UC San Diego

UC San Diego Electronic Theses and Dissertations

Title

Electrical conductivity of solid / liquid suspensions: An analytical model incorporating the effect of suspension stability

Permalink

https://escholarship.org/uc/item/6ct6h16v

Author

Qiao, Shuang

Publication Date

2019

Peer reviewed|Thesis/dissertation

eScholarship.org Powered by the California Digital Library
University of California

UNIVERSITY OF CALIFORNIA SAN DIEGO

Electrical conductivity of solid / liquid suspensions: An analytical model incorporating the effect of suspension stability

A dissertation submitted in partial satisfaction of the

requirements for the degree

Doctor of Philosophy

in

Materials Science and Engineering

by

Shuang Qiao

Committee in charge:

Professor Olivia A. Graeve, Chair
Professor Prabhakar R. Bandaru
Professor Renkun Chen
Professor Javier E. Garay
Professor Patrick P. Mercier

2019

Copyright

Shuang Qiao, 2019

All rights reserved.

The Dissertation of Shuang Qiao is approved, and it is acceptable in quality and form for publication on microfilm and electronically:

_____

_____

_____

_____

_____

Chair

University of California San Diego

2019

TABLE OF CONTENTS

LIST OF FIGURES

LIST OF TABLES

ACKNOWLEDGEMENTS

During my Ph.D. study, I have received numerous help from my adviser, lab mates, family and friends.

First, I would like to thank my supervisor, Prof. Olivia Graeve, for the patient guidance, encouragement and advice she has provided throughout my research and study.

I would like to thank our research scientist Dr. Ekaterina Novitskaya for all her help with my TEM images and my papers.

I would like to give my sincere appreciation to my husband (Ling), my parents (Xiuli Ji and Taibo Qiao) and my sister (Jiayin Ji). The strong support and encouragement from family light me up during the hardest time of my PhD period.

Lastly, I would like to thank all my friends, lab mates, officemates. I have shared a lot of laugh and joy with you guys.

Chapter 1, in part, is currently being prepared for submission for publication of the material. Shuang Qiao, Ekaterina Novitskaya, Flor Sanchez, Manuel Herrera Zaldivar, Rafael Vazquez-Duhalt, and Olivia A. Graeve. The dissertation author was the primary investigator and author of this material.

Chapter 5, in full, is currently being prepared for submission for publication of the material. Shuang Qiao, Ekaterina Novitskaya, Flor Sanchez, Manuel Herrera Zaldivar, Rafael Vazquez-Duhalt, and Olivia A. Graeve. The dissertation author was the primary investigator and author of this material.

Chapter 6, in full, is currently being prepared for submission for publication of the

material. Shuang Qiao, Ekaterina Novitskaya, Flor Sanchez, Manuel Herrera Zaldivar, Rafael Vazquez-Duhalt, and Olivia A. Graeve. The dissertation author was the primary investigator and author of this material.

Chapter 7, in part, is currently being prepared for submission for publication of the material. Shuang Qiao, Ekaterina Novitskaya, Flor Sanchez, Manuel Herrera Zaldivar, Rafael Vazquez-Duhalt, and Olivia A. Graeve. The dissertation author was the primary investigator and author of this material.

VITA

2008-2012	B.S. in Material Shaping and Control engineering, Henan University of Science and Technology, China
2012-2014	M.S. Mechanical Engineering, San Diego State University, USA
2014-2019	Ph.D. in Materials Science and Engineering, University of California San Diego, USA

PUBLICATIONS

H. X. Shi, **S. Qiao**, R. F. Qiu, "Effect of Welding Time on the Joining Phenomena of Diffusion Welded Joint Between Aluminum Alloy and Stainless Steel", *Mater. Manuf. Process*, 2012, **27**, 1366-1369.

S. Qiao, E. Novitskaya, T. Ren, G. Pena, and O. A. Graeve, "Phase and Morphology Control of Magnesium Nanoparticles via Lithium Doping", *Cryst. Growth Des.*, 2019, **19**, 3626-3632.

S. Qiao, E. Novitskaya, F. Sanchez, M. H. Zaldivar, R. Vazquez-Duhalt and O. A. Graeve, "Electrical conductivity of solid / liquid suspensions: An analytical model incorporating the effect of suspension stability", In preparation.

PRESENTATIONS

S. Qiao and O.A. Graeve, "Synthesis of Magnesium Powders of Unique Morphologies," 3rd International Symposium on Nanoscience and Nanomaterials (Ensenada, México. Date: March 10-14, 2014).

S. Qiao, E. Novitskaya, G. Pena, L. Lopez, F. Durazo and O. A. Graeve, "Electrical-conductive mesoporous ceramic with doping for enzyme catalyst", UCSD Jacobs School Annual Research Expo 2015 (La Jolla, CA, April 16, 2015).

S. Qiao, E. Novitskaya, F. Sanchez, R. Vazquez-Duhalt, and O.A. Graeve, "Thermal and Electrical Conductivities of Mesoporous Nanofluids and Applications for Enzyme Catalysis," 2017 TMS Annual Meeting & Exhibition (San Diego, CA. Date: February 26 - March 2, 2017).

S. Qiao, E. Novitskaya, F. Sanchez, M. H. Zaldivar, R. Vazquez-Duhalt, and O. A. Graeve, "Electrical conductivity of stabilized mesoporous ceramic fluid suspensions with varying pH values," UCSD Jacobs School Annual Research Expo 2018 (La Jolla, CA, April 16, 2018).

ABSTRACT OF THE DISSERTATION

Electrical conductivity of solid / liquid suspensions: An analytical model incorporating the effect of suspension stability

by

Shuang Qiao

Doctor of Philosophy in Materials Science and Engineering

University of California San Diego, 2019

Professor Olivia A. Graeve, Chair

The use of electrically conductive mesoporous ceramic powders is a new way for enzyme immobilization aiming for biocatalysts. In this study, mesoporous indium oxide, zinc oxide and titanium dioxide were synthesized by a hydrothermal reaction method. Soft-template and hard-template approaches were utilized to enable mesoporous materials with varying pore sizes. Pore sizes were evaluated by the Brunauer–Emmett–Teller (BET) method and were in the range of 7 to 10 nm. Additionally, indium oxide, zinc oxide and titanium dioxide were doped with tin, gallium, and silver/niobium, respectively, to obtain increased values of electrical conductivity. Afterwards, stable suspensions of mesoporous powders with varying powder volume fractions and pH values were produced through magnetic stirring and ultrasonication and further evaluated by dynamic light scattering (DLS).

Meanwhile, we describe an analytical model predictive of the electrical conductivity of stable ceramic suspensions. Specific model systems in this study include fluids containing

mesoporous powders of TiO_2 doped with silver or niobium, ZnO doped with gallium, and In_2O_3 doped with tin. The electrical conductivities for all four suspensions were found to be lower in acidic solutions (*i.e.*, lower pH) compared to those in basic ones (*i.e.*, higher pH). The behavior of these ceramic suspensions can be explained by considering surface charge and suspension stability. We have also determined that the particle size of the powders has a more pronounced effect on the electrical conductivity of the suspensions compared to powder volume fraction. Particularly, for the same material, larger particle sized suspensions were found to have smaller electrical conductivity due to smaller cumulative surface area of the particles. A theoretical model to describe the electrical conductivity of diluted powder suspensions by incorporating the effects of powder volume fraction, particle size and suspension stability was proposed. This new model predicts the final electrical conductivity of the ceramic suspension by incorporating the effects of powder volume fraction, particle size and suspension stability. The calculations from our model present excellent correlation with the experimental results.

Chapter 1 Introductions

1.1 Mesoporous materials and applications

Porous materials including metal, oxides and carbon are generally composed of three different classes based on their pore sizes: microporous, mesoporous and macroporous materials. Microporous materials are particles with pore sizes less than 2 nm distributed on the surface of particles, mesoporous materials have the pore size in the range of 2 nm-50 nm, macroporous materials have the largest pore sizes (pore sizes >50nm) [1]. The first and also the most well-known mesoporous material is a mesoporous silica called Mobil Composition of Matter No. 41 (MCM-41) [2]. MCM-41 was first discovered and synthesized by researchers from Mobil Research and Development Corporation in 1992. MCM-41 is a synthesized mesoporous silica with hexagonal and uniform pore sizes between 1.5 nm-10 nm. By using a liquid-crystal templating method, MCM-41 with uniform arrays of micro pores and controlled pore sizes can be produced. Later, another mesoporous family discovered by Kuroda and ExxonMobil called M41S broadened the research in mesoporous materials [2]. M41S family are commonly synthesized by using amines and ammonium ions as surfactants during the synthesis process [3, 4, 5, 6]. The surfactants are attracted to the surface of the ceramic precursor and later the synthesized powder precipitates during the heterogeneous hydrothermal reaction process. The surfactants are eventually removed during the synthesis and therefore mesoporous morphology of the particle is obtained. The sizes of the obtained powders are in small micron range. The successful synthesis of M41S family triggers the intensive and mass research and study on mesoporous material synthesis and applications.

Based on the concept and successful synthesis of MCM-41 and M41S, other types of mesoporous silicas have been produced such as MCM-48, MCM-50, SBA-2 etc. [7, 8, 9, 10, 11, 12]. The main difference between these mesoporous silicas is the different shapes of templates utilized during the synthesis process. After removal of the templates, because of the use of different shapes of templates, different pore morphologies will be obtained. For example, MCM-48 is found to have a Ia3d space group based on analysis and calculation from X-Ray diffraction (XRD) and transmission electron microscopy (TEM). Besides, by varying synthesis conditions of MCM-41 like changing the silica/CTAB ratio or using different surfactants, different M41S members have been produced and characterized [8, 9, 10, 11, 12, 13]. One other famous mesoporous silica is called SBA-1. SBA-1 has a three-dimensional cubic structure [13]. Based on SBA-1, mesoporous SBA-15 with highly ordered large pores distribution was synthesized as well [14, 15]. Researchers employed a relatively cheap and later being extensively utilized polymer template named Pluronic (Pluronic 123) as a shape directing agent. Apart from these well known structures, some other novel mesoporous structures have been realized by common wet chemical synthesis through the interaction of surfactants and inorganic precursors. A rectangular arrangement of linear channels was obtained with an orthorhombic structured silica and further observed with TEM [16]. Mesostructured cellular foam material with three-dimensional, continuous large pores was also synthesized with triblock copolymer as template [17]. A chiral mesoporous silica with ordered hexagonal chiral channels was synthesized by Che recently [18]. The complexed morphology was also investigated with transmission electron microscope.

People gradually start to shift their focus from mesoporous silica to other mesoporous materials [9]. It was suggested that by substituting silica with other metal oxides, it is possible to expand mesoporous material family from pure silica to other ceramic materials [19, 20].

Hexagonal structured mesoporous such as tungsten and antimony oxide could be obtained from ionic synthesis approach. While for most other mesoporous metal oxide, Fe^{2+}, Mg^{2+}, Mn^{2+}, Fe3+, Co^{2+}, Ni^{2+}, Zn^{2+}, Al^{3+} and Ga^{3+} present lamellar phases [19, 20]. Semi-crystalline mesoporous metal oxides such as TiO_2, ZrO_2, Al_2O_3, Nb_2O_5, Ta_2O_5, WO_3, HfO_2, SnO_2 as well as mixed oxides $SiAlO_{3.5}$, $SiTiO_4$, $ZrTiO_4$, Al_2TiO_5, ZrW_2O_8 with large pores have later been reported by Yang et al [21]. The synthesized powders present a well ordered nanocrystalline structures which are located within amorphous walls. One of the most famous and intensively investigated mesoporous non-silica is mesoporous carbon. Mesoporous carbon has also been prepared and characterized [22, 23, 24, 25] by several research groups. Among them, the first mesoporous carbon was synthesized by Ryoon and his collaborators in 1999 [23]. As described in the paper, they used mesoporous silica sieves as templates to synthesize ordered mesoporous carbon [23]. The synthesis process includes mild carbonation process of sucrose with sulfuric acid as catalyst. The slow and mild synthesis process guaranteed the successful synthesis of well-ordered carbon sieves after the removal of silica templates. Later, Hyeon and co-workers also made mesoporous carbon (named SNU-x) with very similar method [26]. Similarly, during the process mesoporous silica (MCM-48 or SBA-15) was used as template and impregnated in the carbon precursor. After removing silica by etching process, mesoporous carbon was obtained. Morphology control of mesoporous carbon has been proven very successful, as many different mesoporous carbon have been synthesized including single crystals [27], monoliths [28], fiber [28], nanospheres [29], vesicles [30] and films [31]. Apart from mesoporous metal oxides and mesoporous carbons, the synthesis has been expanded to transition metal oxides and this results in the synthesis of mesoporous composites [32, 33]. With sol-gel process, a multi-layer mesoporous composite of

Fe_3O_4/SiO_2-Au/SiO_2 was fabricated and had shown good potential as catalysis for various catalytic reactions.

Mesoporous materials have wide potential applications as catalysis, energy storage, drug delivery, adsorption and sensing devices [20, 34, 35, 36, 37, 38]. Mesoporous materials have the advantages of large surface area, controllable and uniform pore sizes. They are more favorable used as hosts and adsorption of large protein or organic molecules [39, 40]. Specifically, those enzymes and some other bio organic compounds can be immobilized in the pores on the surface of mesoporous materials and remain their functionality. Amino acids are important supplements and support for proteins in food technology and human daily life. Mesoporous silica (MCM-41 type) was tested for the adsorption of amino acids in aqueous solution. The results show that the effect of loading highly depends on the solution pH and amino acid types [37]. Later, phenylalanine and leucine on C14-MCM-41 was also investigated [37]. It has been confirmed that MCM-41 is a very good candidate for protein adsorption. MCM-41 also has better adsorption of vitamin B-2 compared with MCM-48 [41]. The pore size differences between two mesoporous silicas (MCM-41 and MCM-48) result in different adsorption behavior.

Other examples include the adsorption of vitamin E with mesoporous carbon in n-heptane and n-butanol solutions [42]. Based on the research, larger specific pore volumes can lead to better vitamin E adsorption. So far, it has shown successful attachment of a variety of proteins and small bio molecules such as vitamin E, catalase, lysozyme etc. on ordered mesoporous silica [40, 43, 44, 45, 46, 47]. Some simple molecules rather than protein have also been tested and explored to develop adsorption system [48]. SBA-15 and MCF together with polysaccharide molecules (dextrans) were tested. These combinations provided some insights into the relationship between adsorption amount and molecular weights of protein and bio molecules.

The combination of mesoporous silica or carbon with enzyme immobilization can be further used as bio catalysis, drug delivery and bio molecules separations [49, 50, 51, 52]. Controlled drug delivery system is a process that the drug delivery amount and rate can be well controlled and the targeting area in body is well defined. As a fast developing and one of the most promising applications in human health, it has been intensively studied recently [49, 50, 51]. It was in 2001 that MCM-41 was first suggested as a potential candidate for drug-delivery system [52]. Mesoporous silica has several advantages as being employed in drug delivery system. Firstly, it has very homogeneous pore size distribution, which allows precise control of drug loading and release process. Secondly, it has large pore volumes and it enables large amounts of drug loading. The high surface area of mesoporous silica can guarantee more drug adsorption during the loading process. Lastly, the surface of mesoporous silica can be accordingly functionally changed for better drug release control. These outstanding advantages of mesoporous silica make them great candidates for drug delivery system. Apart from aboved mentioned properties, silica-based mesoporous materials also show good biocompatibility based on previous research [53, 54, 55].

For other mesoporous materials, by depositing proteins in porous glass and sol-gels, they can be used as bio-sensors [56]. Some recent studies have shown that mesoporous glass together with proteins have great potentials for using as biosensors and biological applications [57, 58]. However, the disadvantage of porous glass is the high cost. To solve this issue, researchers changed from porous glass to mesoporous silica after the successful discovery of mesoporous silicate molecular sieves. The mesoporous inorganic materials are usually synthesized by a hydrothermal procedure in an autoclave and the synthesized inorganic materials present narrow pore distributions.

Mesoporous materials can also be utilized as electrodes in solar cells, fuel cells and batteries. The special porous morphology enables them suitable for several different materials adsorption like lithium ions, hydrogen atoms sulfur molecules and so on [59, 60]. Big surface area and large pore sizes make them more efficient in electrolyte transport [61]. Mesoporous TiO_2 is among the best choice due to its superior chemical and physical advantages compared to other metal oxides [62]. Mesoporous crystalline Si can also be used for solar fuel production due to its superior behavior in photocatalytic activity for hydrogen evolution [63]. Except TiO_2 and Si, mesoporous Ta_3N_5, Fe_2O_3, WO_3, $BiVO_4$ and C_3N_4 have also been proven to possess better activity in fuel production compared to other novel materials [64, 65, 66, 67, 68, 69]. Furthermore, mesoporous materials have wide applications in rechargeable batteries, supercapacitors and fuel cells [70, 71, 72]. Higher efficiency is obtained from its mesoporous morphology due to the reason that those interconnected channel walls and micro sized pores can better facilitate electron transport. Overall, the presence of meso-pores can greatly increase their efficiency and stability in energy storage and energy conversion.

1.2 Mesoporous material synthesis methods

There are multiple approaches in mesoporous material synthesis, such as soft-templating, hard-templating and template-free methods [73, 74, 75, 76, 77, 78, 79, 80, 81, 82].

Soft-template method is mainly realized by two pathways: cooperative self-assembly and ‘‘true’’ liquid-crystal templating process [75, 83]. Generally, for soft-template method surfactant molecules such as polymer are assembled inside particles during the wet-chemical synthesis process [84, 85, 86, 87]. Templates or structure directing agents are removed afterwards by heat treatment to leave particles with open pores. During the self-assembly process, surfactants that are serving as template interact with aiming materials. The interaction is driven by Coulomb force, covalent bond or hydrogen bonding. Phase separation and rearrangement between inorganic material and surfactants take place and eventually materials with uniform pores distribution are obtained. For the second approach (liquid-crystal templating method), surfactants can form crystal or half-crystal liquid templates during the synthesis process. Inorganic materials will grow surrounding the template, templates are removed after reaction. Usually, the surfactant is made up of hydrophobic and hydrophilic parts. Depends on the concentration of amphiphile, there are three different arrangements for the surfactants [88]. At low concentration, they will aggregate at the surface. With concentration increase, surfactant will arrange into micelles. Eventually, it will reach the critical micelle concentration [89]. Beyond the critical micelle concentration, these self-assembly clusters will form 2D rod, 3D sphere and some other arrays and further these molecules become the void spaces to produce final pores on particles. Based on soft-template methods, a lot of materials have been successfully synthesized including silica [2, 14, 74, 78, 79, 80, 90], aluminosilicates [90, 91, 92, 93, 94, 95], organosilica [61, 69, 96, 97, 98], carbon [99, 100], metal oxides [101, 102, 103, 104, 105, 106, 107], metal [108, 109, 110], and polymers [111, 112].

There are both advantages and disadvantages using soft-template methods in producing mesoporous materials. The pore size and structures are controllable using soft-template methods, high quality and large production are also achievable. But it requires addition of template and for most of the cases those surfactants are very sensitive to the environments like pH and temperature change [71]. Therefore, soft-template methods have some limitations.

Hard-template method also known as nanocasting is another common way for producing mesoporous materials [73, 75]. Usually mesoporous carbon or mesoporous silica even some clusters of nanoparticles serve as the hard templates. During the synthesis process, these templates need to be well assembled with surfactants. Meanwhile, the mischannels need to be fully filled with targeting synthesized materials to guarantee the final organized mesoporous morphology after hard templates removal. Because of the good protection from these hard templates, highly ordered crystalline even single-crystalline materials can be synthesized. Among the hard-templates, KIT-6 is the most famous and commonly used template [113]. KIT-6 is a well-organized mesoporous silica with uniform pore distribution and it belongs to the cubic Ia3d space group. The pore diameter of KIT-6 can be adjusted by changing the synthesis condition, which makes it a very flexible template choice. A wide range of mesoporous materials have been synthesized with hard-template methods including but not limited to carbon [74, 75, 76, 78, 79, 80, 90, 114], metal oxide [66, 67, 115, 116], metal sulfides [117, 118, 119, 120], metal nitrides [121, 122, 123, 124, 125] and metal carbides [126, 127]. Albeit its great advantages in producing highly organized and well-ordered mesoporous materials, the use of hard-template is very expensive, and the synthesis process is time and labor consuming. Besides, the limited choices of hard-templates make it less flexible compared with soft-template methods.

Apart from synthesis methods with templates, template-free solvothermal synthesis is another very common way to produce mesoporous material by the nucleation and aggregation of nanoparticles [128, 129]. Compared with hard-template and soft-template methods, template-free route is more convenient and cost efficient. Mesoporous titanium dioxide [130, 131, 132], iron oxide [133], copper oxide [134] and some other metal oxide [135, 136], silica [137, 138] have been produced with template-free approach.

Besides the above mentioned most-common methods, multi-templating method [139], In-situ templating pathway [140, 141, 142, 143, 144] are also achievable ways in producing mesoporous materials.

1.3 Introduction of the four materials

1.3.1 TiO_2 and Ag/Nb doped TiO_2

Titanium dioxide or titania is a white chemical powder with characters of good thermal stability, nontoxicity and nonflammability [145]. It also has poor solubility in water and is highly resistant to corrosion. Titanium dioxide has three different crystal structures including rutile, anatase and brookite. Rutile and anatase phases are the most common phases with both wide band gaps of 3.2 eV (387 nm) and 3.0 eV (413 nm) [146]. The common and widely used methods to produce titanium dioxide are sulfate process and chloride process [145]. Titanium dioxide has wide industrial applications such as photocatalysts and ingredient for sunscreen due to its high UV absorbing efficiency. In 1972, Fujishima and Honda did pioneer work of using titanium dioxide as photoelectrodes [147]. The application of titanium dioxide as a photoelectrode which can split water into hydrogen and oxygen with reaction of sunlight has received wide attention. Besides, titanium dioxide has been widely investigated with different doping elements including Fe, Co, Cr, Ni, Mo [148, 149, 150, 151, 152, 153, 154, 155, 156, 157, 158, 159], N, C, F, and S [160, 161, 162, 163, 164, 165, 166, 167, 168, 169, 170, 171]. In current research, we are mainly interested in the incorporation of silver and niobium as doping materials. Silver can be added to titanium dioxide during the synthesis process by two ways. One method is to reduce silver ion to silver metal by irradiating the mixture, the other method is to decompose silver nitrite to silver ions during the sol-gel synthesis with calcination process [172]. The main application of silver doped titanium dioxide is to produce semi-conducting photocatalytic material. They can efficiently tackle environment contaminants by degrading organic pollutants [172]. The wide band gap of titanium dioxide limits it using visible light as light resources. Since majority of sunlight composes visible light, this restricts titanium dioxide from being used as solar or room-light activated

catalysts. Numerous studies have been conducted to try to develop the visible light activity with titanium dioxide by using silver doping. The introduce of doping metal ions into titanium dioxide can change its charge carrier concentration and electron transfer rate. The electrical conductivity of titanium dioxide can be great improved from doping elements such as silver and niobium [173, 174].

1.3.2 ZnO and Ga doped ZnO

Zinc is a very active metal. Because of its small reduction potential, it can easily oxidize and usually present zinc oxide in nature. Despite of the fact that zinc is very crucial for human organisms [175, 176] and is usually regarded as non-toxic, there is evidence showing that free zinc ions may cause neutron degradation [177]. In this case, zinc oxide is preferred as a choice in many chemistry and daily life compared with pure zinc. Zin oxide possesses outstanding characteristics and performance in optical and electrical applications [178]. Zinc oxide has electron-binding energy of 60 meV [179] and a wide band gap of 3.37 eV. It is a typical n-type semiconductor [180]. Zinc oxide can be utilized in optoelectronic industry and applied to visible and close to ultraviolet spectral materials. In specific applications, it can be used as photo-catalysts [181, 182], gas sensors [183, 184], pharmaceutical and cosmetic materials [185], UV-light emitting devices [186, 187]. Zinc oxide normally has two crystal structures: hexagonal wurtzite and cubic blende. It can be synthesized either in physical [188, 189, 190, 191, 192] or chemical way [193, 194, 195, 196]. Zinc oxide has very poor electrical conductivity, but Ga doped zinc oxide possesses high electrical conductivity since the substantial doping can increase the charge carrier density [197]. There has been report stating that Ga doped zinc oxide can have electrical conductivity as high as 8.12×10^{-5} Ω cm [198, 199, 200]. The increased electrical conductivity, better environment stability and lower cost of Ga doped zinc oxide make it a better substitute for traditional

semiconductor or electrical conductive ceramic materials in a variety of application such as solar cells [201, 202] and organic photovoltaics [203, 204, 205, 206].

1.3.3 In_2O_3 and Sn doped In_2O_3

Indium oxide is a n-type semiconductor with a band gap of 3.5eV [207]. When synthesized at low temperature (below 250 °C) indium oxide is amorphous and when synthesized at above 250 °C indium oxide is crystalline cubic phase [208]. Indium oxide shows high optical transmittance, high optical reflectance and low electrical conductivity. By adding external doping materials, the optical transmittance and electrical conductivity of indium oxide can be further increased or decreased [209, 210]. Normally, indium oxide behaves as insulator, but by creating defects or making off stoichiometry in the material it can become electrically conductive [211]. Because of its superior and special qualities, indium oxide has wide applications in using as transparent conducting electrodes, ethanol vapor or other chemical gas sensors, coating materials, photovoltaic devices, etc. [212, 213, 214, 215, 216, 217, 218]. The most common doping materials in indium oxide include iron, nickel, carbon, fluorine, cobalt, chromium, manganese, copper, molybdenum [208]. Among all these doping materials, indium tin oxide (ITO) is the most famous and widely used material with potential applications in biosensors and photovoltaic devices [219]. Compared with pure indium oxide, indium tin oxide shows superior electrical conductivity and optical transmittance [219].

1.4 Nanofluids & stable micron particles suspensions

It has been demonstrated that adding particles (metal, metal oxide) into base fluids (water, ethanol or oil) can greatly improve the thermal conductivity of the corresponding suspensions compared with pure base fluids [220, 221, 222, 223, 224]. Among them, nanofluids are the most investigated. Nanofluids are stable base fluids (water, ethanol, ethylene glycol etc.) containing nanosized materials (nano particles, nanofibers, nanotubes etc.). Nanofluids was first proposed and developed to increase the heat transfer fluids thermal conductivity [225]. It shows superior characteristics compared to conventional solid-liquid unstable suspensions which are combinations of separate phases [222]. The nano-sized materials in nanofluids have larger surface areas thus it improves the heat transfer process. Besides, nanofluids have reduced particle agglomeration and higher suspension stability compared to conventional slurries. By changing different materials and base fluids, nanofluids is a very flexible system with adjustable properties. Nanofluids can be used for heat dissipation in electronic system because of its higher thermal conductivity [226, 227]. It can also be used for industrial transportation system, micromechanics and instrumentation and heating, ventilating and air-conditioning (HVAC) systems [228]. There are commonly two-step and one-step methods to form nanofluids. For two-step method, nano-sized particles were first synthesized through chemical or physical method [229]. After obtaining the nanomaterials, physical mixture like magnetic stirring, ultrasonication and ball milling are applied between nanomaterials and base fluids. Eventually a well dispersed stable suspension can be produced. Two-step method is the most common and economic way to synthesize nanofluids and has been used in large-scale industrial production. For one-step method, the particle synthesis and dispersion are conducted at the same time [223]. Particle agglomeration can be greatly

decreased, and particle stability is greatly increased with this preparation method [230]. However, one-step method cannot produce suspensions in large scale and the cost is high.

There have also been many investigations on other stable suspensions with larger particle sizes [231, 232, 233]. Usually the powders are a few hundred nanometers or even micrometers. These suspensions also have wide applications due to the facts that they are more convenient to be produced and much cheaper compared to nanofluids. They also have very superior advantages in applications for electronics, solar cells, thermal and electrical uses.

1.5 Zeta potentials and electrical double layer

For powder suspensions, zeta potentials and electrical double layers (EDL) are the two most important parameters deciding the suspension stability and particle size distributions. When particle is in contact with base fluids, an electrical double layer is formed on the surface of the particle. On the surface of the particle, there is an electrical field and this electrical field attracts opposite charges from the solutions and repels the same charges. Outside the layer of the particle, there is a layer of attractive counterions and repulsive co-ions. Together they make up of the electrical double layer. Electrical double layer is composed of two layers: diffuse layer and Stern layer [234]. The schematic illustration [234] of electrical double layer is shown in **Figure** 1.1

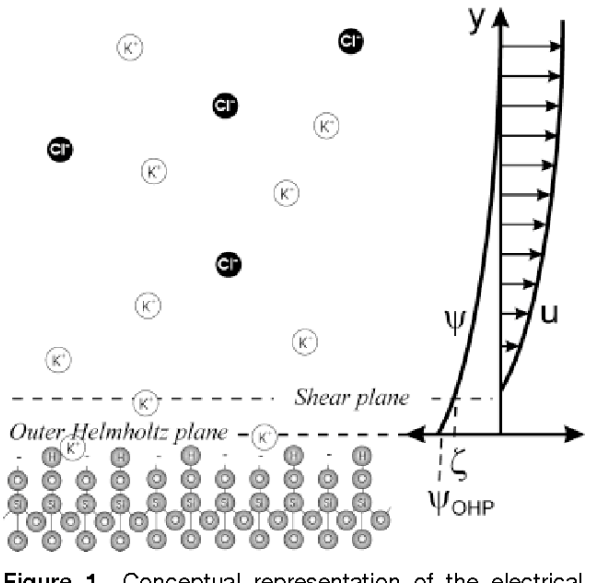

Figure 1.1 Conceptual representation of the electrical double layer [234]

When powders are dispersed in aqueous solutions, the electrostatic interactions between the two phases are very important study and key interest in many areas such as soft material [235], colloidal science [236] energy storage devices [237, 238] and surface chemistry [239, 240]. The

electrical double layer is normally only a few nanometers thick. This thin layer plays important roles in affecting the behavior of charged ions, interactions between particles and the particle-liquid interfaces. The electrostatic interactions between each charged particle, the motion of the particles in electric field, interfaces and solutions motions are all controlled by electrical double layer [241, 242, 243, 244, 245, 246, 247, 248]. Currently there are several models trying to explain electrical double layer. One of the famous models is Gouy-Chapman-Stern Model [249, 250, 251]. Internal stern layer and outside Gouy-Chapman diffuse layer are the two components of electrical double layer.

At the interphase between moving particle and solutions, there are simultaneous interactions between mechanical and electrical effects. Zeta potential is the electrical potential measured at the slipping plane. With distance increase at the diffuse layer of electrical double layer, zeta potential is found to decrease [252]. It can be expressed as **Equation 1.1:**

$$\Psi_{(x)}=\Psi_{\delta} \exp(-\kappa\chi) \quad (1.1)$$

X represents the distance away from the stern layer to the inside slipping plane.

Zeta potential can be determined by four different kinds of electrokinetic phenomena: Electro-osmosis, electrophoresis, streaming potential and sedimentation potential [253]. Depending on the particle sizes and electrical double layer thickness, zeta potential of suspensions can vary greatly [253]. In colloidal systems, zeta potential is usually obtained by measuring responses of small particles when they are placed in an applied electrical field.

1.6 Particle size distributions and Dynamic Light Scattering

Suspensions with particles uniformly distributed in solutions are widely used in pharmacy, food industry, medicine etc. [254, 255, 256, 257, 258, 259]. The most important parameters to characterize suspensions are the particle size distribution and suspension stability. Dynamic light scattering (DLS) is the most common method to determine the particle size [260, 261, 262, 263, 264]. DLS is also known as photon correlation spectroscopy [265] and quasi-elastic light scattering [266]. Based on the sizes of the particles, there are Rayleigh scattering (for small particle sizes) and anisotropic Mie scattering (for larger particle sizes) [267, 268, 269]. The schematic figure showing the two different kinds of scatterings are shown below in **Figure 1.2** [270].

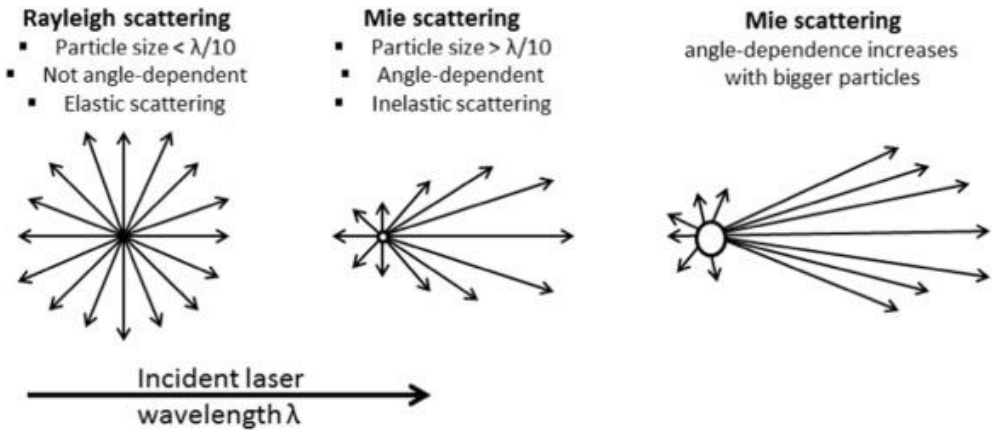

Figure 1.2 Two different kinds of scatterings based on the particle sizes [270]

In a colloidal suspension system, the particle will interact with the incoming laser and scatter back a signal, the intensity of the scattered light can be detected by DLS.

1.7 Current electrical conductivity study of mesoporous materials

Mesoporous materials have large surface area and uniform organized pore distributions. They can be used for thermoelectrical materials since the pores can reduce their thermal conductivities. Further, by doping impurities can increase their electrical conductivity [174]. Mesoporous TiO_2 thin films have been synthesized with 3 at% Ag doping through a sol-gel process [174]. Because Ag^+ ion is much larger than Ti^{4+} ion, during the doping process, Ag^+ ions aggregate and form metallic Ag phase than substitute Ti^{4+} ions. The formation of this metallic Ag phase greatly improves the electrical conductivity of synthesized mesoporous TiO_2 thin films. Sn doping concentration has been altered the electrical conductivity of mesoporous indium tin oxide has been investigated [271, 272, 273]. A certain amount of Sn can improve the electrical conductivity of mesoporous indium oxide. Sn can substitute In during the doping process and result in excessive unpaired electrons from the mismatch of stoichiometric ratio. These free electrons can behave as free carriers since they are bounded together by weak forces. The introduce of these free carriers greatly improve the electrical conductivity of the original mesoporous indium oxide material. Indium tin oxide with highest electrical conductivity can be obtained when 10 mol% tin doping is added. Mesoporous tungsten oxide with high electrical conductivity has also been synthesized and analyzed [274]. Because of its high electrical conductivity, it can be used as pseudocapacitor electrode. By using hard-template method and KIT-6 silica as the template, well ordered mesoporous tungsten oxide is obtained and its electrical conductivity is almost as high as mesoporous carbon.

1.8 Electrical conductivity models

Apart from experimental observations of the electrical conductivity of stable suspensions, several models have been developed to better understand the mechanisms and predict the electrical conductivity of these system [275, 276, 277, 278, 279, 280, 281, 282, 283].

The earliest model to describe both the electrical and thermal conductivities of suspensions is the Maxwell model [275] with the equation expressed by:

$$\frac{\sigma_p}{\sigma_0} = \frac{2\sigma_0+\sigma_P-2(\sigma_0-\sigma_P)\varphi}{2\sigma_0+\sigma_P+(\sigma_0-\sigma_P)\varphi} \quad (1.2)$$

where σ_0 is the electrical conductivity of the base fluid, σ_p is the electrical conductivity of the solid nanoparticles, and φ is the powder volume fraction. This model can be applied to predict the electrical conductivity of solid-liquid suspensions with low powder volume fractions and uniform dispersion. The model can also be expressed by **Equation 2**, where α is the ratio between the electrical conductivity of particles and the electrical conductivity of base fluid:

$$\sigma_{Maxwell} = \sigma_0\left(1 + \frac{3(\alpha-1)\varphi}{(\alpha+2)-(\alpha-1)\varphi}\right) \quad (1.3)$$

This equation is the most common form of the Maxwell equation. By further considering the conducting nature of both solid particles and liquid base fluid, the Maxwell model is able to describe the following three cases: (Case 1) insulating particles ($\sigma_p << \sigma_o$), (Case 2) almost equal conductivity between particles and a base fluid ($\sigma_p = \sigma_o$), and (Case 3) highly conductive particles ($\sigma_p >> \sigma_o$). The conductivity ratio can be simplified by functions of particle volume fractions for each case:

Case 1: $\alpha \to 0,\ \frac{\sigma}{\sigma_0} = 1 - \frac{3}{2}\varphi$ (insulating particles)

Case 2: $\alpha = 1, \frac{\sigma}{\sigma_0} = 1$ (almost equal conductivity between particles and a base fluid)

Case 3: $\alpha \to \infty, \frac{\sigma}{\sigma_0} = 1 + 3\varphi$ (highly conductive particles)

Therefore, the corresponding electrical conductivity of a suspension can be smaller, equal or larger than the electrical conductivity of a base fluid. The ratio between electrical conductivity of particles and base fluid determines the contribution of the dispersed phase to the entire electrical conductivity of the suspension. When this model is applied to suspensions with low powder volume fractions (dilute suspensions with powder volume fraction ≤ 1vol.%), it demonstrates almost a linear dependence between the electrical conductivity of a suspension and the corresponding particle volume fractions. The Maxwell model demonstrates a good agreement for several dilute suspensions [284, 285]. However, several studies have shown that the electrical conductivity of insulating particles is underestimated by the Maxwell model [279, 286]. The main limitation of this model is that it neglects factors that have been shown to influence the behavior, including particle size, particle dynamics, particle-particle interactions, and particle-solution interactions.

Based on Maxwell model, a more comprehensive model including the particle interactions with dispersing solution was developed by Shen [276, 280]. This model was verified with zinc oxide in insulated oil fluids system. The author measured the electrical conductivities of zinc oxide-insulated oil system. It was proposed that the final nanofluids' electrical conductivity should be a combination of static electrical conductivity (Maxwell model) and dynamic (Brownian motion and Electrophoresis) electrical conductivities. The specific equation describing the model is shown by **Equation 1.4**:

$$\sigma = \sigma_M + \sigma_B + \sigma_E$$

$$=\delta_{0(T)}(1+3\varphi)+\frac{3\varphi\varepsilon_r\varepsilon_0 U_0}{r^{\frac{2}{3}}}\left(\frac{RT}{L}.\frac{e^{\lambda(T-T_0)}}{3\pi\rho\upsilon(1+25\varphi+625\varphi^2)}\right)^{\frac{1}{2}}+\frac{2\varphi{\varepsilon_r}^2{\varepsilon_0}^2{U_0}^2}{\rho\upsilon(1+25\varphi+625\varphi^2r^2)}e^{\lambda(T-T_0)} \quad (1.4)$$

In this equation, σ_M, σ_B, σ_E represent the electrical conductivity from Maxwell model, Brownian motion and Electrophoresis respectively. φ is powder volume fraction, ε_0 and ε_r are the

dielectric constant of the vacuum and relatively dielectric constant of the base fluid. r is the average radius of the particle and U_0 is the zeta potential of the nanofluids. ρ is the density of the fluid and υ is the kinetic viscosity of the fluid. T is the temperature in Kelvin, L and R represent Avogadro's constant and thermodynamic constant. λ is the viscosity index of the fluid.

A relatively complicated model was generated to describe the relationship between nanofluids' electrical conductivity and powder volume fraction/temperature change. The main restriction for this model is using insulated oil as a solvent. Since there is very limited ion exchange between zinc oxide and insulate oil system, the ion exchange and transportation are very rare compared to conventional water-based ceramic suspensions. Besides, pH changes or suspension stability was not considered in this model, therefore, this model cannot fully explain the mechanisms of electrical conductivity of ceramic suspensions.

Ganguly *et al*. [278] and Minea and Luciu [281, 287] both proposed a two-factor equation using a regression analysis to model the suspension's electrical conductivity based on the experimental measurements of their alumina-water system. They obtained equations (**Equation 1.5** and **Equation 1.6**) to describe the empirical relationship for the final alumina-water nanofluid electrical conductivity as a function of particle volume fraction ϕ and temperature *T*.

$$\frac{\lambda_{eff}-\lambda_{bf}}{\lambda_{bf}} = 3679.049\phi + 1.085799T - 43.6384 \quad (1.5)$$

λ_{eff} represents the electrical conductivity of nanofluids and λ_{bf} is the electrical conductivity of base fluids.

$$K_{Electrical\ conductivity} = 176.69 + 588.41\phi - 13.64T - 86.31\phi^2 + 0.36T^2 + 1.07t\phi + 11.06\phi^3 - 0.003T^3 + 0.18t^2\phi - -1.01t\phi^2 \quad (1.6)$$

Both of those equations are only based on the fitting of alumina-water electrical conductivity data that were obtained in the experiments with regression analysis. Thus, they are not applicable to other material systems.

O'brien [283] developed more complicated model with wider applications using the electro kinetic radius and zeta potential to predict the electrical conductivity of dilute suspensions. It was assumed that when particles are dispersed into solution, particles together with their double layer (a thin layer that appears on the surface of the particle when it is dispersed in fluid) only occupy small part of the total suspension volume. As a result, ions will aggregate on the surface of the particle and contribute to the electrical conductivity of the suspension. To calculate the electrical conductivity of the suspension, a series of coupled differential equations were used to calculate the flow field as well as ion densities, quantities of the electric field on the surface and away from the particles. This model provides an approximate solution for the situation of low zeta potential suspensions with a symmetric electrolyte (a substance whose formula unit has one cation and one anion that dissociate completely) dispersed with spherical particle. The electrical conductivity K^* is finalized with **Equation 1.7** shown as below:

$$\frac{K^*}{K_{bf}} = 1 - 3\phi - [\frac{L(\kappa\alpha)I_3 e\zeta}{kT} - \left\{ I_4 M(\kappa\alpha) + N(\kappa\alpha)\left(\frac{\sum_{j=1}^{j=N} z_j^2 n_j^\infty}{\sum_{j=1}^{j=N} z_j^2 \left(\frac{n_j^\infty}{m_j}\right)} \right) \right\} \left(\frac{e\zeta}{kT}\right)^2] \quad (1.7)$$

To better understand and simply Equation 4, three parameters are expressed below:

$I_3=\frac{z_1(\omega_1-\omega_2)}{(\omega_1+\omega_2)}$

$I_4={z_1}^2$

$\frac{\sum_{j=1}^{j=N} z_j^2 n_j^\infty}{\sum_{j=1}^{j=N} z_j^2 \left(\frac{n_j^\infty}{m_j}\right)}=\frac{2m_1m_2}{m_1+m_2}$

In the above Equations each of the variables are defined as below: K^* is the electrical conductivity of suspension, K_{bf} is conductivity of the electrolyte beyond the double layers and K is the electrical conductivity of the fluid. z_1 is ionic charge, T represents the temperature. ω_1 and ω_2 are the ionic mobility of the suspensions, m_1 and m_2 are ionic drag coefficients of the particles. ζ is the zeta potential of the suspension. $(\kappa\alpha)$ is the double layer thickness. $L(\kappa\alpha)$, $M(\kappa\alpha)$ and $N(\kappa\alpha)$ are the mathematical functions of exponential integrals.

The main limitation of this model is that it is only applied to low zeta potential (near 0) suspensions with nonconducting charged particles. At this low zeta potential status, the suspension is highly unstable. It is not applicable to stable suspensions. Therefore, this equation is more useful to determine the zeta-potential of particles which is too small to be observed using common tools (such as DLS) than to predict the electrical conductivity of the suspension.

Despite the fact that an extensive and tremendous research of the effects of temperature, powder volume fraction, particle sizes on the corresponding electrical conductivity of ceramic suspensions was performed [277, 278, 288], most of the studies are limited to be focusing on one or two aspects only. In addition, to the best of the author's knowledge, there is no research studies targeting mesoporous ceramic suspensions. One of the goals for the current study is to propose a new model which will combine the previous efforts to describe an electrical conductivity of ceramic suspensions. In this paper, ceramic suspensions based on four mesoporous materials (Ag/Nb doped TiO_2, Ga doped ZnO, and Sn doped In_2O_3) were produced, and their electrical conductivities were extensively studied. Most importantly, a comprehensive model to describe the electrical conductivity behavior of dilute mesoporous ceramic suspensions was proposed. An excellent correlation between the model predictions and experimental results was obtained.

1.9 Goals of my research

Four mesoporous materials with different doping elements are synthesized and analyzed with a variety of technical methods. Mesoporous ZnO:Ga, TiO_2:Ag, TiO_2:Nb, In_2O_3:Sn are the four targeting materials in our research. They are synthesized by both soft and hard template methods. The electrical conductivities of the synthesized mesoporous materials are increased after different dopings. Pore sizes and morphologies are studied by BET and TEM methods. Afterwards, mesoporous suspensions with varying powder volume fractions and solution pH values are produced through overnight magnetic stirring and long-time ultrasonication. Their electrical conductivities are measured with a bench meter electrical conductivity machine. Meanwhile, particle sizes and zeta potential values of the suspensions are also measured with dynamic light scattering (DLS). Correlations between particle sizes, suspension stability and their electrical conductivities are summarized. A systematic investigation of a wide range of electrically conductive mesoporous material suspensions are studied as well as their mechanism are discussed.

Fungal peroxidases are enzymes able to perform catalysis in superficial amino acids through a long-range electron transfer (LRET). The use of electrically conductive mesoporous ceramic powders appears as a new way for enzyme immobilization aiming to oxidize potential substrates directly in the mesoporous ceramic and improving the overall biocatalytic performance. The goal of this project is the design and characterization of unique mesoporous biocatalytic electrode architectures for optimal energy conversion in biofuel cells (BFCs). We will explore the fundamental behavior, design, optimization, and manufacturing of mesoporous powders and their incorporation into biomimic fluids. The fundamental contribution of this project to science and engineering is the discernment of the necessary foundational principles required for the

development of unique electrode architectures and favorably oriented modified enzymes in mesoporous materials for efficient bioenergy harvesting.

Chapter 1, in part, is currently being prepared for submission for publication of the material. Shuang Qiao, Ekaterina Novitskaya, Flor Sanchez, Manuel Herrera Zaldivar, Rafael Vazquez-Duhalt, and Olivia A. Graeve. The dissertation author was the primary investigator and author of this material.

Chapter 2 Mesoporous Powders Synthesis and Characterizations

2.1 Powder synthesis

2.1.1 Synthesis of Ga doped mesoporous ZnO

Mesoporous ZnO was synthesized with template-free method. Ga dopant was added during the synthesis process with gallium nitrate as doping agent. To be specific [289], 2.97 g of zinc nitrate hexahydrate (223787, reagent grade, 98%, Sigma Aldrich, St. Louis, MO, USA) was mixed and dissolved in polyethylene glycol 200 (PEG 200) (81839, Fisher Scientific, Hampton, NH, USA). Then 0.13 g of gallium nitrate (289892, 99.9% trace metals basis, Sigma Aldrich, St. Louis, MO, USA) was added into the above solution. The solution was kept for 6 hours at a temperature of 160°C. After cooling to room temperature, the synthesized brown powder was washed with deionized water and ethanol twice. Eventually, the powder was heated at 500°C for 4 hours to acquire its final mesoporous morphology.

2.1.2 Synthesis of Ag/Nb doped TiO_2

The procedure of producing mesoporous TiO_2 was similar to [290] with several extra doping steps. A mass of 1.50 g of poloxamer 407 (16758, purified, non-ionic, Sigma Aldrich, St. Louis, MO, USA) was dissolved in 100 mL of deionized water and 0.82 mL of sulfuric acid (11000, 99.999%, Alfa Aesar, Haverhill, MA, USA) were dropped into the solution to form Solution 1, after which 0.11 g of $AgNO_3$ (209139, ACS reagent, ⩾99.0%, Sigma Aldrich, St. Louis, MO, USA) were added. Next, 8.15 mL of titanium tetraisopropoxide (TTIP) (377996, 99.999%, Sigma Aldrich, St. Louis, MO, USA) and 2.83 mL of 2,4-pentanedione (A14117, 99%, Alfa Aesar, Haverhill, MA, USA) were simultaneously added into the above solution while stirring at 50°C

for half an hour. The resulting yellow solution was then hydrothermally reacted at 90°C for 10 hours in a heating flask which was connected to a condenser with cooling water system. The obtained powder was filtered and dried at room temperature in air and calcined at a temperature of 600°C, using a heating rate of 1°C/min and a holding time of 2 hours. The procedure for producing Nb-doped TiO_2 was as described above, except the $AgNO_3$ was replaced with $NbCl_4$. During the doping process, 0.38 g of $NbCl_4$ (326364, Sigma Aldrich, St. Louis, MO, USA) were first dissolved in 10 mL of pure ethanol, then the solution was added to Solution 1.

2.1.3 Synthesis of Sn doped In_2O_3

The procedure of producing mesoporous In_2O_3 was similar to the description in [291]. in which the pores were obtained by etching off the silica template (KIT-6) embedded in the In2O3 particles. KIT-6 was originally synthesized using a hydrothermal method. First, 60.00 g of deionized water and 5.83 mL of HCl (H1758, 36.5-38%, Sigma Aldrich, St. Louis, MO, USA) were mixed, after which 1.96 mL of pluronic P123 (435465, PEG-PPG-PEG, Sigma Aldrich, St. Louis, MO, USA) were added and dissolved in the above solution. Subsequently, 2.47 mL of 1-butanol (B7906, for molecular biology, ⩾99%, Sigma Aldrich, St. Louis, MO, USA) were added to the solution, then stirred for 1 hour, after which 4.29 mL of tetraethyl orthosilicate (TEOS) (333859, 99.999%, Sigma Aldrich, St. Louis, MO, USA) were added drop by drop to the solution, and the whole mixture was kept at 35°C for 24 hours. The resulting solution and white precipitate were kept at 140°C for 24 hours. After the hydrothermal reaction in the same set-up that was used to synthesize titanium dioxide, the white as-synthesized product was filtered out, and kept in a mixture of ethanol/HCl (1:1 ratio) solution for 12 hours. After filtering and drying at room temperature in air, the powder was calcined at a temperature of 550°C using a heating rate of 2°C/min and a holding time of 2 hours. The obtained white powder was the KIT-6 silica template.

The first step in the preparation of the Sn-doped In_2O_3 required first dispersing 0.15 g of KIT-6 silica in 8 mL of ethanol. Next, 0.60 g of $In(NO_3)_3$•xH2O (326127, 99.99%, Sigma Aldrich, St. Louis, MO, USA) and 42.00 mg of $SnCl_2$ (208256, reagent grade 98%, Sigma Aldrich, St. Louis, MO, USA) were added into the mixture, left stirring for 2 hours, and then left to dry at 40°C for 24 hours. After drying, the powder went through a two-step heating process. The first step was a 2-hour holding at 130°C, followed by a second heating process of 5-hour holding at 250°C. For both steps, the heating rate was 5°C/min. Then 0.3 g of $In(NO_3)_3$•xH2O and 21.00 mg of $SnCl_2$ were added to the powder obtained from previous step, and stirred for 2 hours in 8 mL of ethanol. After another overnight drying at 40°C, the obtained powder was calcinated with 2-hour holding at 130°C first and then 5-hour holding at 550°C (5°C/min). The last step is to etch off the KIT-6 silica. The etching process was conducted at room temperature. First, 2.40 g of NaOH (S8045, ⩾98%, Sigma Aldrich, St. Louis, MO, USA) were first dissolved in 30 mL of deionized water. The previous obtained powder was added to the NaOH solution and kept at 70°C for 6 hours. The same etching procedure was repeated twice. In_2O_3 powder was retrieved by centrifugation (10 min. at 11000 rpm), washed with deionized water twice and dried at the open air.

2.2 Characterization techniques

All the powders were characterized with multiple techniques: XRD for crystal phases, TEM for particle morphology, EDX for doping confirmation, BET for pore sizes and DLS for particle sizes.

A D2 Phaser (Bruker AXS Inc., Madison, WI) instrument using CuK radiation was used to carry out the powder X-Ray diffraction measurement. During the measurement, step size was 0.04° 2Θ and a count time count time of 1 s by scanning from 20° to 80° 2θ. Particle and pore morphologies were analyzed by transmission electron microscopy (TEM) using a TecnaiTM TEM (G2 Sphera, FEI Company, Hillsboro, OR) instrument with an operating voltage of 200 kV. Powders were well dispersed in acetone with mechanical stirring and ultrasonication as dispersing method. One drop of the diluted solution was put on a copper grid sample holder and dried immediately with a filter paper. EDX was performed with a FEI/Phillips XL30 ESEM. Specific doping element was confirmed by the EDX analysis. Total surface area was measured by Brunauer–Emmett–Teller (BET) method and pore size distribution was calculated with Barrett–Joyner–Halanda (BJH) method [292]. In order to prepare stable nanofluids, the mesoporous powders were dispersed in solutions with different pH values (pH 3-9) for overnight magnetic stirring and subsequent 2h ultrasonication. Solutions with different powder volume fractions (0.125 vol.%, 0.25 vol.% and 1 vol.%) were prepared, and their electrical conductivities were measured with a 4-Cell conductivity electrode meter (Cyber Scan PC10). The set-up was calibrated with de-ionized water and ethanol before measurements. Each measurement was repeated four times to obtain consistent results. The readings from the display show both temperature and electrical conductivity of the suspension once it is stable. Zeta potential and particle size distributions were measured with dynamic light scattering on a Nanotrac Wave II

system (Microtrac Inc., York, PA, USA). The errors are combination of both instrumental and measurement errors. The measurement error is calculated based on the repeating readings for each measurement. The instrumental uncertainty for this machine is ±1% (full number + 1 digit) and 0.1 K (0–1999 _S/cm).

2.3 Powder characterizations

2.3.1 Powder characterizations of Ga doped mesoporous ZnO

Newly synthesized and Ga:ZnO powder after washing procedure is brown color. After calcination at 500 ºC for 4h, the powder turns to milky white. Afterwards, the powder is examined and characterized with X-Ray diffraction (XRD), Scanning electron microscopy (SEM), transmission electron microscopy (TEM) and Brunauer–Emmett–Teller (BET) to confirm its crystal structure, micro morphology and pore sizes.

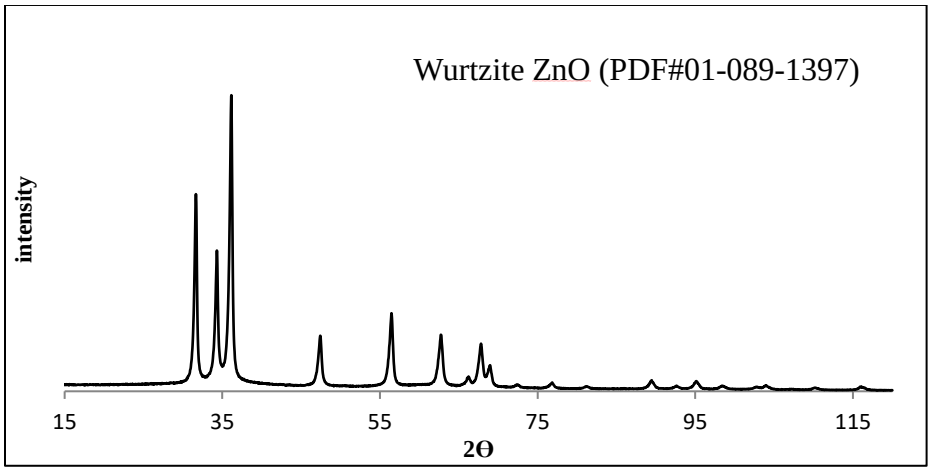

Figure 2.1 XRD pattern for mesoporous ZnO:Ga

Figure 2.1 shows the XRD pattern of the synthesized and calcinated Ga doped ZnO powders. After analysis, all peaks confirm to be consistent with Wurtzite ZnO (PDF card# 01-089-1397). There is no peak for Ga or Ga-Zn, Ga-O, Ga-Zn-O compounds. This means that this small amount of Ga dopant (5 wt.%) does not change the crystal structure of ZnO. The pattern also shows that there is no impurity produced except pure ZnO during the synthesis.

SEM images of Ga doped ZnO are shown in **Figure 2.2**. It shows that the particles have two different sizes. The larger particles (sphere balls) are about 1-2 micron and the smaller particles are about a few hundred nanometers. Both small and large sized particles show mesoporous morphology. Most particles show a round cage-like morphology with various of pores distributed on the surface of the ball.

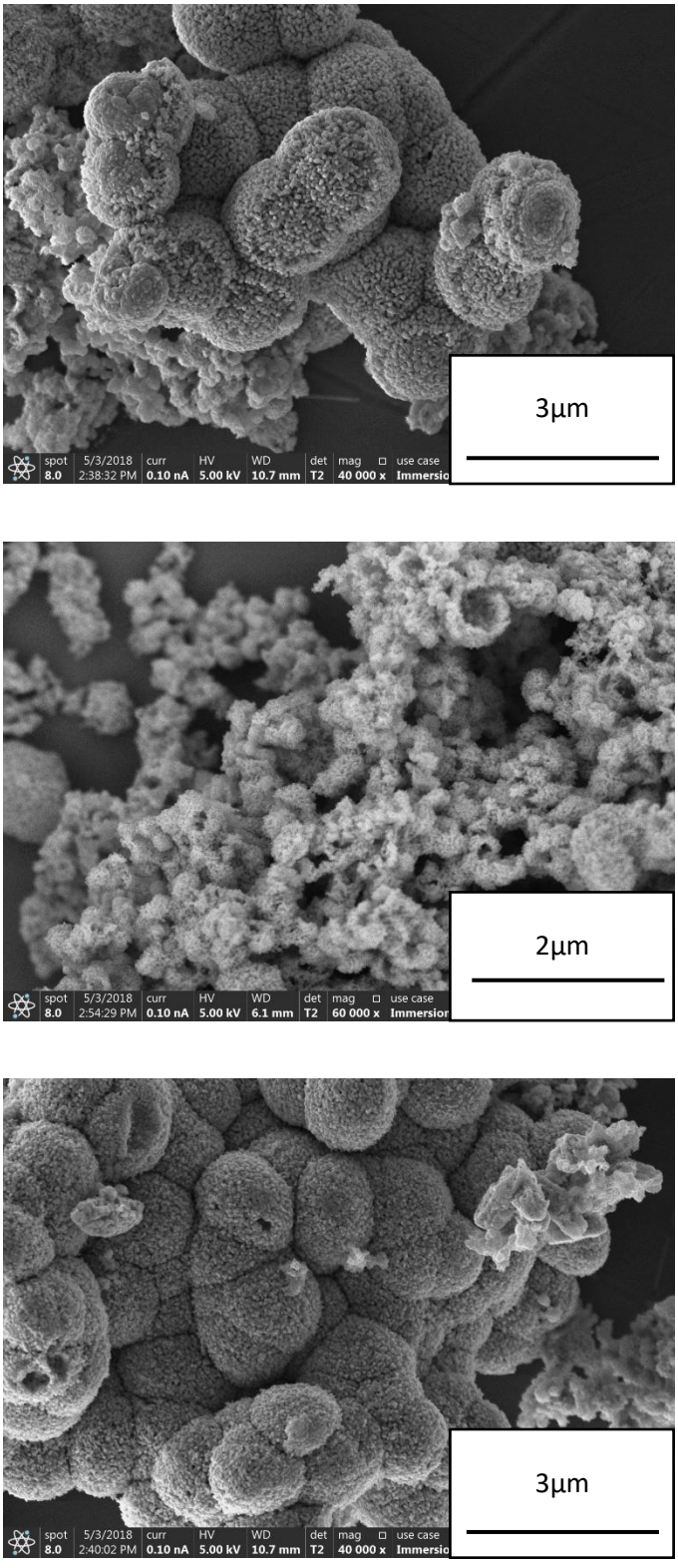

Figure 2.2 SEM images of mesoporous ZnO:Ga

The powder is also examined with TEM to investigate its microstructure and pore morphology. The powder is dispersed in acetone with 30min of mechanical stirring and 30min of ultrasonication. The solution is then dropped onto a thin carbon coated copper TEM grid. **Figure 2.3** show the microstructure images of ZnO:Ga powder. The color contrast in the images demonstrates that the powder is not fully dense. ZnO:Ga particle consists of well dispersed pores and the pore size is about 10-15 nm.

To precisely measure the pore sizes, BET is conducted to characterize the powders and calculate the pore sizes. According to the BET results, pore size graph is obtained as in **Figure 2.4**. The main peak for the pores falls between 10-15 nm.

Finally, to confirm the successful doping of Ga during the synthesis process, EDX is conducted to verity the existence of Ga element in the synthesized powders. Ga is detected according **Figure 2.5**. Because of the close atomic size between Ga (187pm) and Zn (139pm), Ga substitutes Zn during doping.

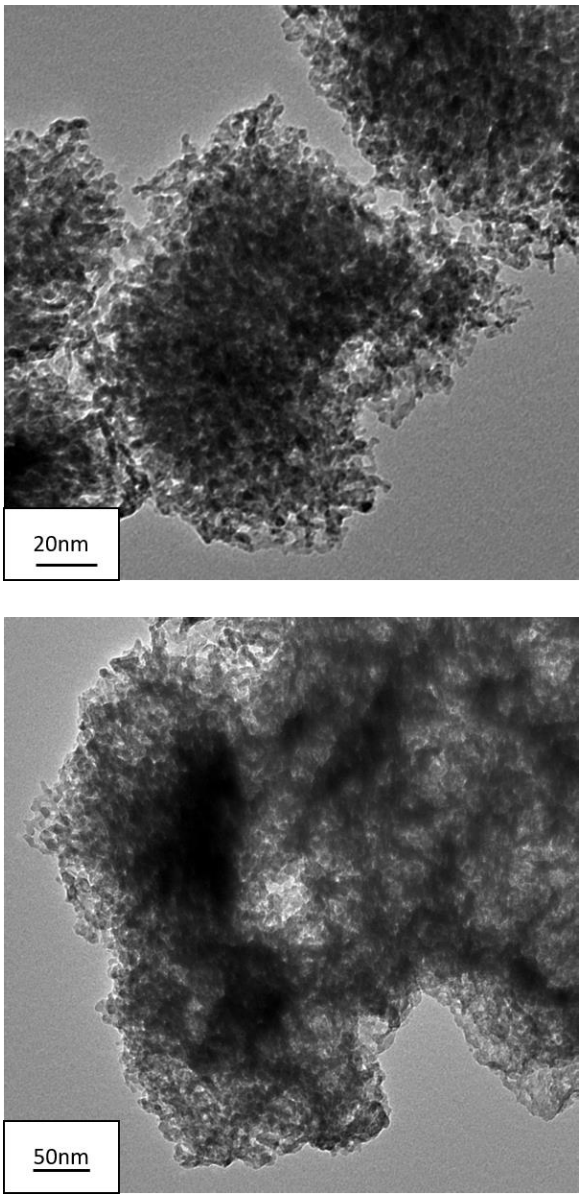

Figure 2.3 TEM images of mesoporous ZnO:Ga

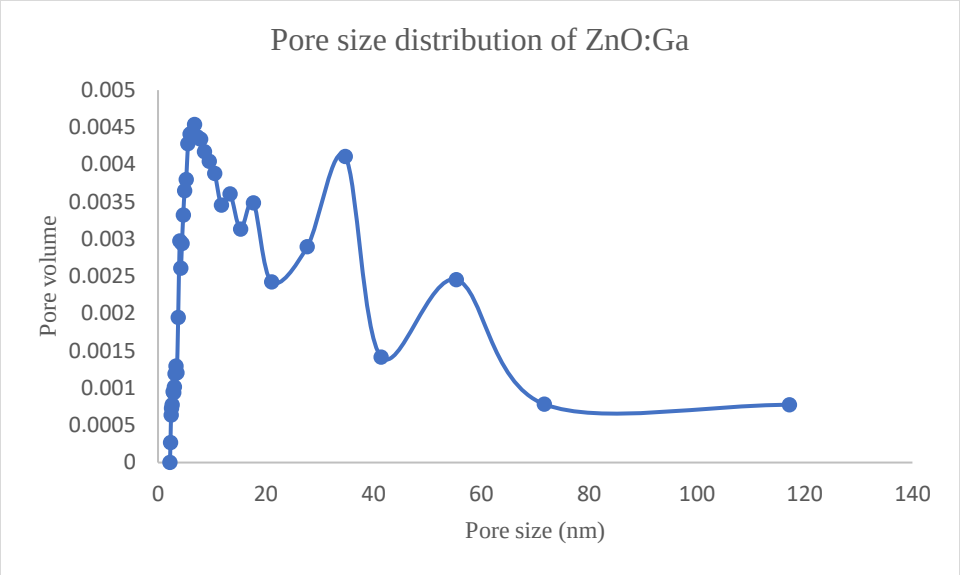

Figure 2.4 BET result of mesoporous ZnO:Ga

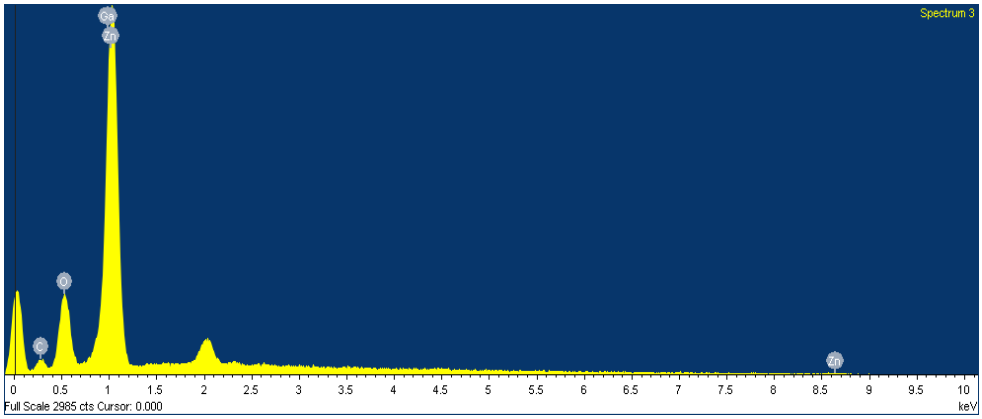

Figure 2.5 EDX result of mesoporous ZnO:Ga

2.3.2 Powder characterizations of Ag/Nb doped TiO_2

The synthesized titanium dioxide powders were first examined with XRD to confirm their phase compositions. The XRD patterns for both materials were shown in **Figure 2.6** and **Figure 2.7**. Despite the dopant differences, the peaks for both materials corresponded to anatase titanium

dioxide (PDF card #00-021-0272). The patterns not only proved that there are no byproducts synthesized during the process but also showed that dopant did not change the crystal structure of TiO_2.

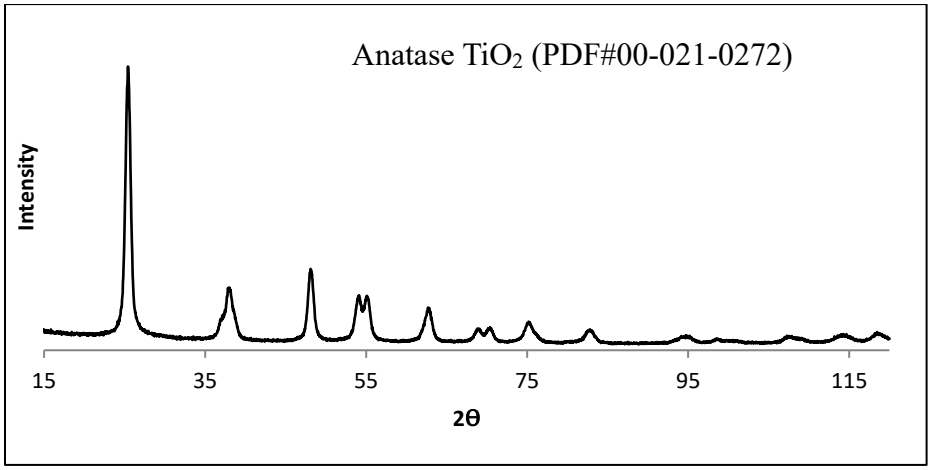

Figure 2.6 XRD pattern for mesoporous TiO_2:Ag

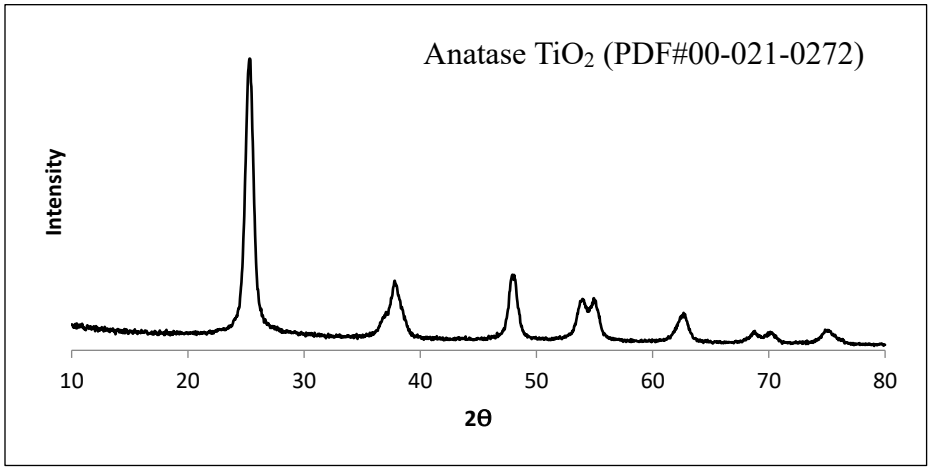

Figure 2.7 XRD pattern for mesoporous TiO_2:Nb

SEM was first conducted to check the particle morphology and particle sizes. **Figure 2.8** show the SEM images of synthesized TiO_2:Ag particles. The particles are uniformly distributed with mesoporous morphology.

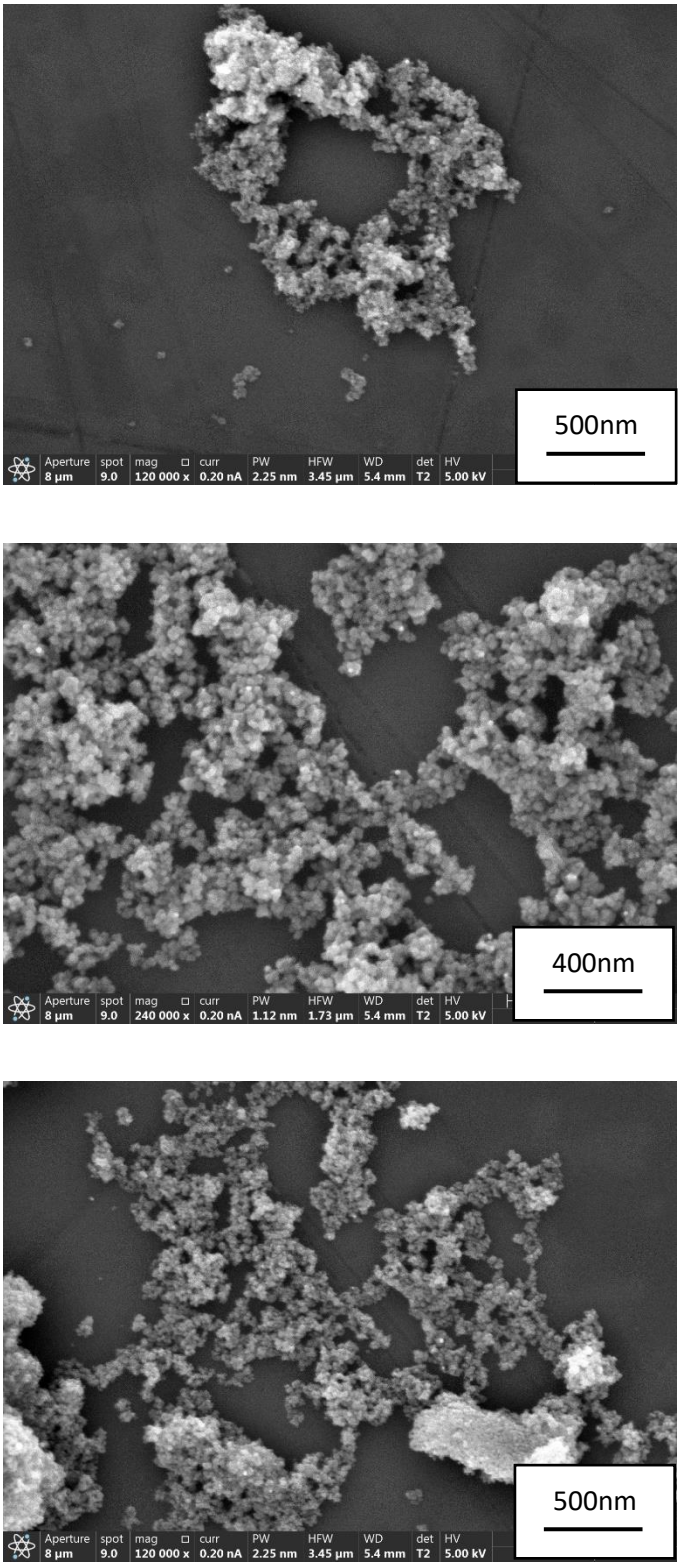

Figure 2.8 SEM images of TiO_2:Ag

In order to further investigate the mesoporous morphologies of TiO_2:Ag and TiO_2:Nb particles, TEM was performed with the synthesized powders. Results from TEM are consistent with SEM images. **Figure 2.9** and **Figure 2.10** both show the TEM images of the TiO_2:Ag and TiO_2:Nb. Similar with mesoporous ZnO:Ga, as shown in the pictures, the contrast indicated the particle was not solid, rather with pores evenly distributed on the surface of the powder. The bright and dark places shown on the image correspond to pore and dense parts of the particle respectively.

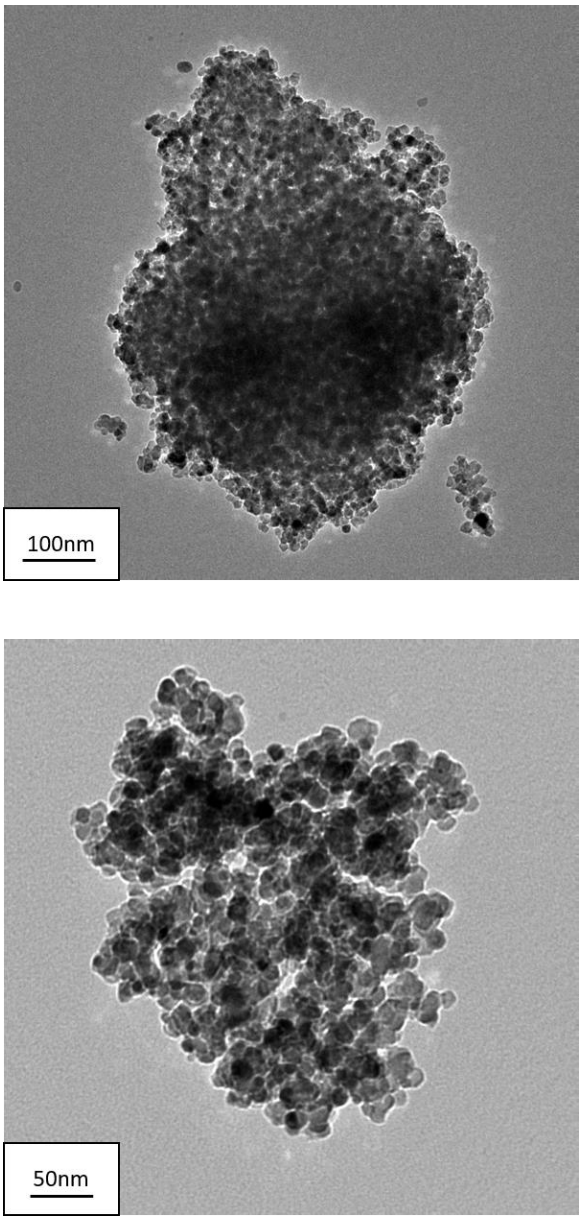

Figure 2.9 TEM images of mesoporous TiO_2:Ag

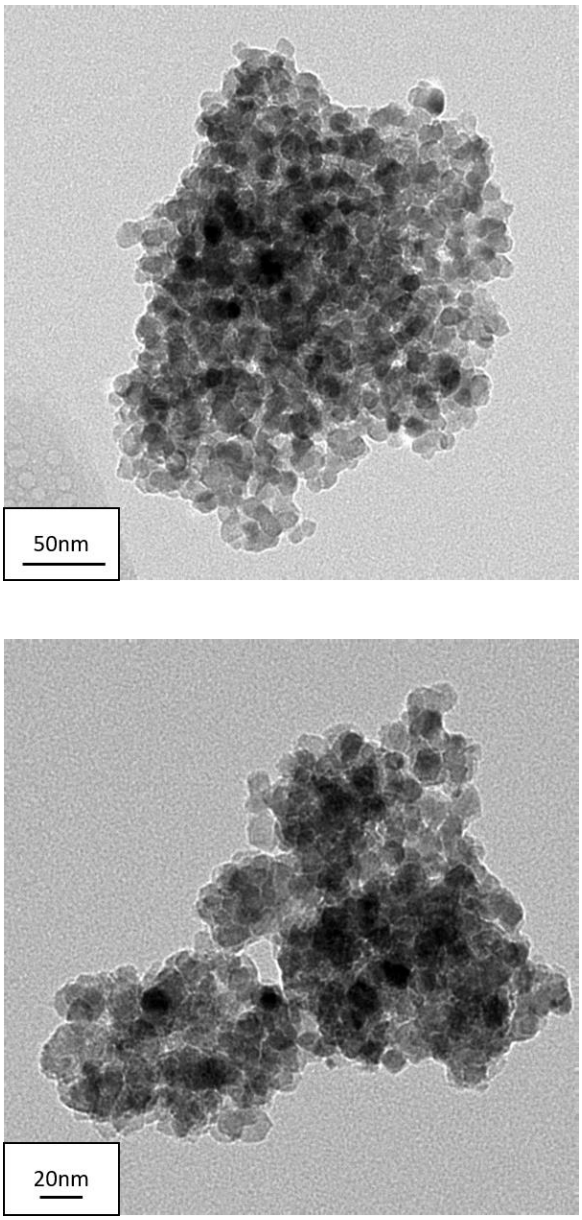

Figure 2.10 TEM images of mesoporous TiO_2:Nb

In order to accurately estimate the pore sizes of the synthesized powders, BET tests with nitrogen gas were conducted to measure the surface area and calculate the pore sizes based on Barrett-Joyner-Halenda (BJH) adsorption and desorption of the pore's calculation method. According to BJH computational calculation, the pore size maximum value is about 9.9nm for Ag

doped titania dioxide (shown in **Figure 2.11**) and 7nm for Nb doped titania dioxide (shown in **Figure 2.12**).

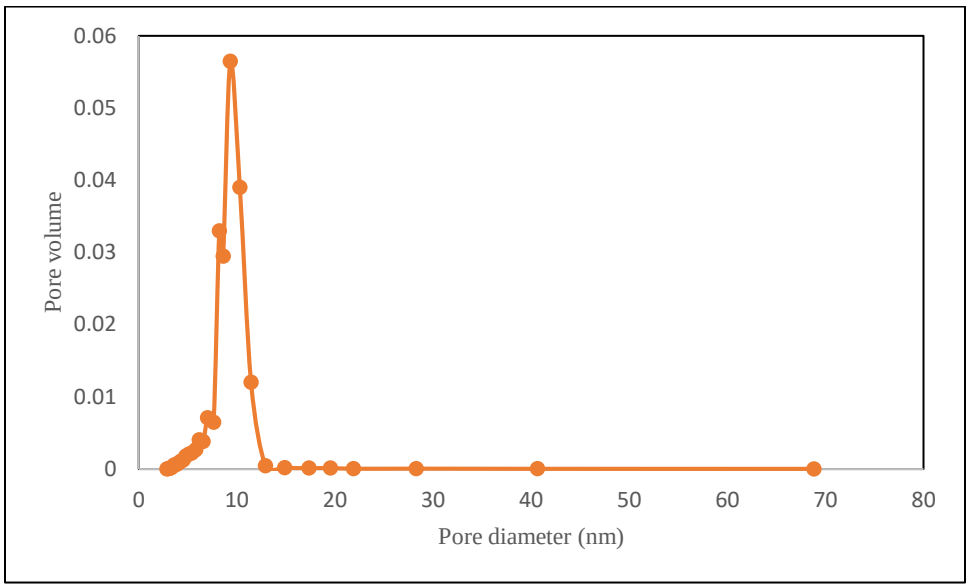

Figure 2.11 Pore size distribution of mesoporous TiO_2:Ag based on BET results

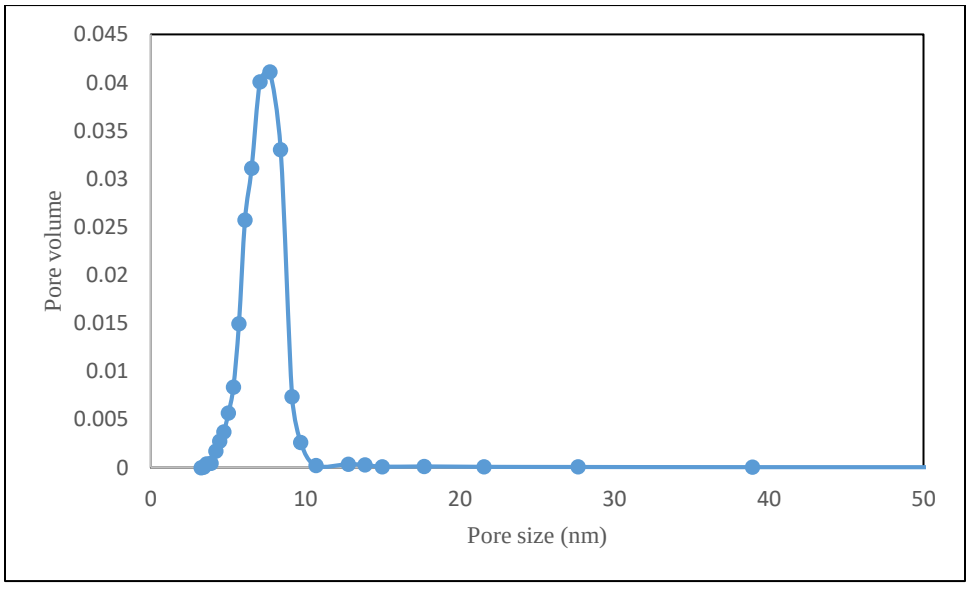

Figure 2.12 Pore size distribution of mesoporous TiO_2:Nb based on BET results

Dopants were added during the experiments to improve their electrical conductivity. To confirm their existence, Energy-dispersive X-ray spectroscopy (EDX) was employed to analyze the component elements. As arrows indicated in **Figure 2.13** and **Figure 2.14**, Ag and Nb have been found existing in each of the powders. The signals from EDX confirmed that the doping process was successful.

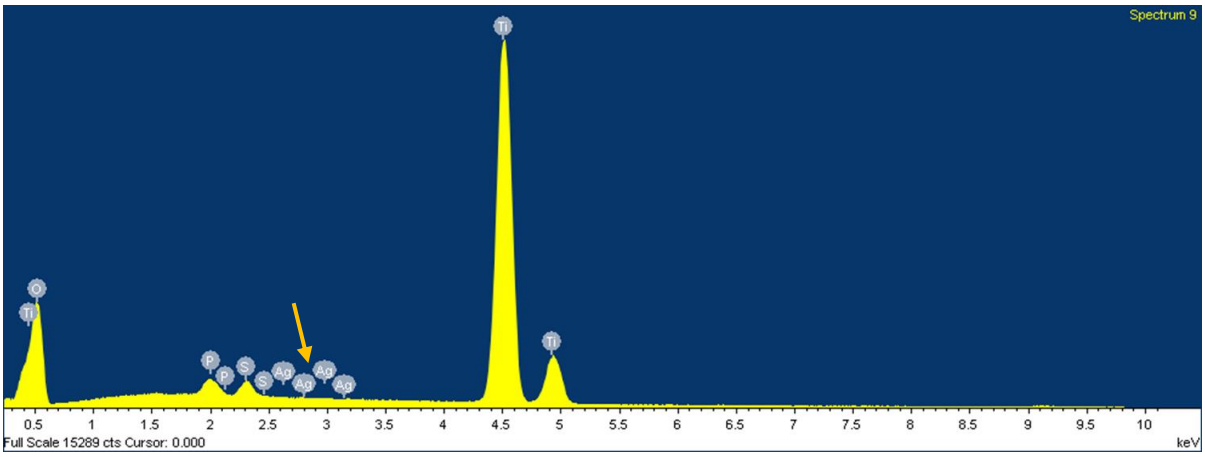

Figure 2.13 EDX for TiO_2:Ag

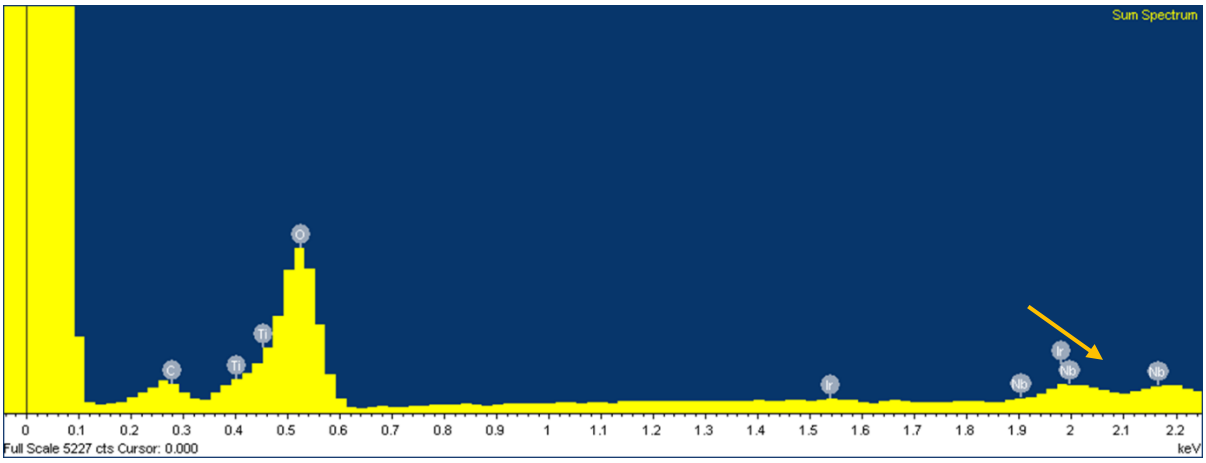

Figure 2.14 EDX for TiO_2:Nb

2.3.3 Powder characterizations of Sn doped In_2O_3

The XRD pattern in **Figure 2.15** shows that the powder is comprised of cubic indium oxide. The pattern shows all sharp peaks demonstrating the synthesized powder is highly crystal. Small amount of Sn (4%) doping did not change the crystal structure of indium oxide. All peaks correspond to cubic indium oxide (pdf card#00-066-0416). The XRD result also confirms that the final powders contain successful Sn dopant.

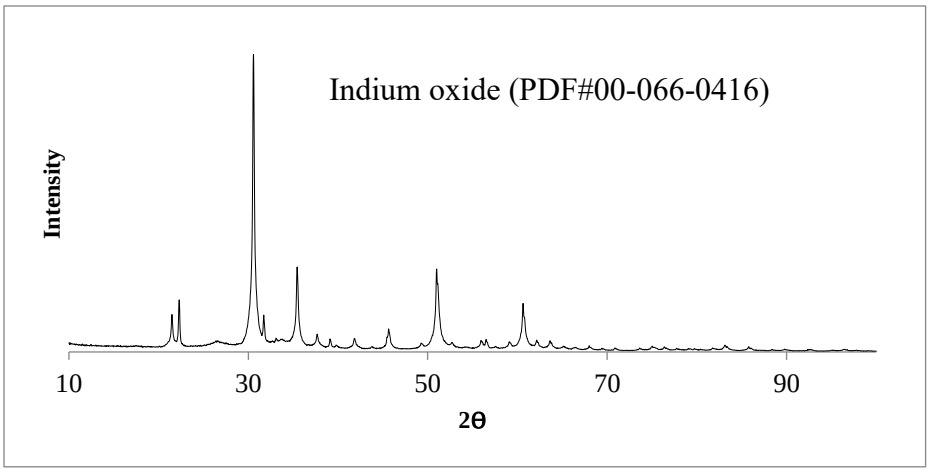

Figure 2.15 XRD pattern for Sn doped In_2O_3

While it shows cubic indium oxide phase according to XRD pattern, EDX is performed to further support the doping exitance. **Figure 2.16** shows distinguishable strong Sn signal.

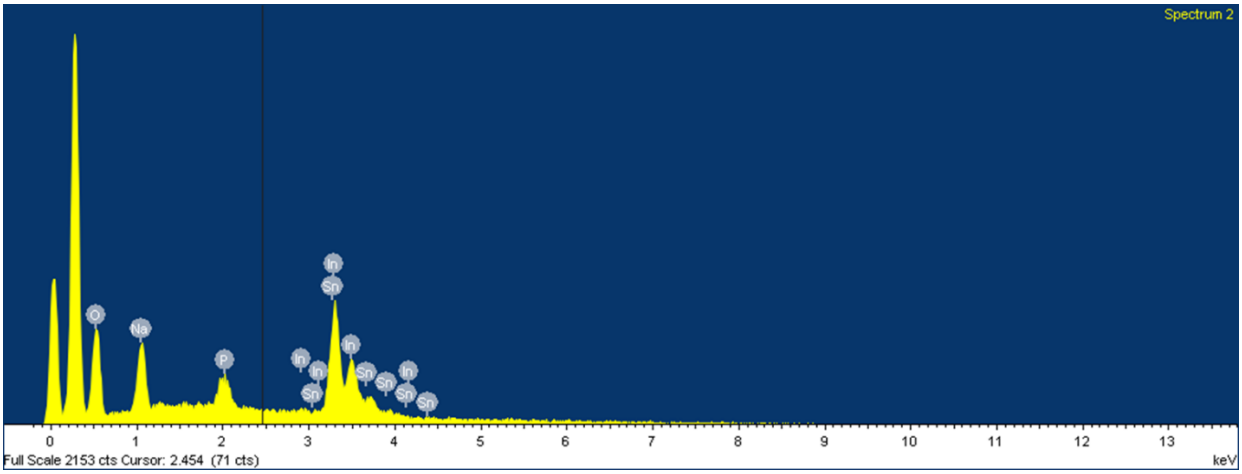

Figure 2.16 EDX pattern for Sn doped In_2O_3

SEM images of synthesized In2O3:Sn is shown in **Figure 2.17.** It can be seen that they have well organized mesoporous pore morphology.

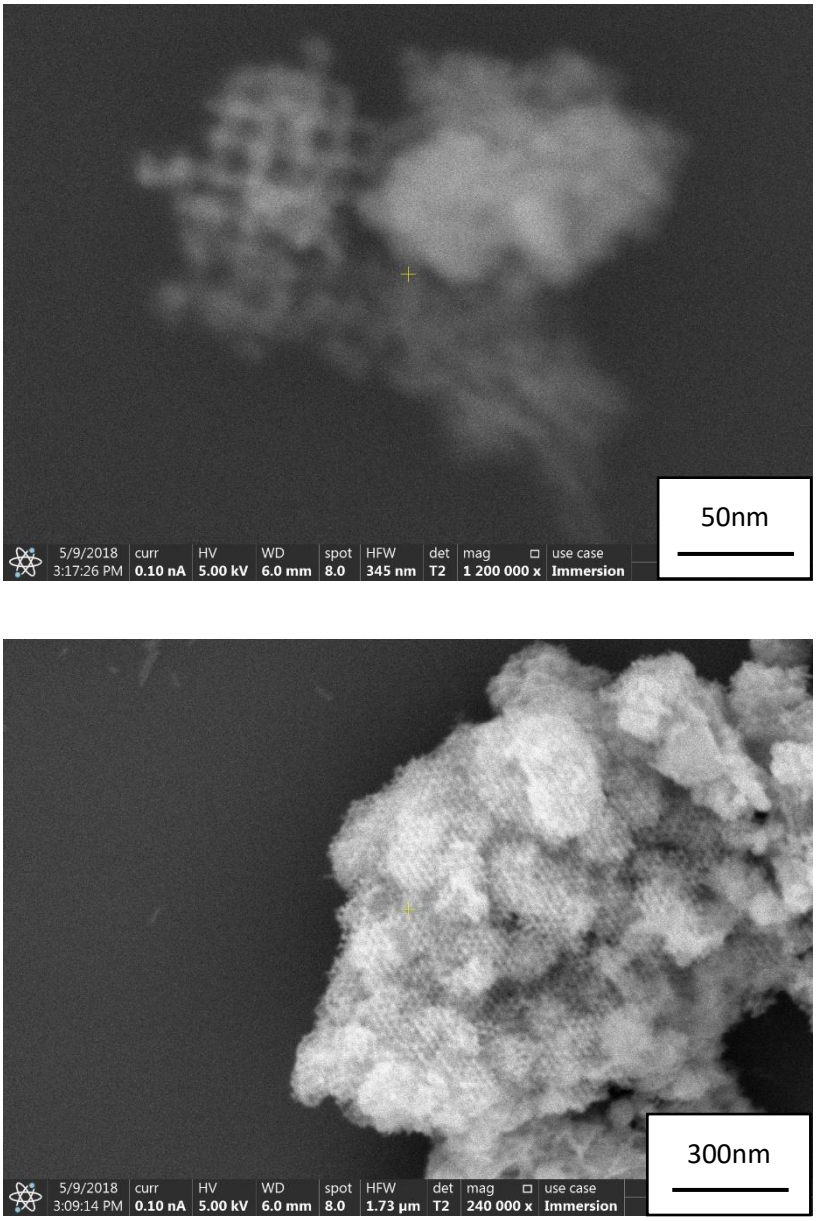

Figure 2.17 SEM images of mesoporous In_2O_3:Sn

In order to better visualize the pores distribution and pore mophology on the particle, TEM characterizations were also conducted. Synthesized KIT-6 was first investigated to confirm the template mophology. Mesoporous silica has the advantage of large pore volume, uniform pore distribution and structure, besides, it also shows good stability under hydrothermal reaction [293,

294, 295]. KIT-6 is a cubic Ia$\bar{3}$d phase with 3-dimentional mophology mesoporous silica [113, 296]. The morphology of synthesized KIT-6 is analysed with TEM and the images are shown in **Figure 2.18**. As illustrated in **Figure 2.18**, synthesized mesoporous silica shows highly ordered mesoporous topology. It has good amount of pores distributed evenly on the particle while maintain interconnective channels between pores. Since the method for producing mesoporous In_2O_3:Sn is hard-template method with KIT-6 as template. The final morphologies of the pore present well organized and highly ordered structures. The TEM images in **Figure 2.19** clearly show the mesoporous and well-ordered morphology of synthesized In_2O_3:Sn particles. A successful 3D framework of mesoporous In_2O_3 intermediate has been obtained based on the TEM images.

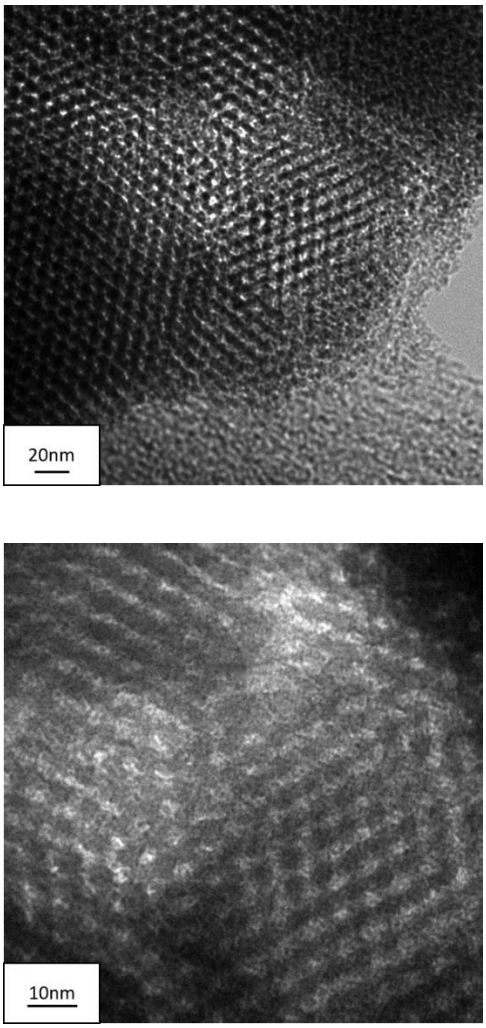

Figure 2.18 TEM images of mesoporous KIT-6

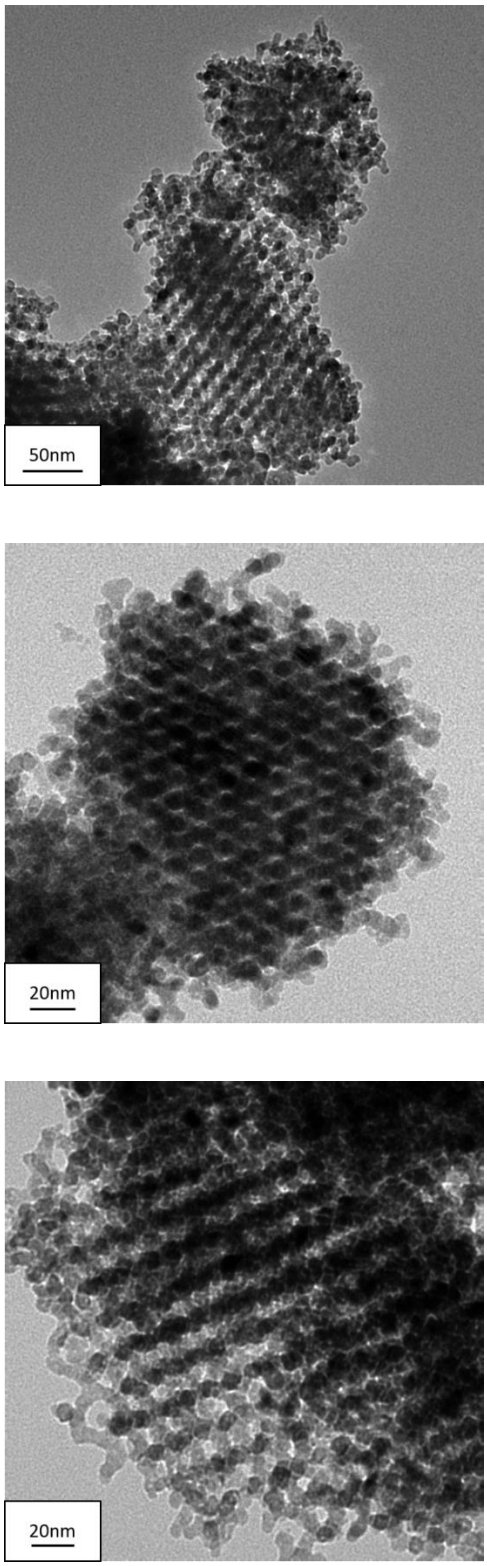

Figure 2.19 TEM images of Sn doped In_2O_3

Same with the previous discussed materials, BET analysis was also conducted to investigate the powder surface area and pore sizes. The isotherm graph of nitrogen adsorption–desorption in **Figure 2.20** indicates type IV isotherm [297, 298]. According to BJH computational calculation method, the pore size distribution for mesoporous indium tin oxide is plotted in **Figure 2.20**. The pore-size maximum value is found to be around 15nm.

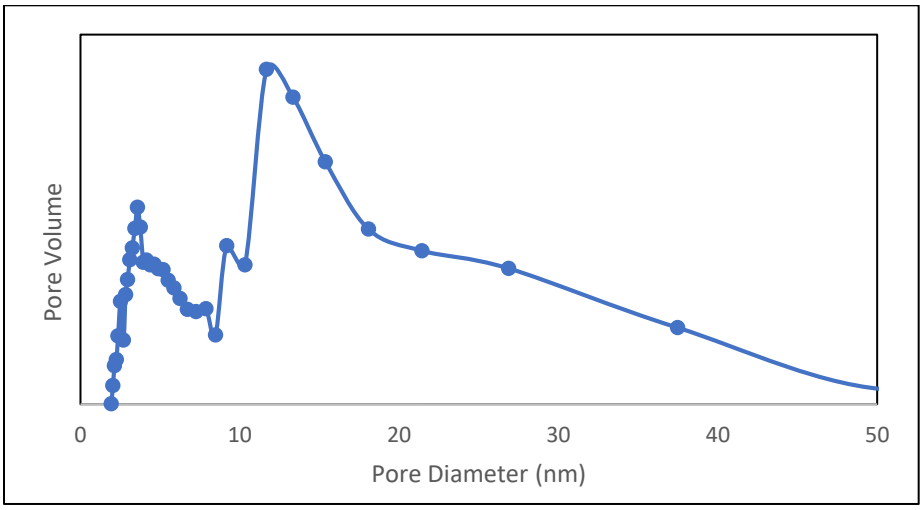

Figure 2.20 Pore size distribution of mesoporous In_2O_3:Sn

Chapter 3 Electrical conductivity of mesoporous ceramic suspensions with pH variations

The electrical conductivities of all four ceramic suspensions with different powder volume fractions and pH values are measured. Powders are dispersed in buffer solutions with three different concentrations. To realize stable dispersion, they are dispersed in buffer solutions by overnight magnetic stirring and 2h ultra sonication.

3.1 TEM images of TiO_2:Ag, TiO_2:Tb, ZnO:Ga and In_2O_3:Sn particles after dispersing in different pH solutions

To confirm that mesoporous materials keep their morphologies unchanged when dispersed in different pH buffer solutions, TEM images were taken for each of the four materials after they are placed in buffer solutions for overnight. **Figure3.1** shows the TEM images of Ag doped TiO_2 dispersed in different pH valued solutions. As shown from the images, TiO_2 is stable regardless of dispersion solution pH changes. It remains mesoporous morphologies from pH3-pH9.

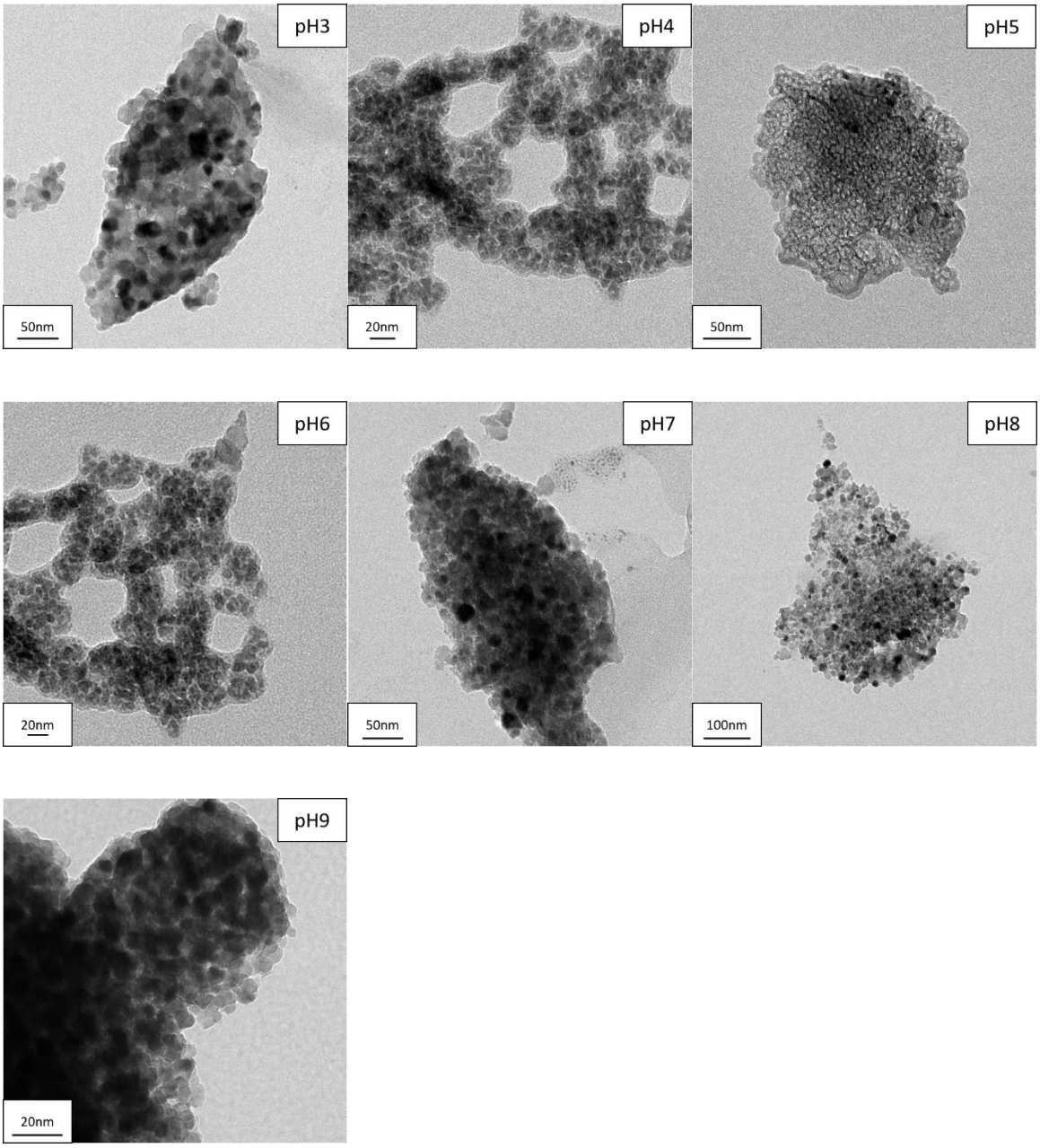

Figure 3.1 TEM images of mesoporous TiO_2:Ag dispersed in pH3-pH9 solutions

ZnO:Ga is also very stable with different buffer solutions. The mesoporous morphologies remain not damaged in seven different solutions. TEM images of mesoporous ZnO:Ga dispersed in different pH solutions are shown in **Figure 3.2**.

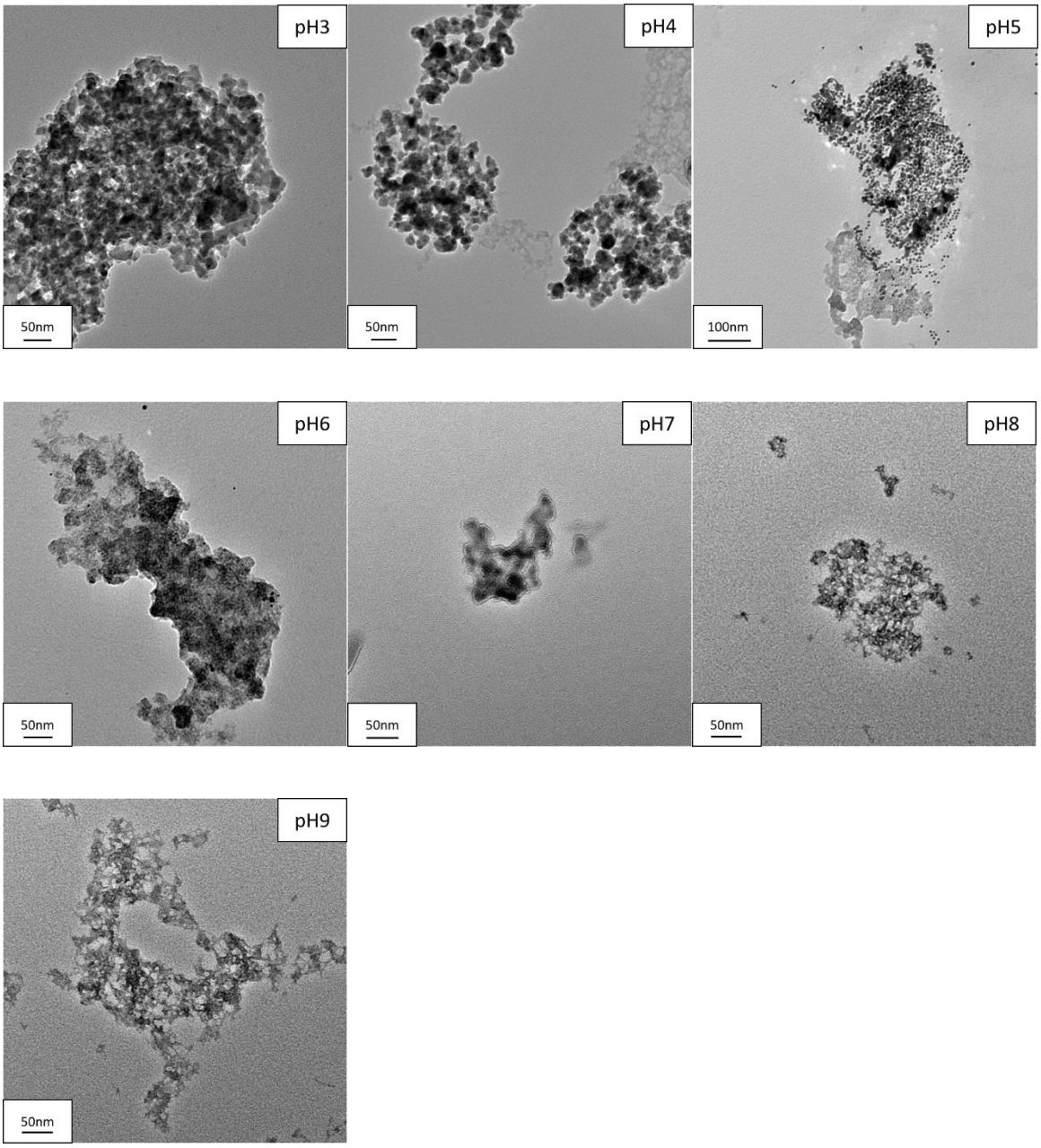

Figure 3.2 TEM images of mesoporous ZnO:Ga dispersed in pH3-pH9 solutions

In_2O_3:Sn is a little bit unstable when dispersed in pH3 and pH9 solutions, the mesoporous morphology gets little changed within these two extreme pH solutions. However, it remains stable in other conditions. Overall, In_2O_3:Sn still remains mesoporous morphology in different buffer solutions. The TEM images of In_2O_3:Sn in different pH solutions are shown below in **Figure 3.3**.

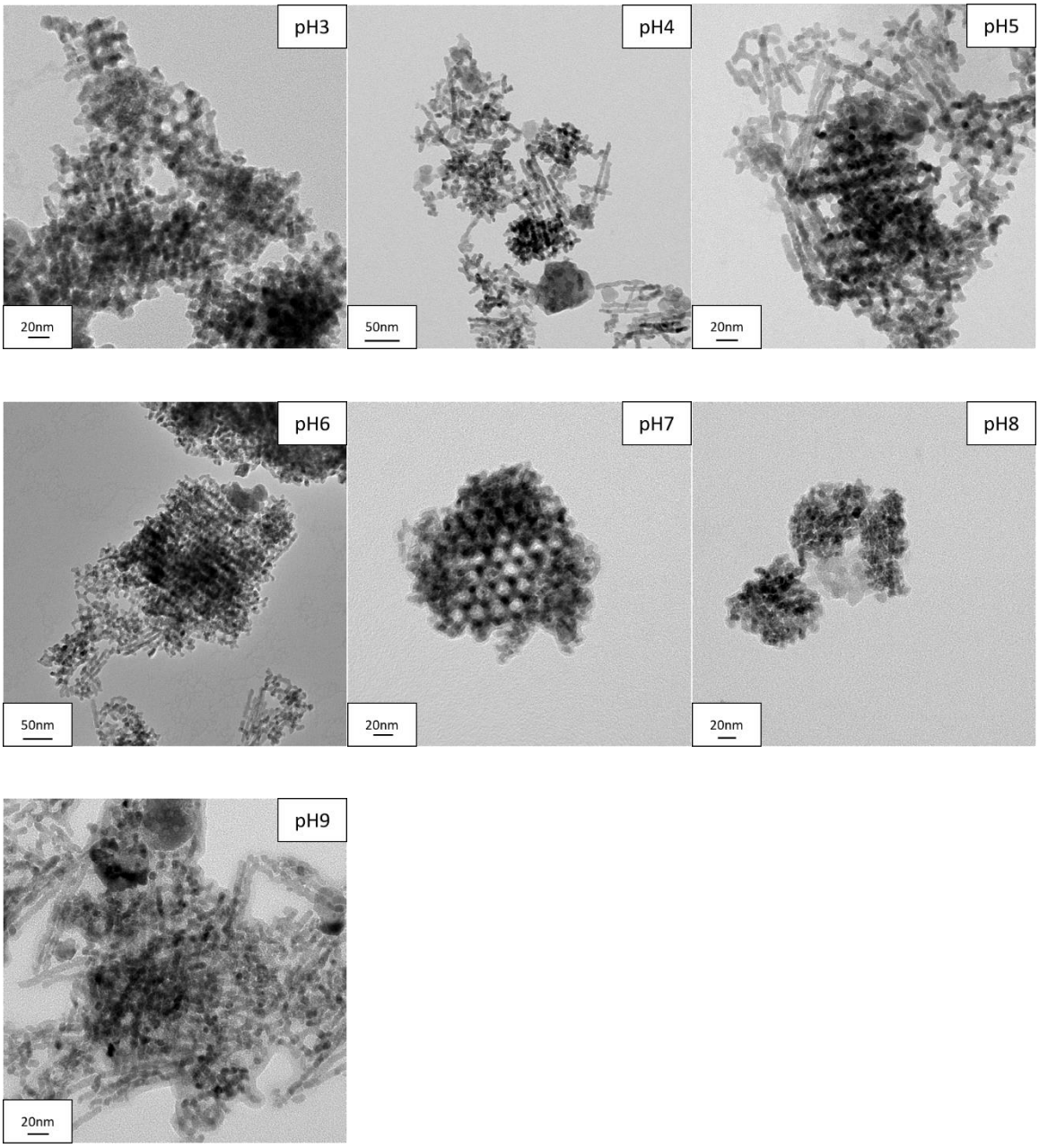

Figure 3.3 TEM images of mesoporous In_2O_3:Sn dispersed in pH3-pH9 solutions

3.2 Electrical conductivities of ceramic suspensions

3.2.1 stable suspension preparation

Three different powder volume fractions (0.125vol%, 0.25vol% and 1vol%) of ceramic suspensions were prepared and their electrical conductivities as well as particle sizes were tested. Powders were weighed precisely and mixed with buffer solutions. Powders were dispersed in buffer solutions ranging from pH3 to pH9. Overnight magnetic stirring and 4 hours of strong ultrasonication were applied to the suspension to guarantee good stability. Visual observation was applied to check the nanofluids stability. No large sedimentation in the nanofluids was seen after 5h.

3.2.2 Electrical conductivities of suspensions

Electrical conductivities of Ag/Nb doped TiO_2 suspensions are drawn in **Figure 3.4a and Figure 3.4b**. Total of seven different pH values were tested with three different powder volume fractions including 0.125vol%, 0.25vol% and 1vol%. It shows different trend regarding pH changes. For solutions at pH 3-6 (acidic solution), the electrical conductivity increases as concentration increases, however, it behaves opposite in basic solution (pH 7-pH 9). Overall, the electrical conductivity of basic suspension is higher than acidic suspension.

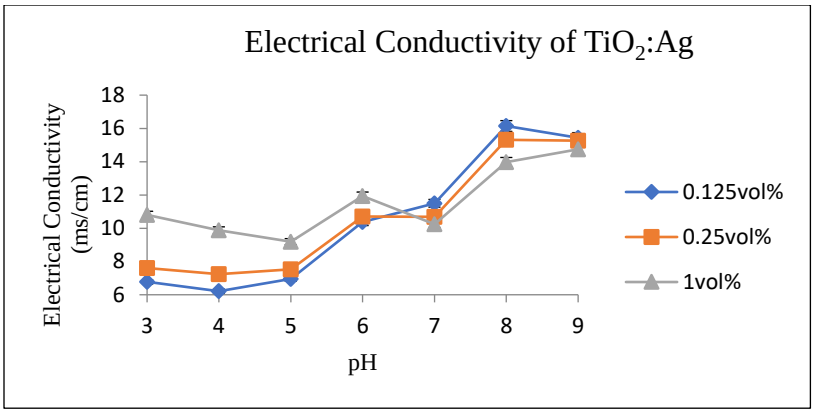

Figure 3.4a, Electrical conductivities of mesoporous TiO_2:Ag suspensions with different volume fractions from pH3-pH9

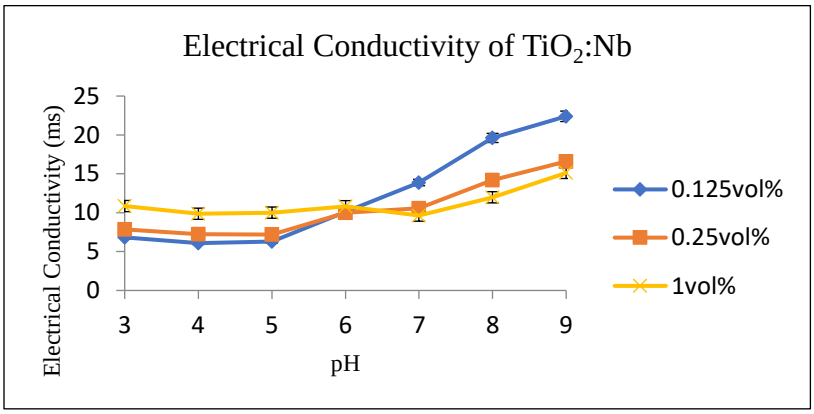

Figure 3.4b, Electrical conductivities of mesoporous TiO_2:Nb suspensions with different volume fractions from pH3-pH9

Figure 3.4 Electrical conductivities of TiO_2:Ag/TiO_2:Nb suspensions from pH 3-pH 9 at powder volume fractions of 0.125vol%, 0.25 vol% and 1 vol%

Electrical conductivity results for Ga doped ZnO are shown in **Figure 3.5**. With concentration increases from 0.125vol%, 0.25vol% to 1vol%, the electrical conductivity decreases in both acidic and basic solutions. Similar as Ag/Nb doped TiO_2 solutions, electrical conductivities of suspensions are higher when they are in basic conditions than acidic ones.

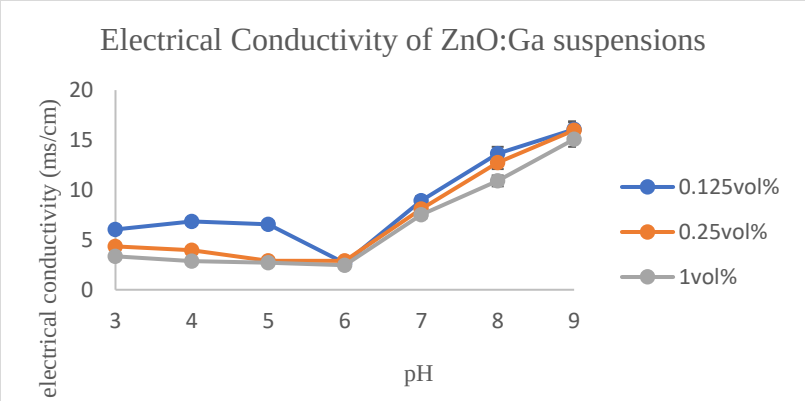

Figure 3.5 Electrical conductivity of mesoporous ZnO:Ga suspensions from pH 3-pH 9 at powder volume fractions of 0.125vol%, 0.25 vol% and 1 vol%

Figure 3.6 shows the electrical conductivity of Sn doped In_2O_3 nanofluids with different pH values. Three different volume fractions (0.125vol%, 0.25vol% and 1vol%) were tested. Despite changes in concentrations, the electrical conductivities remain almost the same.

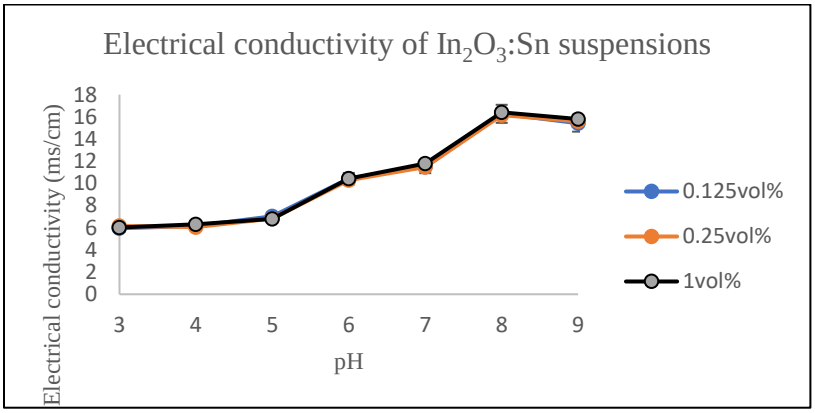

Figure 3.6 Electrical conductivity of mesoporous In_2O_3:Sn suspensions from pH 3-pH 9 at powder volume fractions of 0.125vol%, 0.25 vol% and 1 vol%

Chapter 4 Particle sizes analysis of four ceramic suspensions

While measuring their electrical conductivities, the particle size distributions of suspensions are measured with DLS as well. Powders are dispersed in buffer solutions (pH3-pH9) with three different concentrations (0.125vol%, 0.25vol% and 1vol%). Their particle sizes and zeta potentials are measured using a DLS machine. Particle size distributions are shown as below.

4.1 DLS and particle sizes of Ag doped TiO_2

Figure 4.1 and **Figure 4.2** shows the DLS results for TiO_2:Ag suspensions. **Figure 4.1** represents the DLS results of TiO_2:Ag with 0.125vol% volume fraction. **Figure 4.2** represents the DLS results of TiO_2:Ag suspension with larger volume fractions. The specific particle sizes with different volume fractions when dispersed in different pH buffer solutions are summarized in **Table 4.1**.

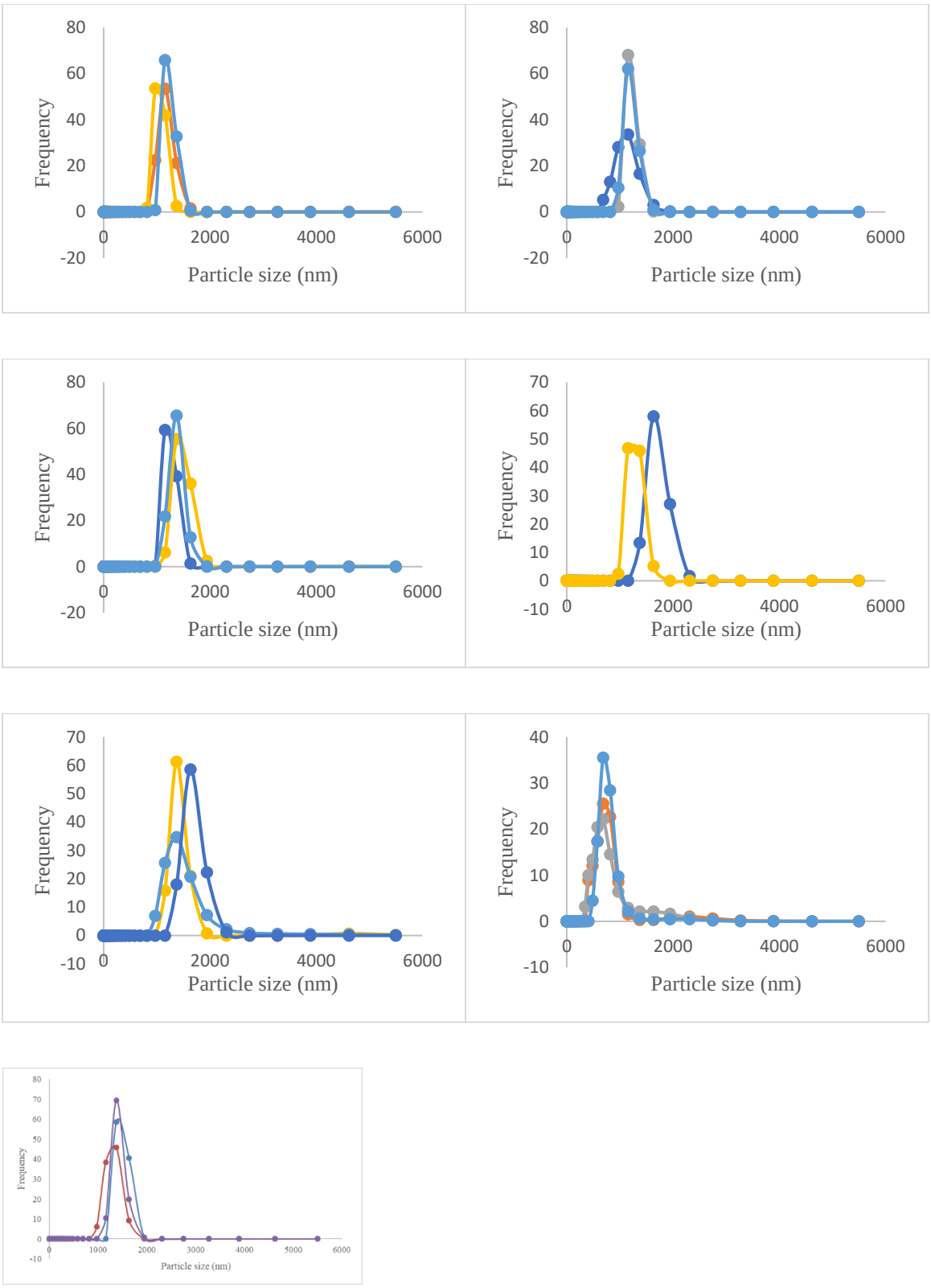

Figure 4.1 Particle size distributions of TiO_2:Ag with 0.125vol% concentration in pH3-pH9 solutions

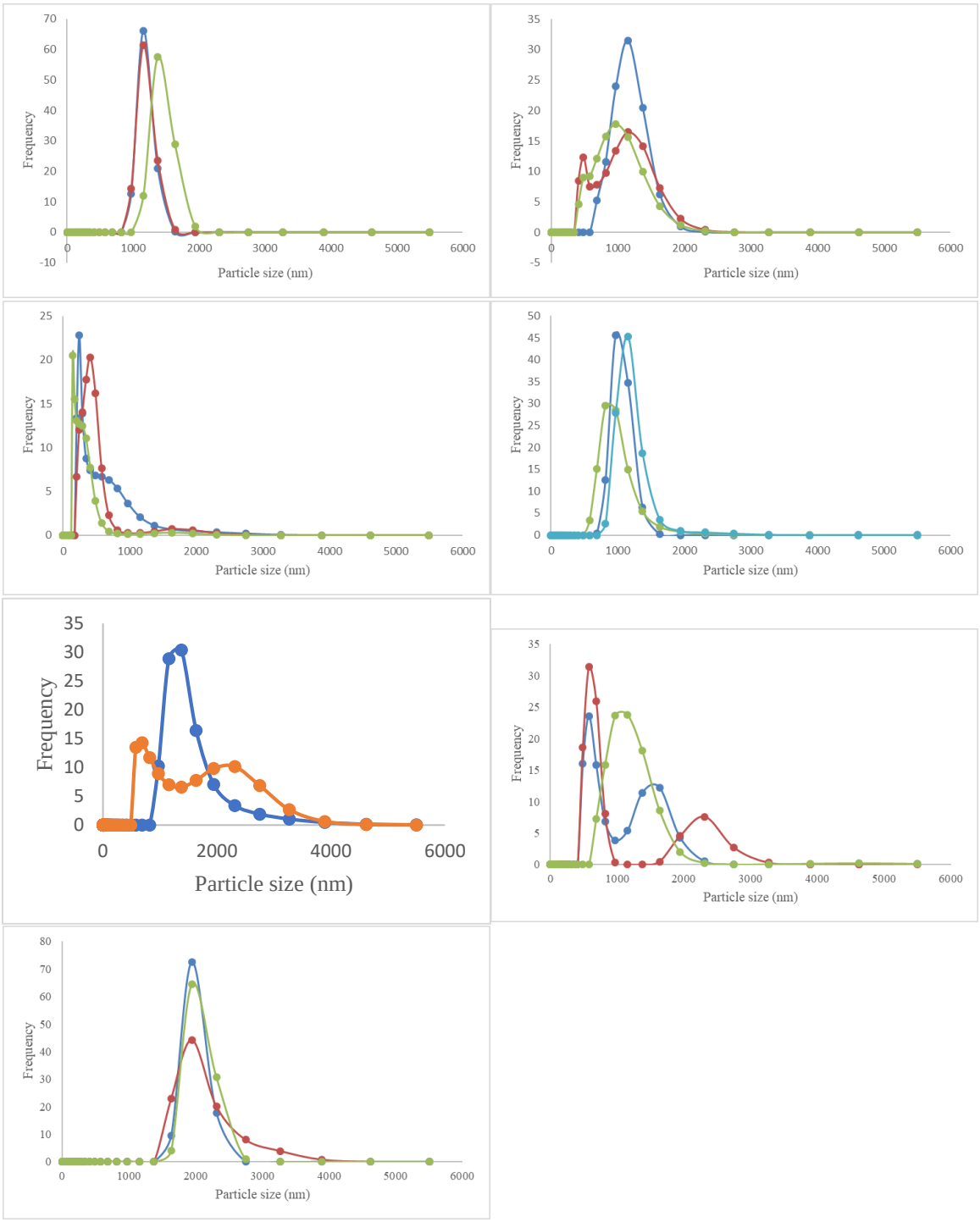

Figure 4.2 DLS results for TiO_2:Ag with 0.25vol% concentration in pH3-pH9

Table 4.1 Particles size summary of 0.125vol% and 0.25vol% TiO_2:Ag suspensions (particle size: nm)

pH / PVF	3	4	5	6	7	8	9
0.125vol	950-970	100-140	100-120	70-80	1100-1600	900-1100	1100-1300
0.25vol%	500-680	70-120	90-100	1000-2000	1400-2000	1300-1600	1300-1500
1vol%	250-350	50-70	45-55	1700-1900	1800-1900	1700-1860	1550-1610

4.2 DLS and particle sizes of TiO_2:Nb

Particles sizes of TiO_2:Nb are also analyzed with DLS equipment. Specific results of the particle size of different concentration suspensions are shown as below in **Figure 4.3** and **Figure 4.4** A summary table of particle sizes is also attached as **Table 4.2**.

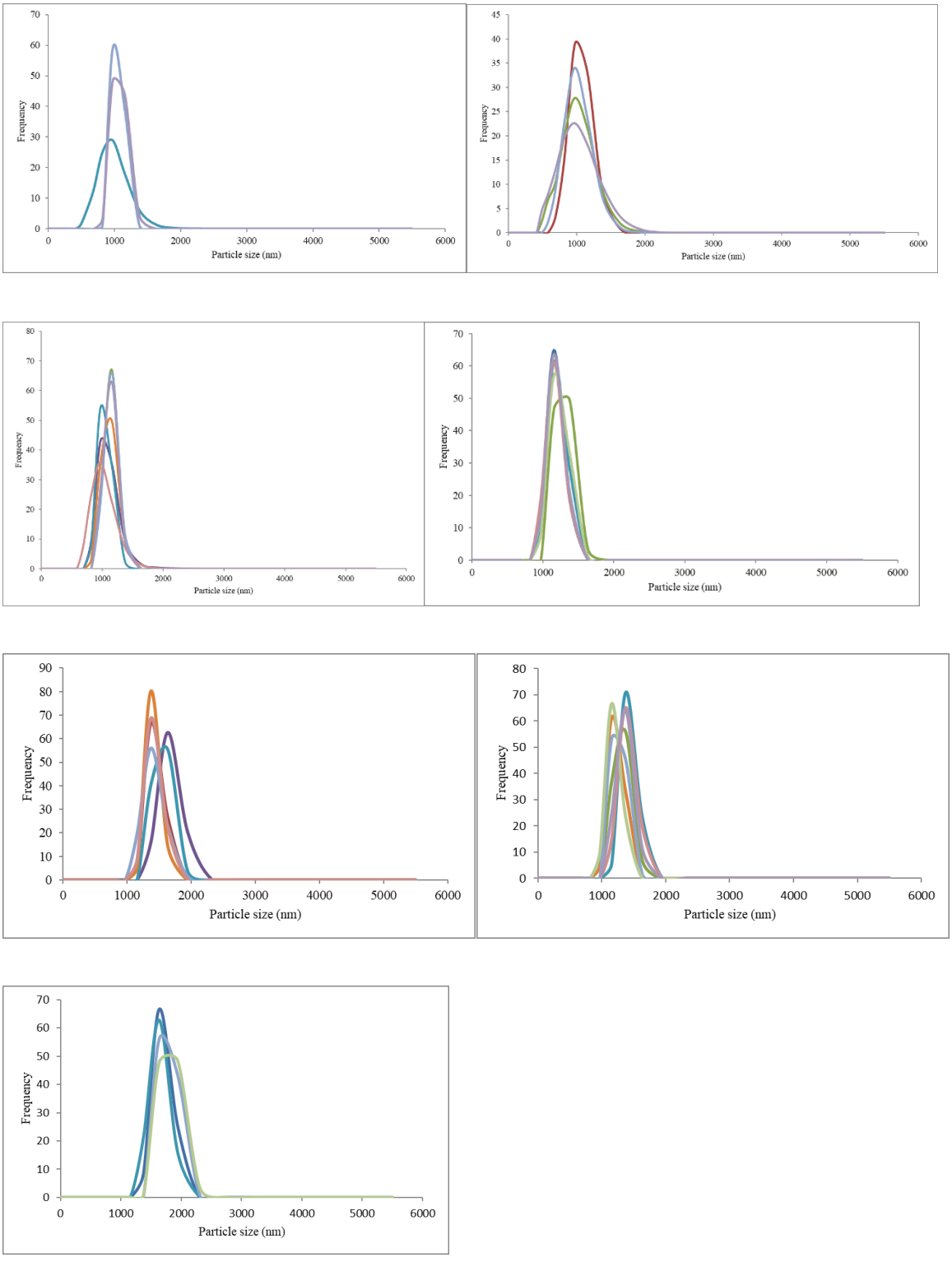

Figure 4.3 DLS results for TiO_2:Nb with 0.125vol% concentration in pH3-pH9

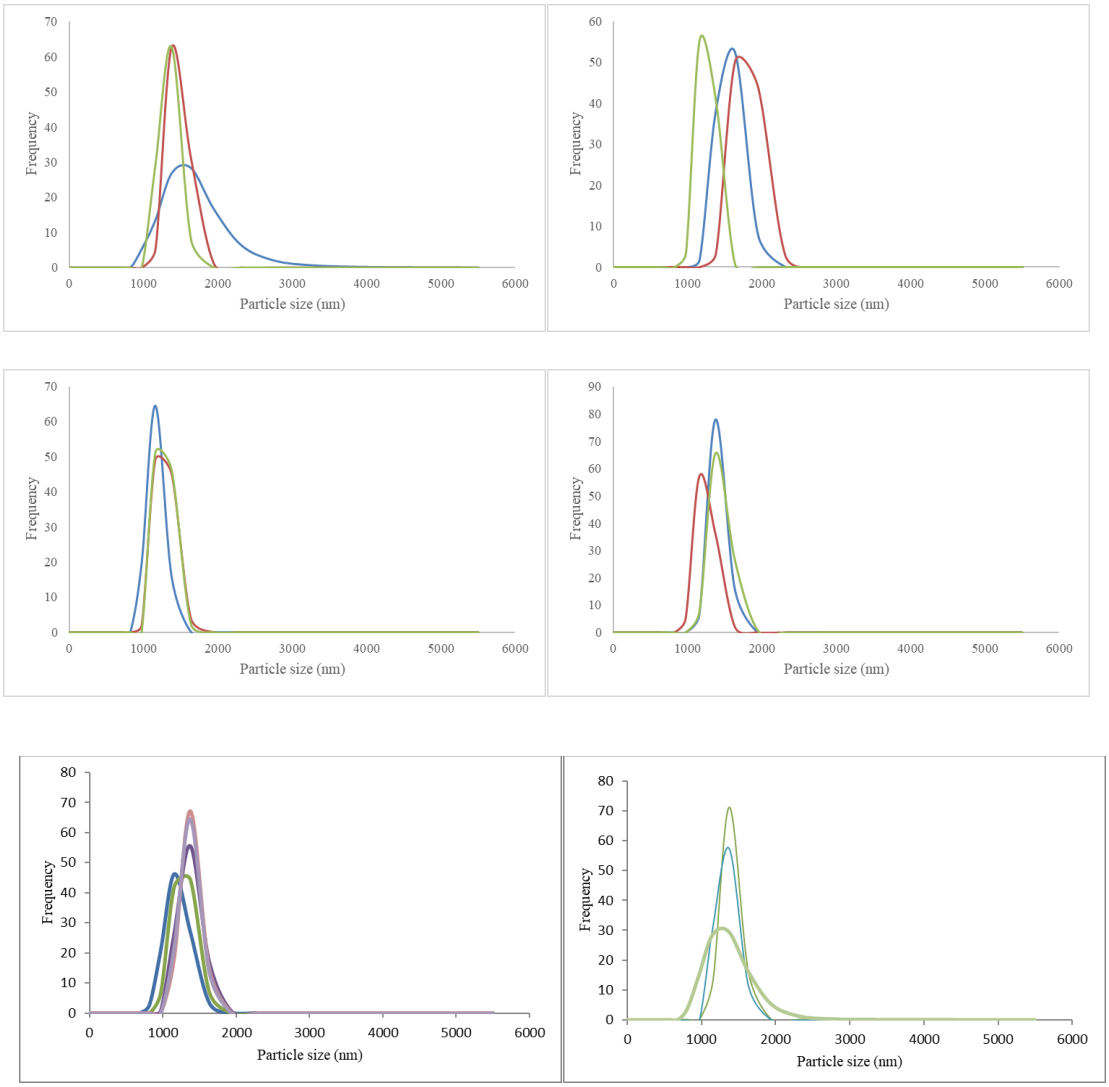

Figure 4.4 DLS results for TiO_2:Nb with 0.25vol% concentration in pH3-pH9

Table 4.2 Particles size summary of 0.125vol% and 0.25vol% TiO_2:Nb suspensions (particle size: nm)

pH	3	4	5	6	7	8	9
0.125vol%	800-980	980-1100	330-800	800-1000	800-1100	1100-1300	1000-1300
0.25vol%	680-820	300-500	500-600	700-900	1300-1600	1300-1600	1200-1600
1vol%	400-600	200-300	310-490	640-760	1500-1700	1650-1750	1600-1960

4.3 DLS and particle sizes of Ga doped ZnO

While measuring the electrical conductivities of ZnO:Ga suspensions. The particle sizes of ZnO:Ga are also analyzed and compared with two different concentrations (0.125vol% and 0.25vol%). Results are summarized as below in **Figure 4.5** and **Figure 4.6**. **Figure 4.5** shows the DLS measurements of 0.125vol% and **Figure 4.6** shows the DLS measurements of 0.25vol%. A summary of particle size in each buffer solution with different concentrations are shown in **Table 4.3**.

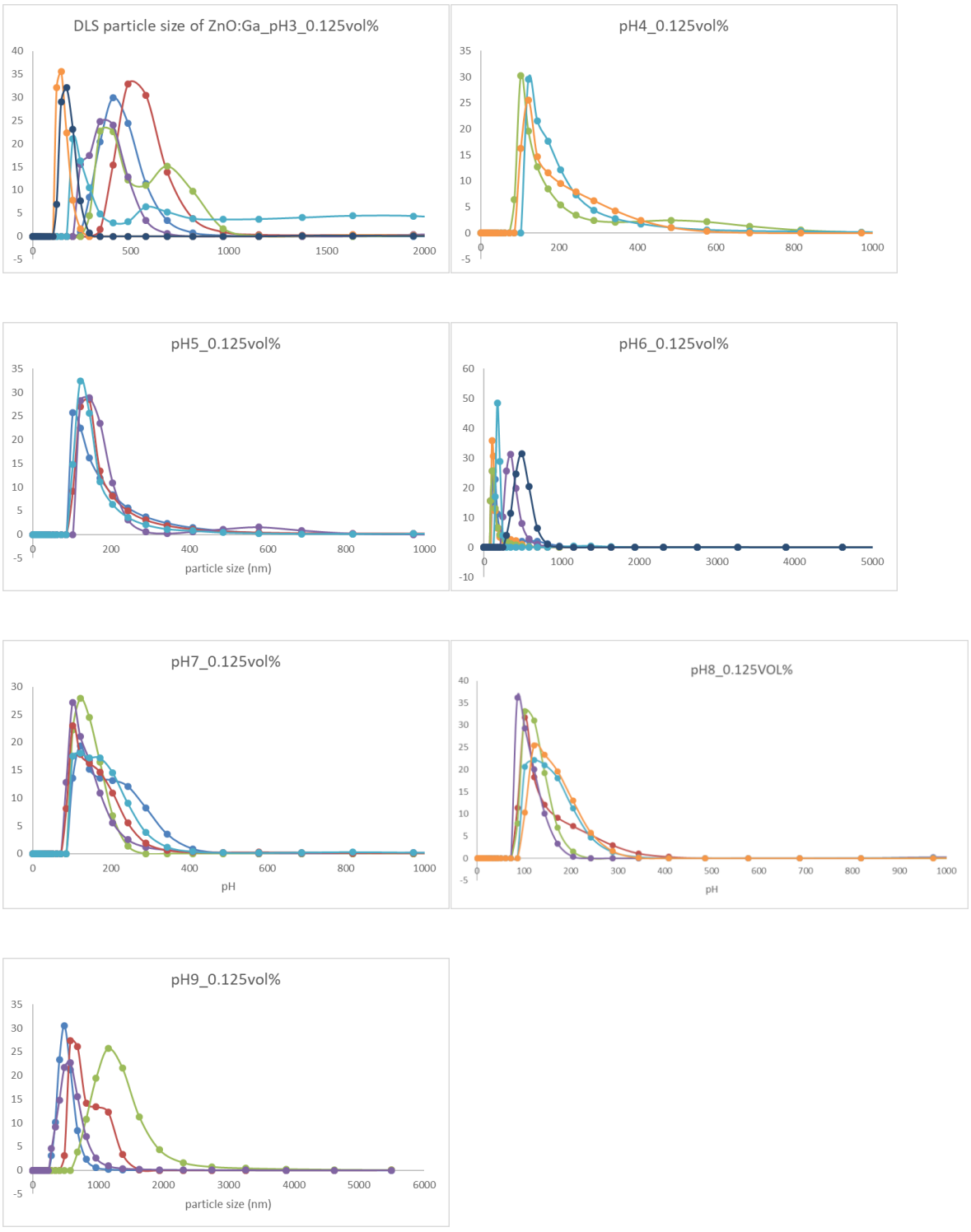

Figure 4.5 DLS results for ZnO:Ga with 0.125vol% concentration in pH3-pH9

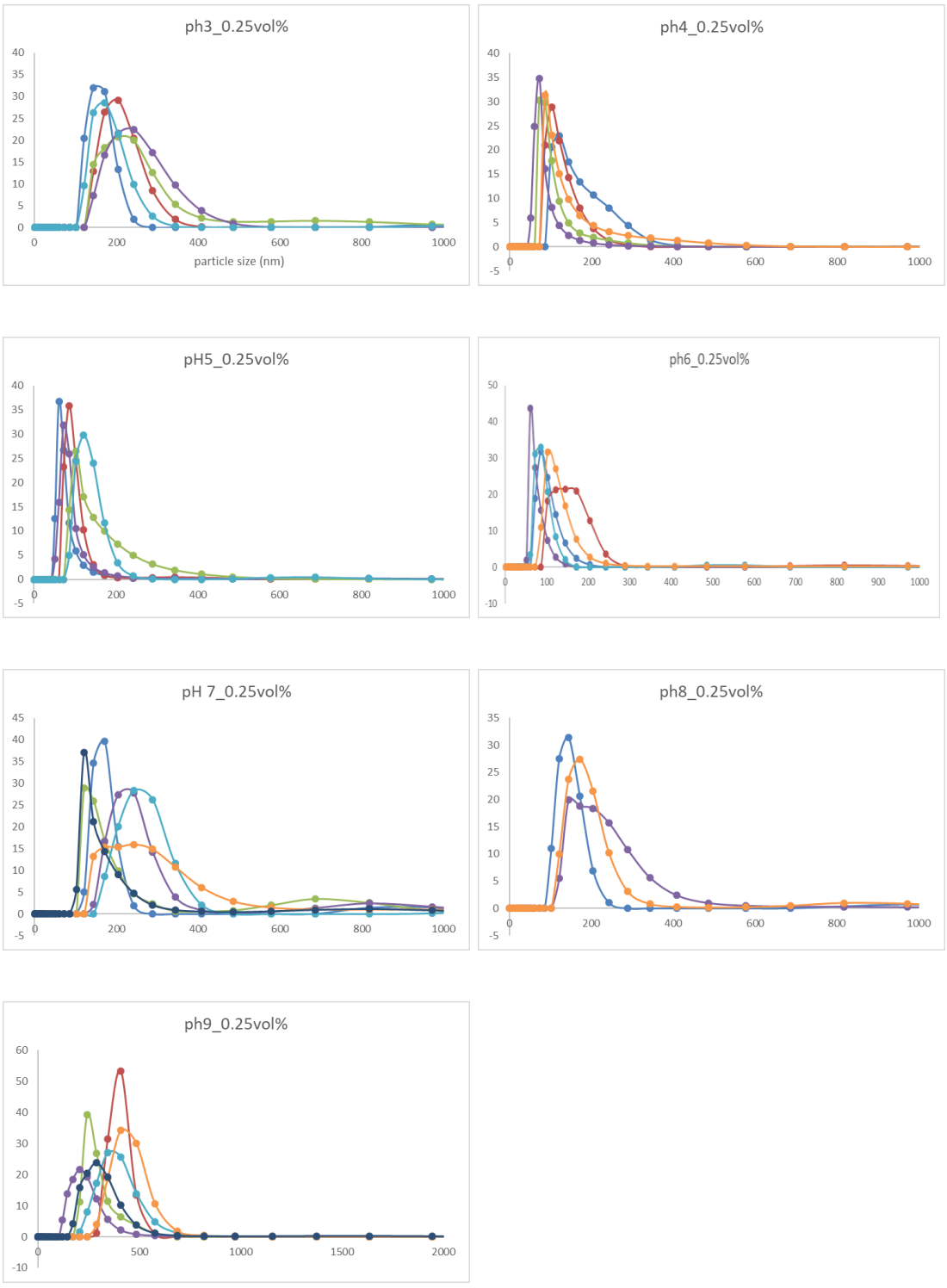

Figure 4.6 DLS results for ZnO:Ga with 0.25vol% concentration in pH3-pH9

Table 4.3 Particles size summary of ZnO:Ga suspensions (particle size: nm)

pH	3	4	5	6	7	8	9
0.125vol%	350-480	100-120	120-140	120-480	100-140	100-120	450-480
0.25vol%	140-240	80-120	60-100	85-100	170-240	150-170	350-400
1vol%	300-400	190-210	200-260	210-230	200-400	200-220	400-520

4.4 DLS and particle sizes of Sn doped In_2O_3

For In_2O_3:Sn, particle sizes are analyzed with DLS machine. Regardless of volume fractions changes, the particle size stays the same. Particles sizes are plotted below as **Figure 4.7** and specific particle numbers are summarized in **Table 4.4.** **Figure 4.7** shows the DLS plots for mesoporous In_2O_3:Sn with 0.125vol% concentration.

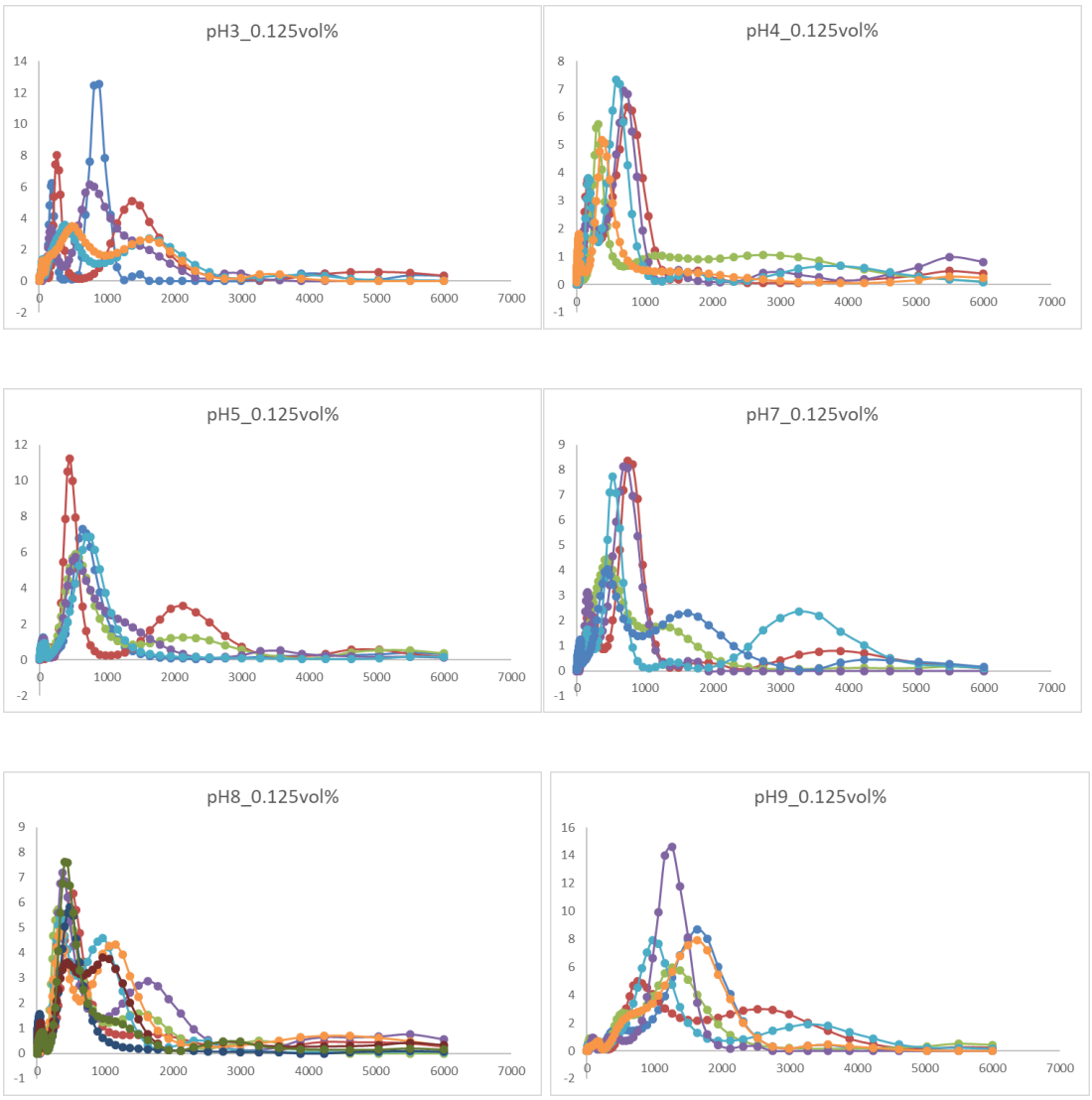

Figure 4.7 DLS results for In_2O_3:Sn with 0.125vol% concentration in pH3-pH9.

Table 4.4 Particle size summary of In_2O_3:Sn suspensions (particle sizes: nm)

	pH3	pH4	oH5	pH6	pH7	pH8	pH9
0.125vol%	290-350	340-550	580-750	450-680	500-750	970-1200	970-1300
0.25vol%	330	430	700	550	600	1100	1100

Chapter 5 Discussions

Electrical conductivities of the suspensions at powder volume fractions of 0.125 vol.%, 0.25 vol.% and 1 vol.%, were measured at seven different pH values (pH 3 to 9) and illustrated in **Figure 5.1**. The values for Ag- and Nb-doped TiO2 suspensions are shown in **Figure 5.1(a)** and **Figure 5.1(b)**, respectively, while the values for Ga-doped ZnO, and Sn-doped In2O3 are illustrated in **Figure 5.1(c)** and **Figure 5.1(d)**, respectively. **Figure 5.1(d)** illustrates the electrical conductivity of the Sn-doped In_2O_3 solutions. Differently from other materials, despite the changes in powder volume fractions, the electrical conductivities of all Sn-doped In_2O_3 suspensions almost remained constant. This can be explained by the extremely low electrical conductivity of mesoporous Sn-doped indium oxide (2.9 $(\Omega \bullet cm)^{-1}$) [299]. Due to this extremely low electrical conductivity, the electrical conductivity of Sn-doped In_2O_3 suspensions did not change much even with increased powder volume fractions (see **Figure 5.1(d)**).

Based on previous investigations, these base mesoporous materials exhibited low to high electrical conductivities with their corresponding dopants. Electrical conductivities of 2.9 $(\Omega \bullet cm)^{-1}$, 9.8 $(\Omega \bullet cm)^{-1}$, 40.0 $(\Omega \bullet cm)^{-1}$ and 300.0 $(\Omega \bullet cm)^{-1}$ were obtained for mesoporous Sn doped In_2O_3 [299, 300] Ag doped TiO_2 [301] Nb doped TiO_2 [302] and Ga doped ZnO [303]. A systematic study of these materials covering a range of electrical conductivities can give us a better insight of the correlations and mechanism of their nanofluids electrical conductivity behaviors. Most of previous research about electrical conductivities of nanofluids focused on changing powder volume fractions [304, 305, 306, 278, 288], temperatures [278, 281, 305, 307, 308] and solvents [277]. **Figure 5.2** generalized previous investigations of electrical conductivities of nanofluids when they were dispersed in aqueous solutions. Electrical conductivities of various materials including metals and ceramics were measured when they were dispersed in aqueous solutions with

different powder volume fractions. According to **Figure 5.2**, electrical conductivities are increased with increased powder volume fractions and temperatures. However, we attempt to study and explain the mechanism of nanofluids electrical conductivities with different suspension pH values and correlate the electrical conductivity of the suspensions with particle sizes change while powder volume fraction is increased. Detailed discussions are presented below.

The electrical conductivities for all four suspensions were found to be lower in acidic solutions (*i.e.*, lower pH) compared to those in basic ones (*i.e.*, higher pH). The behavior of these ceramic suspensions can be explained by considering surface charge and suspension stability. For example, when TiO_2 is dispersed in aqueous solutions, it is well known that ions (H^+, OH^-) are attached to the surface of the TiO_2 particles [309]. By changing the pH of the solutions, the surface charges are modified [310, 311, 312]. By studying the ion pair formations between the interface interaction of titanium dioxide and various cations (Cs^+, K^+, Na^+, Li^+) and anions (Cl^-, NO^{3-}, ClO^{4-}, I^-) in aqueous solutions, it has been concluded that the surface of titanium dioxide has stronger interactions with cations (acidic solutions) compared to anions (basic solutions) [313]. The weak binding between cations and the surface of titanium dioxide leaves more free ions in basic solutions compared to acidic solutions. This leads to higher electrical conductivity of TiO_2:Ag/TiO_2:Nb suspensions when dispersed in basic solutions. Our results also agree with conclusions from previous studies for titanium dioxide dispersed in pH 4 to 12 solutions [314]. Results from Tkachenko's study on titanium dioxide show an increasing trend of electrical conductivity from pH 4 to 12 with a suspension concentration of 0.03 g/L. Zeta potential increases from pH 4 to 12, which indicates better suspension stability. In addition, when titanium dioxide is dispersed in water, the net charge at the interphase of particle/solution is also controlled by pH [310, 315]. Based on the colloidal stability theory [311], the pH value of the suspension can affect the repulsive

and attractive potentials on the surface of the particle and thus affect the suspension stability. Other supporting results from Bordi *et al*. [316] also show that the electrical conductivity of silver suspension decreases with less suspension stability. In addition, when ZnO:Ga powders are dispersed in aqueous solutions, hydroxide layers are formed at the surface of the particles (≡Zn–OH). Zinc hydroxide has low solubility in water, and its solubility and stability increase with extremely high pH environments [317]. When dispersed in basic solutions, zinc oxide suspensions have better stability compared with acidic ones based on the stability research of zinc oxide suspension from Reichl [316]. Moreover, zeta-potential of indium oxide suspension increases with higher pH values [318]. Zeta potential measures the potential between the surface of the particle and the bulk solution and determines the stability of suspension, therefore its increase indicates better suspension stability. Larger electrical conductivity and better suspension stability of zinc oxide and indium oxide in basic solutions agree with our previous conclusion regarding titanium dioxide. Our results agree with Chakraborty and Padhy [319], who demonstrated the increase of electrical conductivity for stable colloidal suspensions containing nanoscale conductive particles of alumina. By investigating the agglomeration-deagglomeration effects on the electrical conductivity of α-alumina colloidal suspensions, researchers studied how the suspension stability affect the electrical conductivity. In particular, for less stable suspensions, it was concluded that small agglomeration of particles will reduce the electrophoretic mobility and dispersion of particles in the system, thus the overall electrical conductivity of the suspension is reduced. Another interesting phenomenon we have observed from Figure 3 is the different electrical conductivity behavior for different concentration with these four materials. For example, in **Figure 5.1(a)** and **5.1(b)**, electrical conductivity for 1vol.% volume fraction suspension has the highest and lowest value at pH3 and pH9 respectively. However, this phenomenon has not been

observed in other two materials. The difference between electrical conductivities at different concentrations and pH values can be associated with the effects caused by particle size change, which will be further elaborated below.

Another interesting insight is the correlation between different powder volume fraction, particle size and suspension electrical conductivity. Particle sizes at the three different powder volume fractions (0.125 vol.%, 0.25 vol.% and 1 vol.%) together with suspension electrical conductivities are plotted in **Figure 5.3**, **Figure 5.4**, and **Figure 5.5** for TiO_2:Ag, TiO_2:Nb, and ZnO:Ga, respectively. Specifically, in **Figures 5.3** and **5.4**, for pH from 3 to 5, the electrical conductivity of suspensions increases with corresponding increase in powder volume fraction. In contrast, suspension electrical conductivity decreases between 0.125 vol.% and 1 vol.% powder volume fractions with particle size increase for pH from 7 to 9. Despite this reverse relationship between particle size and electrical conductivity for pH range from 7 to 9, the particle size of TiO2:Ag/Nb shifts from decreasing to increasing with powder volume fraction increase for pH from 5 to 7. Higher powder volume fractions usually lead to larger particle sizes due to likely agglomeration of particles. However, the particle size of TiO2:Ag/Nb becomes smaller with increasing powder volume fraction (0.125 vol.% to 1 vol.%) at acidic solutions (**Figure 5.3**). Dispersion behavior of particles were investigated with alumina through electrostatic repulsion force and electric potential [320]. It was concluded that smaller particle size can be obtained when the electrostatic repulsion force between particles overcomes the attraction force. When dispersed in acidic solutions, with stronger interaction with cations compared to anions [312], the surface of TiO_2:Ag/Nb can attract more oppositely charged ions to the particle surface and augment the electrostatic repletion force. Larger electrostatic repletion force will lead to smaller particle sizes when dispersed at pH3-pH5 suspensions within powder volume fractions of 0.125vol.%-1vol.%.

In **Figure 5.5** for ZnO:Ga suspensions, decreased particle sizes and increased electrical conductivity were both observed with increased powder volume fractions. When dispersed in aqueous solutions, by increasing powder concentration of ZnO:Ga within certain range, larger electrostatic repulsion force and better dispersion of the particles are obtained. Therefore, smaller particle size was observed with increasing powder volume fraction from pH 3 to 9. Usually for ceramic or metallic suspensions, smaller particles have larger surface areas, providing higher cumulative space for attachment of various ions from suspension which immediately increases corresponding electrical conductivity of a suspension. For indium oxide, change in powder volume fraction does not affect the final suspension electrical conductivity (**Figure 5.1d**) due to the extremely low electrical conductivity of indium oxide [321].

Several previous studies show that the enhanced powder volume fractions can lead to higher electrical conductivities of the corresponding suspensions [288, 322, 323]. However, our results indicate that there is either increase or decrease of the overall electrical conductivities of ceramic suspensions with increased powder volume fractions based on different pH values. For our investigated materials, increased particle sizes correspond to decreasing electrical conductivity and decreased particle sizes result in increasing electrical conductivity. While powder volume fraction helps with the increase of electrical conductivity, the particle sizes were found to have much more pronounced effect on the resultant electrical conductivity of suspensions.

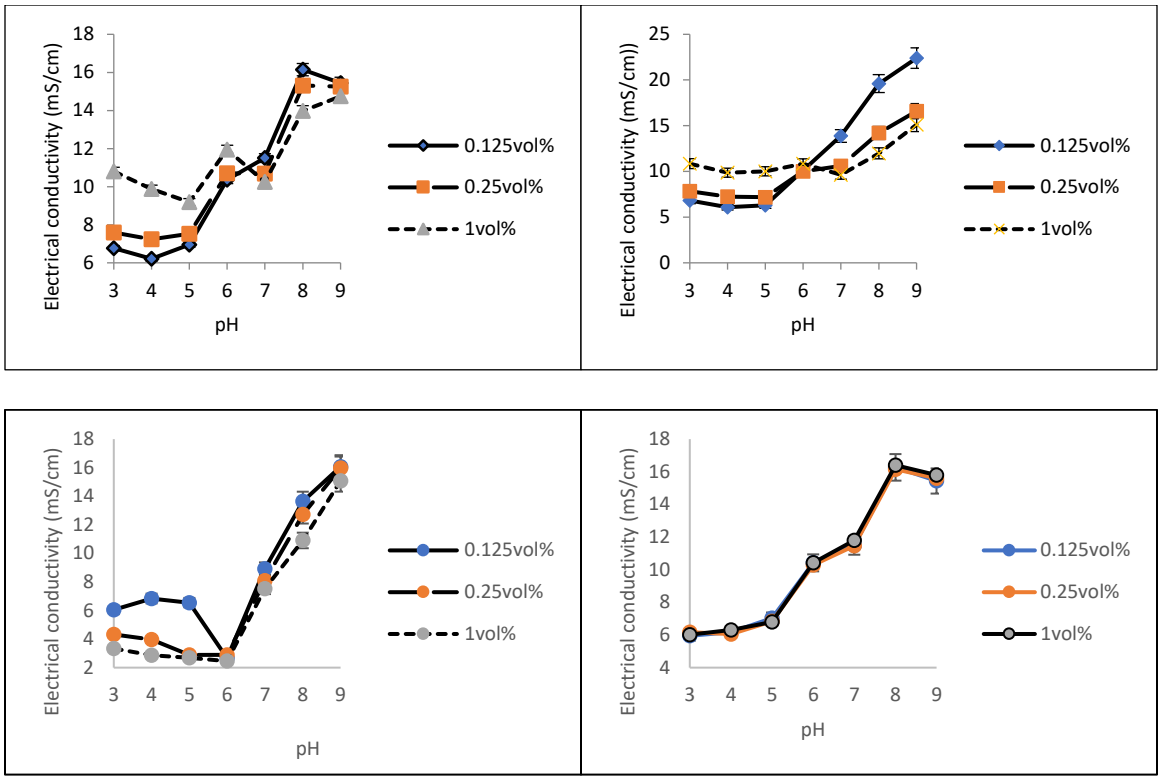

Figure 5.1 Electrical conductivities for different pH values and powder volume fractions for TiO_2:Ag (a), TiO_2:Nb (b), ZnO:Ga (c), and In_2O_3:Sn (d)

Differently from previously discussed materials, electrical conductivity of Sn doped indium oxide suspensions seems to be stable regardless powder volume fractions change (**Figure 5.1(d)**). This can be explained by the extremely low electrical conductivity of indium tin oxide [324]. Tin doping can increase the electrical conductivity of indium oxide. the ionic radius of

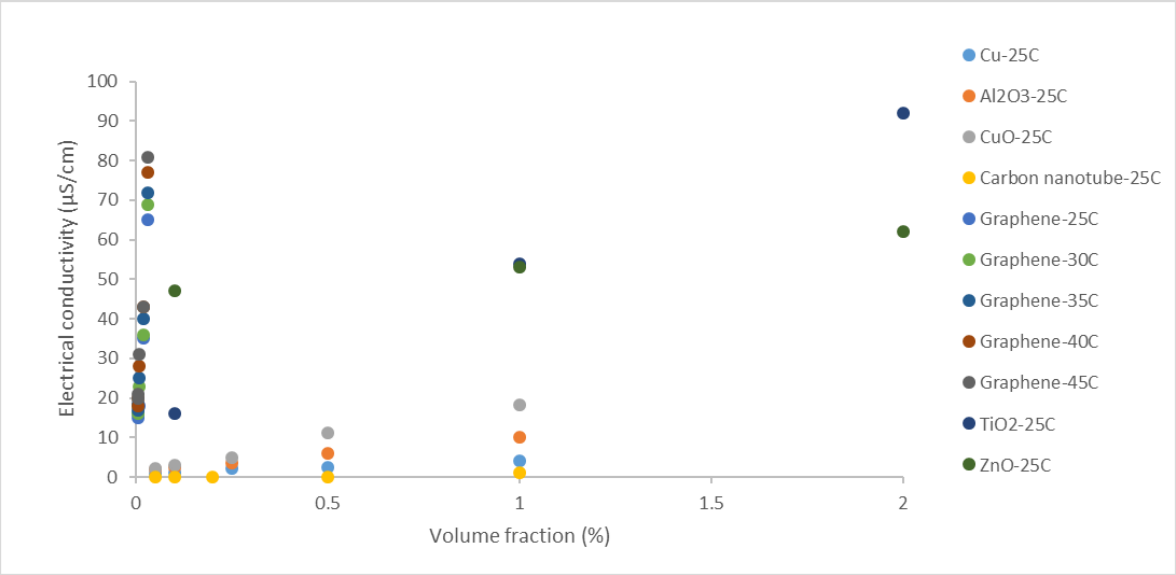

Figure 5.2 Electrical conductivities of nanofluids from previous investigations [277, 278, 281, 288, 304, 305, 306, 307, 322]

Sn^{4+} is smaller than the one of In^{3+}, therefore it substitutes indium when it is doped during the synthesis. Due to valence difference, Sn doping can provide one extra electron to the conduction band. This one extra electron provides more carrier concentration and improves the electrical conductivity. Even with this improved electrical conductivity for In_2O_3:Sn, it is still much smaller compared with the previously described materials. This extremely low electrical conductivity may explain the unchanged electrical conductivity of the dilute suspensions for all the three volume fractions examined (see **Figure 5.1(d)**). Also, because of this characteristic of indium tin oxide we decided not to include this material into our further discussion regarding the influence of particle sizes on the electrical conductivity.

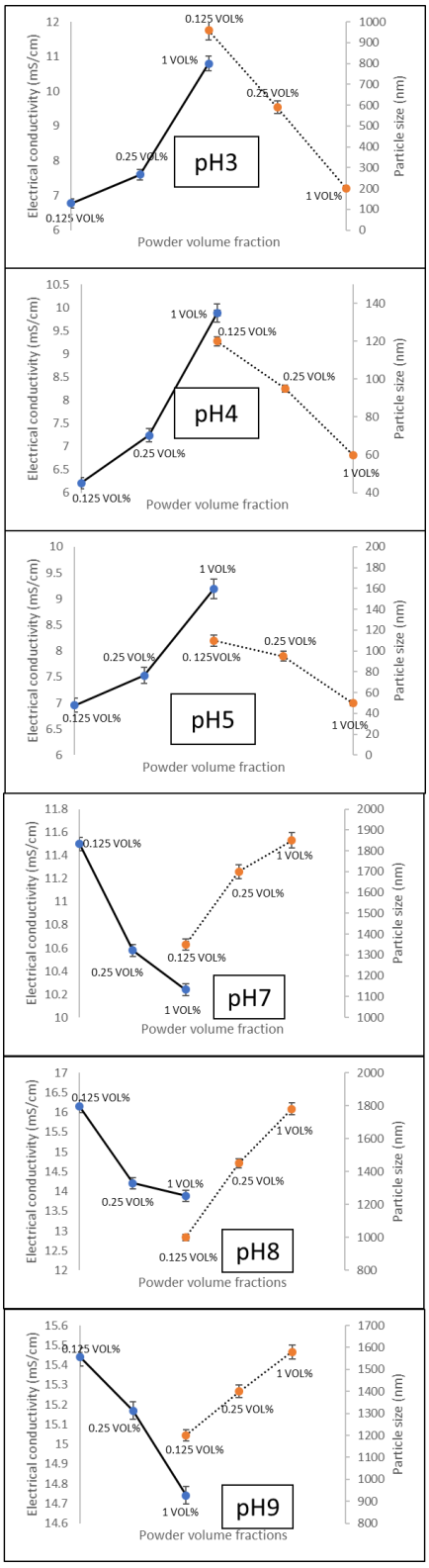

Figure 5.3 Electrical conductivity and particle sizes of TiO_2:Ag from pH3-pH9 with 0.125 vol.%, 0.25 vol.% and 1 vol.%

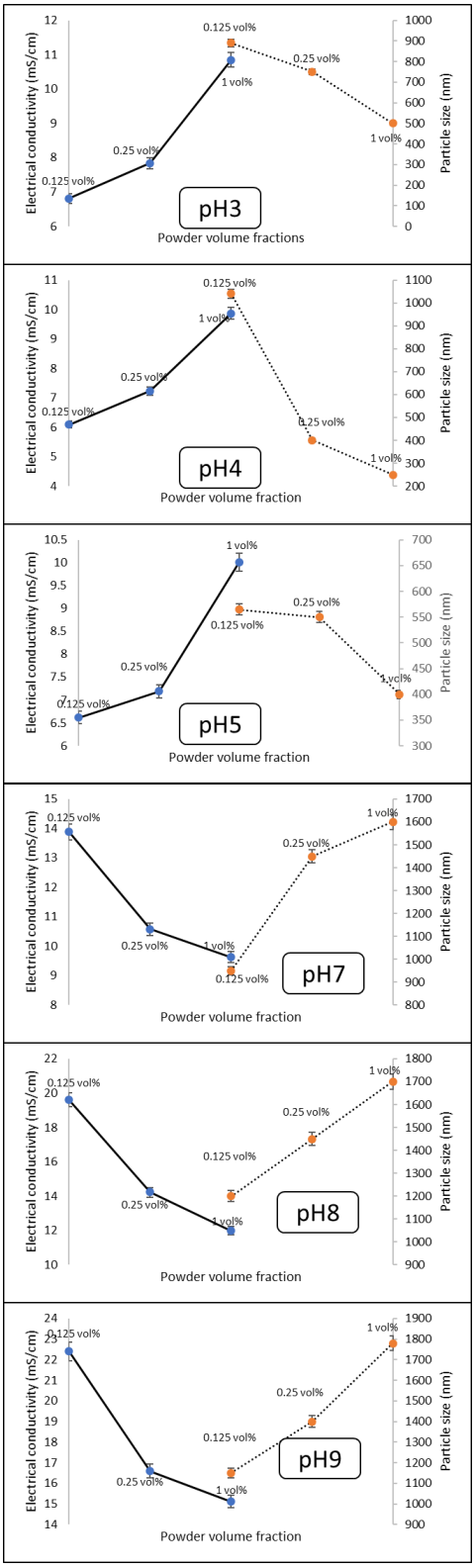

Figure 5.4 Electrical conductivity and particle sizes of TiO_2:Nb from pH3-pH9 with 0.125 vol.%, 0.25 vol.% and 1 vol.%

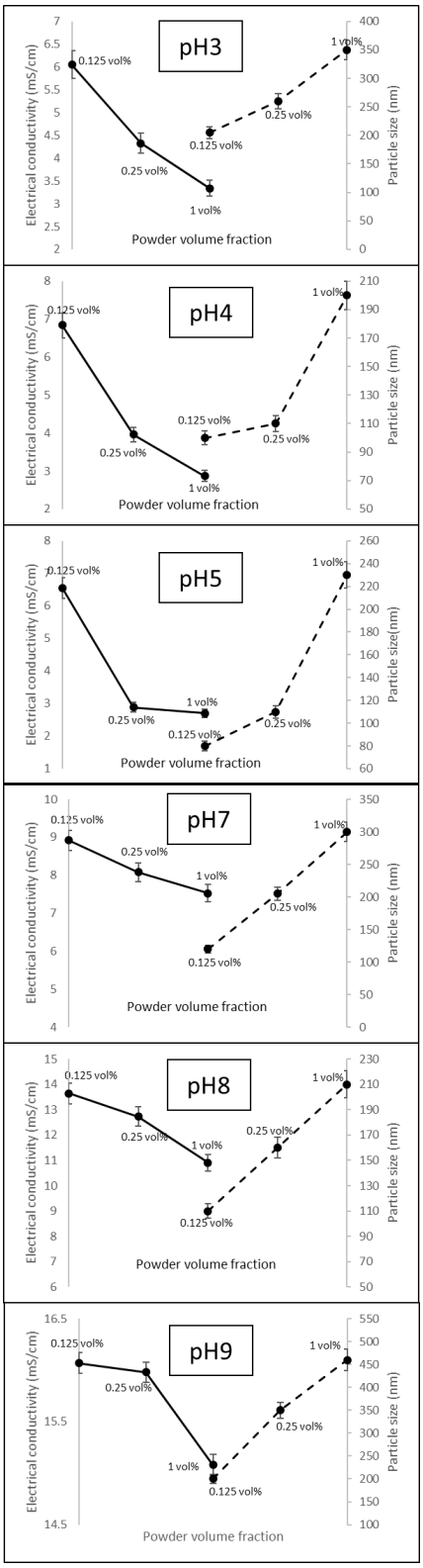

Figure 5.5 Electrical conductivity and particle sizes of ZnO:Ga from pH3-pH9 with 0.125 vol.%, 0.25 vol.% and 1 vol.%

In summary, electrical conductivity of measured suspensions is higher in basic solutions compared with acidic solutions. In addition, for acidic solutions of Ag/Nb doped titanium dioxide, particle size and electrical conductivity are observed to be decreasing and increasing with powder volume fraction increase. However, for basic solutions, particle size and electrical conductivity are observed to be increasing and decreasing. For Ga doped zinc oxide, with increased powder volume fractions, particle size and electrical conductivity are observed to be decreasing and increasing both in basic and acidic solutions. Finally, there is no noticeable change of electrical conductivity of indium tin oxide with powder volume fraction changes.

Chapter 5, in full, is currently being prepared for submission for publication of the material. Shuang Qiao, Ekaterina Novitskaya, Flor Sanchez, Manuel Herrera Zaldivar, Rafael Vazquez-Duhalt, and Olivia A. Graeve. The dissertation author was the primary investigator and author of this material.

Chapter 6 Theoretical model

Nomenclature

σ_p	electrical conductivity of particles	$mS \bullet cm^{-1}$
σ	electrical conductivity	$mS \bullet cm^{-1}$
σ_o	electrical conductivity of pure buffer solution	$mS \bullet cm^{-1}$
α	ratio of electrical conductivity of particle to the electrical conductivity of pure buffer solution	
φ	powder volume fraction	
σ_M	electrical conductivities from the Maxwell model	$mS \bullet cm^{-1}$
σ_B	electrical conductivities from the Brownian motion	$mS \bullet cm^{-1}$
σ_E	electrical conductivities from electrophoresis	$mS \bullet cm^{-1}$
n	the number of particles in per unit volume	
η	the dynamic viscosity of the liquid	$m^2 \bullet s^{-1}$
ε_o	dielectric constant of the vacuum	$F \bullet m^{-1}$
ε_r	relatively dielectric constant of the base fluid	
ρ	density of base fluid	$g \bullet cm^{-3}$
υ	kinetic viscosity of the base fluid	$m^2 \bullet s^{-1}$
A_0	Avogadro's number	mol^{-1}
R	gas constant	$J \bullet mol^{-1} \bullet K^{-1}$
λ	viscosity index of the fluid	
r	radius of particle	m

ζ_o	zeta potential	V
I	ionic strength	mol•kg^{-1}
Ψ_o	surface potential	V
b	slip length	m

A comprehensive model to explain the mechanism of electrical conductivity of suspensions with respect to corresponding powder volume fractions, particle sizes and solution pH was proposed.

The effect of powder volume fraction on electrical conductivity of suspensions was first evaluated by Maxwell [275]. This model describes the final electrical conductivity of the mixture by separately considering the conductivities of continuous liquid and dispersed particles. The results of the model can be expressed as **Equation 6.1**:

$$\sigma_{Maxwell} = \sigma_0(1 + \frac{3(\alpha-1)\varphi}{(\alpha+2)-(\alpha-1)\varphi}) \quad (6.1)$$

where $\sigma_{Maxwell}$ is the electrical conductivity of suspension, σ_0 represents the electrical conductivity of the base fluid, α represents the ratio between the conductivities of particle and base fluid, and Φ is the powder volume fraction. Calculations from Maxwell model together with the experimental results on dependence of electrical conductivity on powder volume fraction from the current study are plotted on **Figures 6.1-Figure 6.4**. The general trend obtained from Maxwell model is consistent with our experimental results for all four materials, however the predictions from Maxwell model were found to be smaller compared to the experimental measurements. It is believed that Maxwell model does not consider the electrical conductivity enhancement contributed from particle-fluid interaction as well as particle size effect [276, 280].

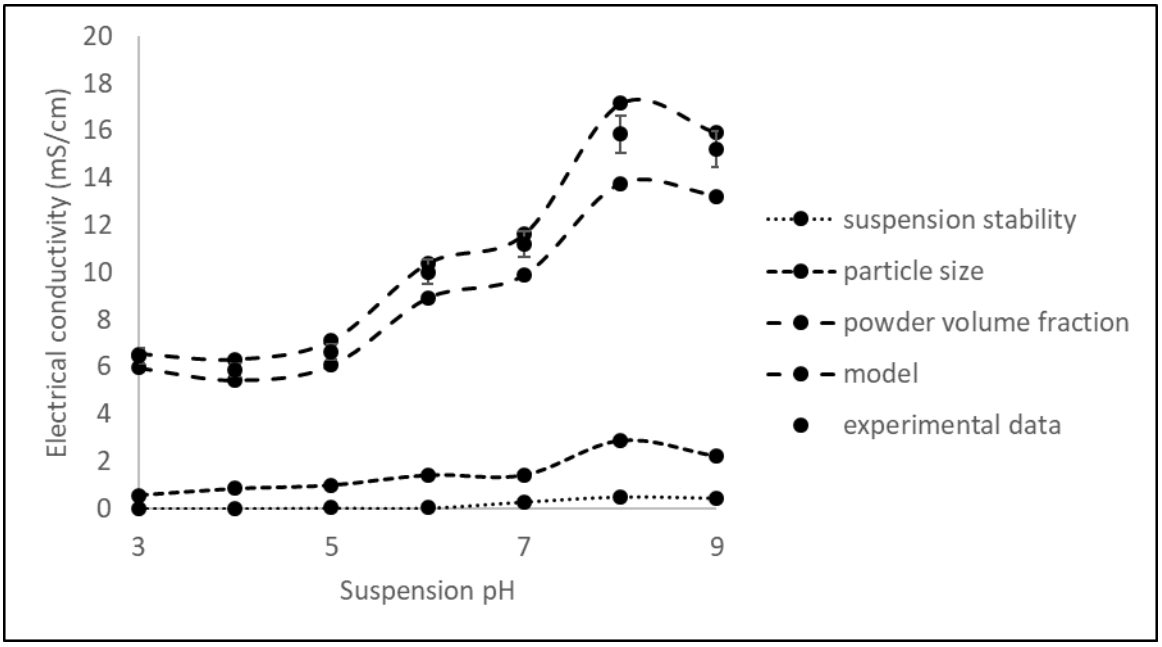

Figure 6.1 Experimental results for electrical conductivity of ceramic suspensions with 0.125 vol% of powders for pH3-pH9 vs modeling data for TiO_2:Ag

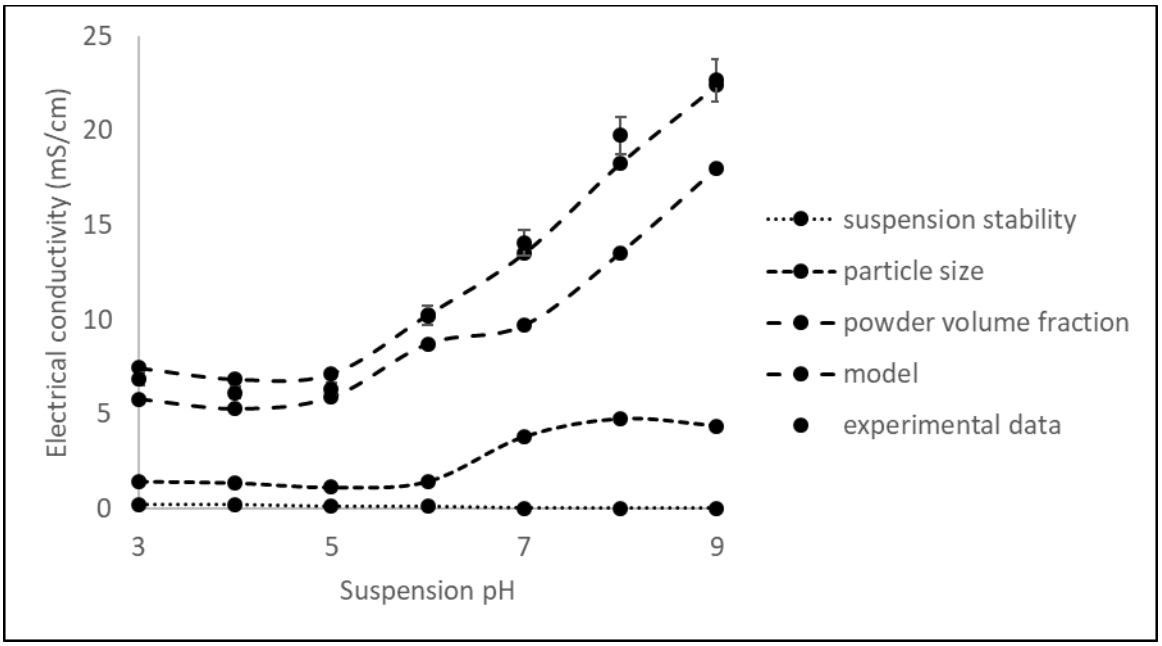

Figure 6.2 Experimental results for electrical conductivity of ceramic suspensions with 0.125 vol% of powders for pH3-pH9 vs modeling data for TiO_2:Nb

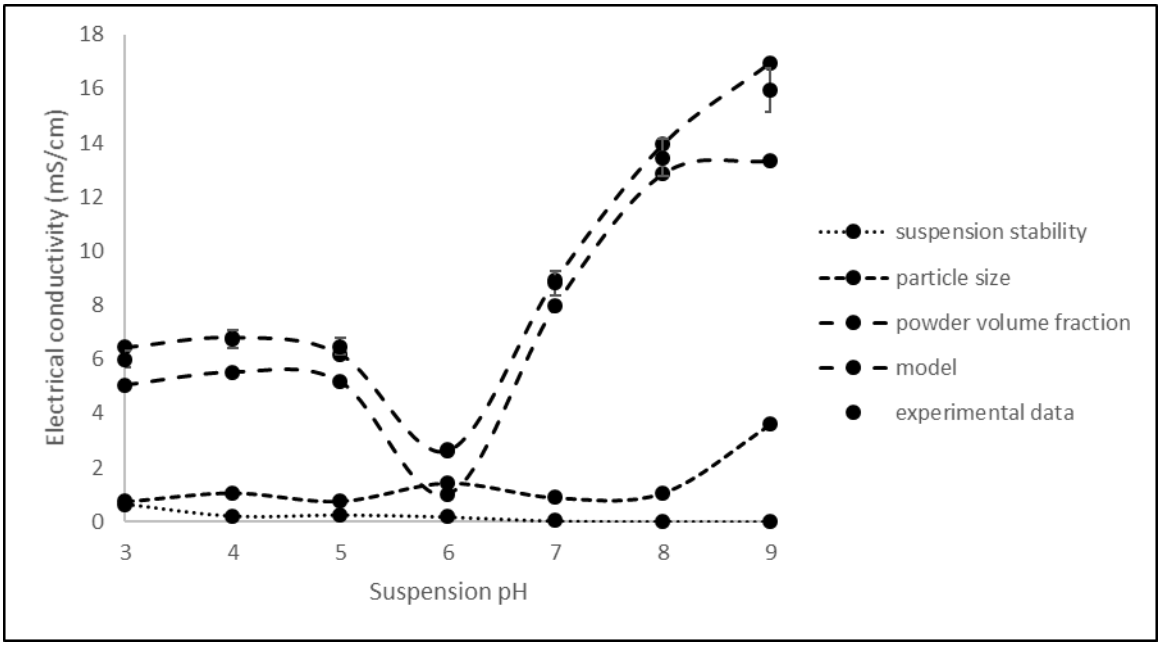

Figure 6.3 Experimental results for electrical conductivity of ceramic suspensions with 0.125 vol% of powders for pH3-pH9 vs modeling data for ZnO:Ga

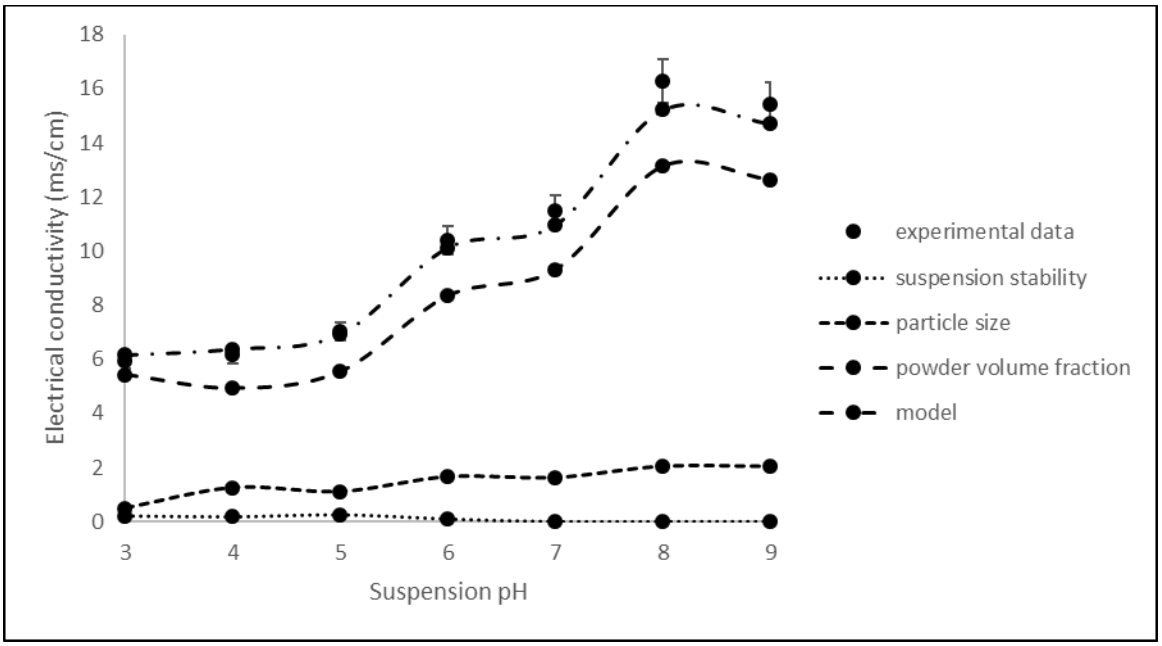

Figure 6.4 Experimental results for electrical conductivity of ceramic suspensions with 0.125 vol% of powders for pH3-pH9 vs modeling data for In_2O_3:Sn

To consider these effects, a net charge formed at the surface of the particles for uniformly dispersed solutions was proposed by [276]. This net charge will affect the distribution of ions on the surface of the particles. The corresponding electrical conductivity of the solution will depend on particle size (which will define the number and density of ions that are attached to the surface of particle). Additional step proposed by Shen includes a consideration of static and dynamic electrical conductivities of nanofluids; the predicted outcomes were verified on zinc oxide particles dispersed in insulated oil. Since the liquid system used in this study was only limited to insulated oil, it did not consider the influence from the suspension stability and pH change of the system. Therefore, these results cannot completely explain our case of ceramic suspensions in water solutions with different pH values. As a result, a theoretical model of electrical conductivity of nanofluids which considers the effects of suspension pH was proposed in the current study.

We will be using the equation of Maxwell model (**Equation 6.1**) as the electrical conductivity of powder volume fraction effect ($\sigma_{powder\ volume\ fraction}$). We assume spherical particles with a uniform radius of *r*. When particles are dispersed in solution, there will be positively and negatively charged ions attached to the surface of each particle; these ions have non-zero net electrical charge and electrons [325]. The relationship between electrical conductivity of the particle and electron mobility can be expressed by **Equation 6.2**:

$$\sigma = \mu * q \tag{6.2}$$

where σ is the electroconductivity of particles, q is electron charge, and μ is electron mobility. Based on Walden rule, which states that the product of the viscosity and the ionic conductance in dilute electrolytic solutions remains constant [326], the electron mobility can be calculated as:

$$\mu = \frac{q}{6\pi r \eta} \tag{6.3}$$

where η is the dynamic viscosity of the liquid, and r is a radius of the particle.

Summarizing **Equations 6.2 and 6.3**:

$$\sigma = \frac{q^2}{6\pi r\eta} \tag{6.4}$$

Based on Coulomb's law, the cumulative charge at the surface of the particle can be expressed by:

$$q = 4\pi\varepsilon_r\varepsilon_0 r U_0 \tag{6.5}$$

where ε_0 is the dielectric constant of the vacuum, ε_r is the relatively dielectric constant of the base fluid, and U_0 represents the zeta potential of the nanofluid.

By substituting **Equation 6.5** into **Equation 6.4**, the impact from the ions attached to the surface of one spherical particle on electrical conductivity of suspension can be expressed as:

$$\sigma = \frac{8\pi r n_0 \varepsilon_r^2 \varepsilon_0^2 U_0^2}{3\eta} \tag{6.6}$$

The number of electrons per volume can be calculated by dividing powder volume fraction on the volume of one particle:

$$n_0 = \frac{\phi}{V} = \frac{3\phi}{4r^3\pi} \tag{6.7}$$

Summarizing all above, the electrical conductivity of nanofluid considering particle sizes effects can be expressed by:

$$\sigma_{particle\ size} = \frac{2\phi\varepsilon_r^2\varepsilon_0^2 U_0^2}{\eta r^2} \tag{6.8}$$

Both, radius of the particles and the zeta potential of nanofluid can be obtained from DLS characterization.

In addition, pH of solution will influence the suspension stability by affecting both the aggregation of particles, and concentration of ions on the surface of particles. The stability of solution is reflected by the value of zeta potential. Zeta potential measures the potential between the surface of the particle and bulk solution. Furthermore, the thin layer in between of particle and

corresponding fluid is termed as electrical double layer (EDL); the thickness of this layer is defined by Debye length ($1/\kappa$) [327] and can be expressed by:

$$\kappa = (32.87*10^{8}\sqrt{I})m^{-1} \quad (6.9)$$

where I is the concentration of ions in the solution and κ is Debye screening wave vector.

According to [328], the relationship between ion concentration and electroconductivity of the solution is shown by:

$$I = 0.013*\sigma \quad (6.10)$$

A combination of **Equations 6.9** and **6.19** will produce an expression for electrical conductivity of suspensions considering its pH values:

$$\sigma = \frac{\kappa^2}{32.4*10^{16}} \quad (6.11)$$

The Debye length can be calculated based on the zeta potential of the system according to [329]:

$$U_0 = \Psi_0(1 + b\kappa) \quad (6.12)$$

where Ψ_0 is the electrostatic surface potential and b is a slip-induced amplification factor [330]. By substituting **Equation 13** into **Equation 12**, the electrical conductivity of suspension considering its stability is expressed as:

$$\sigma_{suspension\ stability} = \frac{(U_0-\Psi_0)^2}{b^2{\Psi_0}^2*3.24*10^{17}} \quad (6.13)$$

Eventually, by combining the effects of powder volume fraction (see **Eq. 6.1**), particle sizes effect (see **Eq. 6.8**), and suspension stability effect (see **Eq. 6.13**), the final equation for electrical conductivity of dilute suspension was obtained:

$$\sigma_{electrical\ conductivity} = \sigma_{powder\ volume\ fraction} + \sigma_{particle\ size} + \sigma_{suspension\ stability} = \sigma_0\left(1 + \frac{3(\alpha-1)\varphi}{(\alpha+2)-(\alpha-1)\varphi}\right) + \frac{2\varphi\varepsilon_r^2\varepsilon_0^2U_0^2}{\eta r^2} + \frac{(U_0-\Psi_0)^2}{b^2{\Psi_0}^2*3.24*10^{17}} \quad (6.14)$$

Calculated values based on **Equation 6.14** were plotted and compared with our experimental results for electrical conductivities of all four materials from the current study (see **Figures 6.1-Figure 6.4**). All four materials are examined with 0.125 vol.% powder volume fraction since this is the most dilute suspension we obtained in the experiments and both Maxwell and Shen's models are only applied to dilute suspensions. As seen on **Figure 6.1** for TiO_2:Ag suspension, there is no linear relationship between electrical conductivity of suspension and powder volume fraction or particle sizes. It also appears that particle sizes have more pronounced effect on the corresponding electrical conductivities of suspension than powder volume fractions (see above discussions). The disagreement between Maxwell model and experimental data has also been observed by other researchers [276, 278]. Shen's model considers the effect of particle sizes on the suspension stability, however calculation from his model was also smaller than our experimental results (see **Figure 6.1-Figure 6.4**). After incorporating the third part (suspension stability effect) into our revised model, we obtain a good match with the experimental results. **Figure 6.2-Figure 6.4** display the electrical conductivity curves of TiO_2:Nb, ZnO:Ga and In_2O_3:Sn with their experimental data and results from all three models. Overall, the experimental results are in a good agreement with theoretical predictions based on the proposed comprehensive model for dilute suspensions with powder volume fraction of 0.125 vol.%.

The ultimate objective of the current project is to predict the electrical conductivity of suspensions prepared with different types of base fluids. According to our revised model, the final electrical conductivity of suspension is a function of powder volume fraction, particle size and suspension stability (see **Equation 6.14**). The excessive effects from various parameters (such as particle size, zeta potential, dynamic viscosity of fluid *etc*.) is one of the main obstacles to accurately predict the electrical conductivity of nanofluids; the proposed model quantifies

these aspects by comprehensive mathematical approach. Based on the proposed model, we generate an equation to predict the electrical conductivity of a ceramic suspension with different base fluids. Four curves for TiO_2:Ag, TiO_2:Nb, ZnO:Ga and In_2O_3:Sn suspensions are given in **Figure 6.5-6.8**; electrical conductivities of suspensions are plotted vs. electrical conductivities of base fluid. As seen on **Figure 6.5**, similar behavior was noticed for all four materials: Almost linear relationship between electrical conductivity of base fluid and electrical conductivity of the corresponding suspension was obtained. An excellent correlation between electrical conductivity curves (dash lines in **Figure 6.5**) and experimental data (solid dots in **Figure 6.5**) provide the opportunity to accurately predict the electrical conductivity of any ceramic nanofluids.

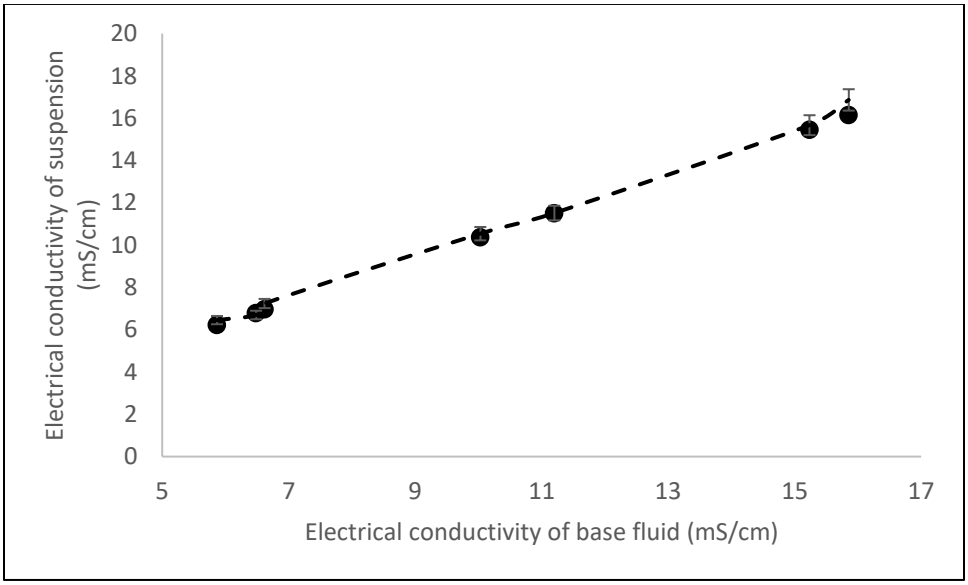

Figure 6.5 Electrical conductivity of TiO_2:Ag suspensions with respect to electrical conductivity of base fluid vs modeling results

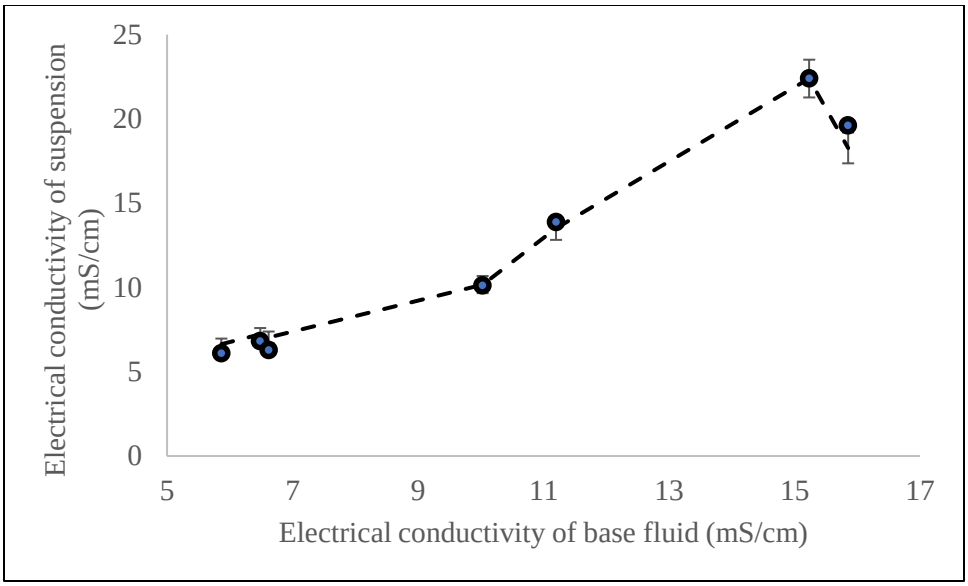

Figure 6.6 Electrical conductivity of TiO_2:Nb suspensions with respect to electrical conductivity of base fluid vs modeling results

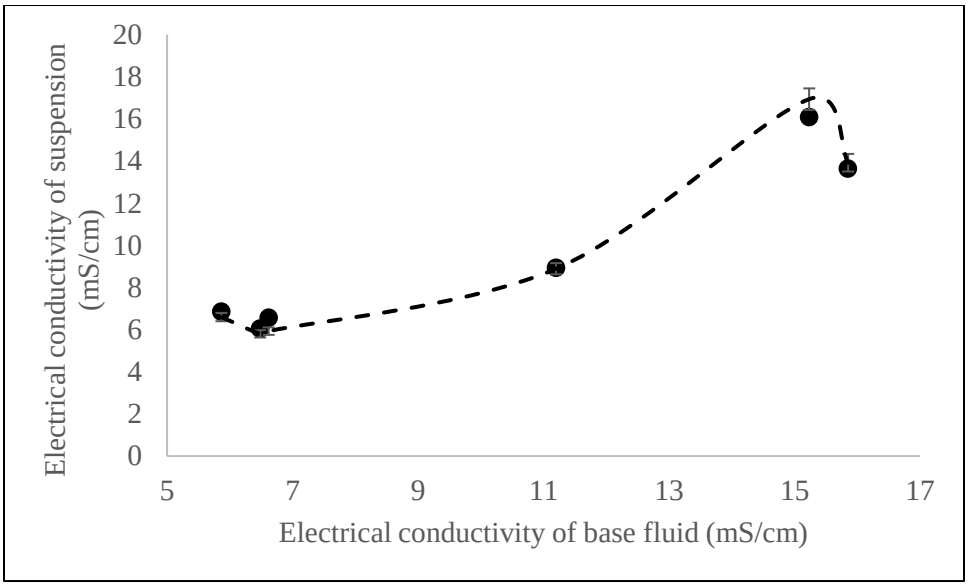

Figure 6.7 Electrical conductivity of ZnO:Ga suspensions with respect to electrical conductivity of base fluid vs modeling results

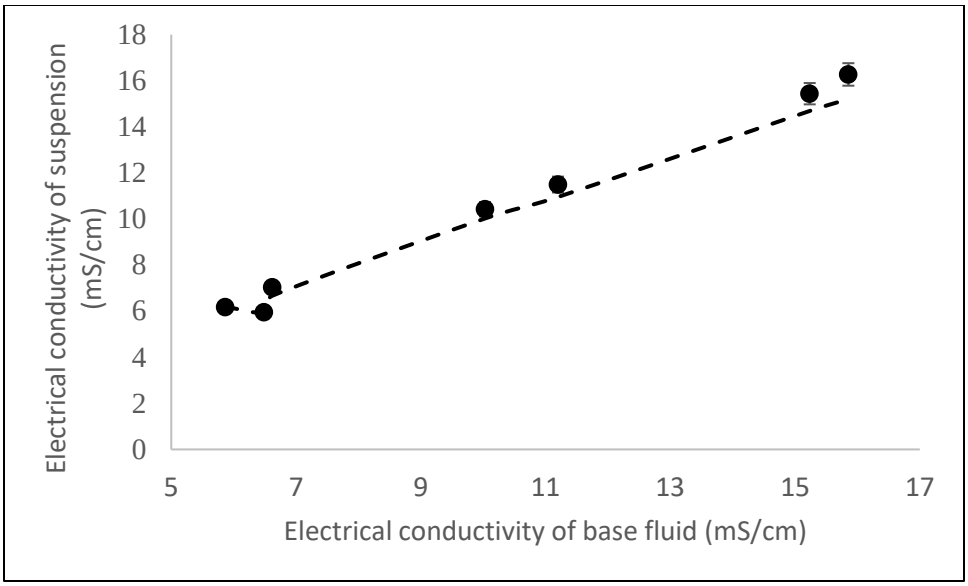

Figure 6.8 Electrical conductivity of In_2O_3:Sn suspensions with respect to electrical conductivity of base fluid vs modeling results

Results obtained from our revised model was compared with Maxwell model in **Figure 6.9-Figure 6.12**. The general trend obtained from the Maxwell model is consistent with our experimental results for all four materials, however the predictions from Maxwell model were found to be much smaller compared to the experimental measurements. It is believed that Maxwell model only considers the effect from powder volume fractions. In our revised model, we thoroughly consider the suspension stability effect together with powder volume fraction and particle sizes. The stability of solution is reflected by the value of zeta potential which is measured by DLS machine.

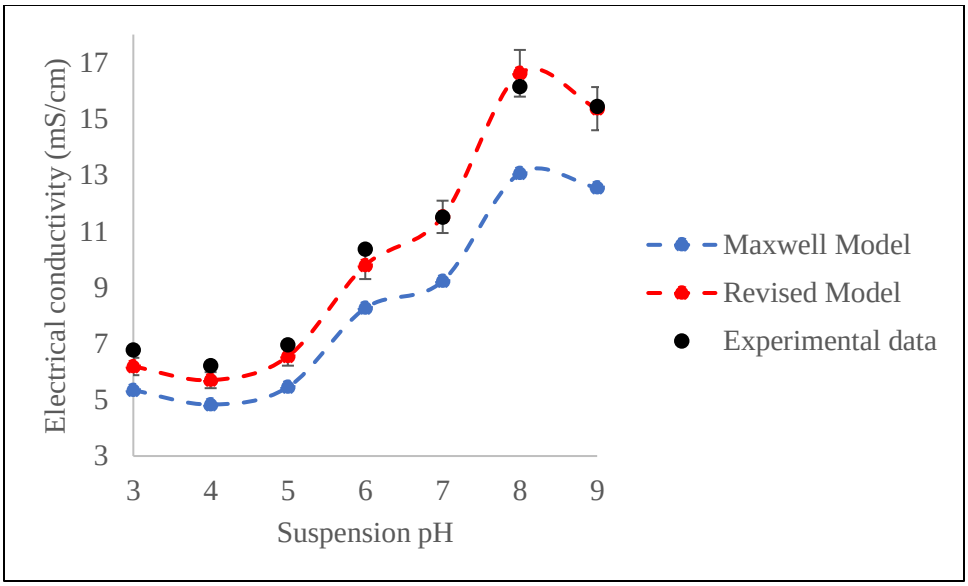

Figure 6.9 Experimental data points (black dots) and revised model results (red dash curves) vs. Maxwell model (blue dash curves) for electrical conductivity of ceramic suspensions for TiO_2:Ag

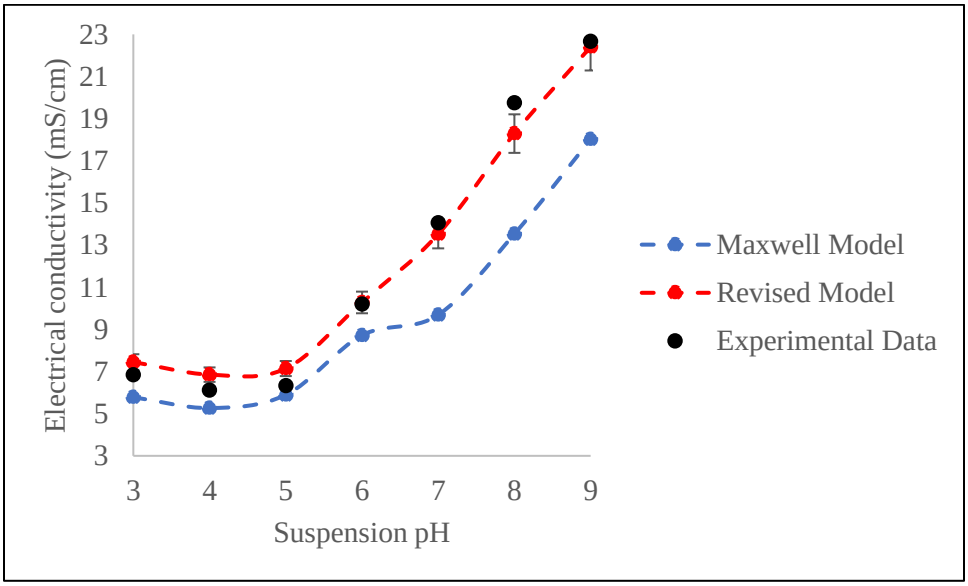

Figure 6.10 Experimental data points (black dots) and revised model results (red dash curves) vs. Maxwell model (blue dash curves) for electrical conductivity of ceramic suspensions for TiO_2:Nb

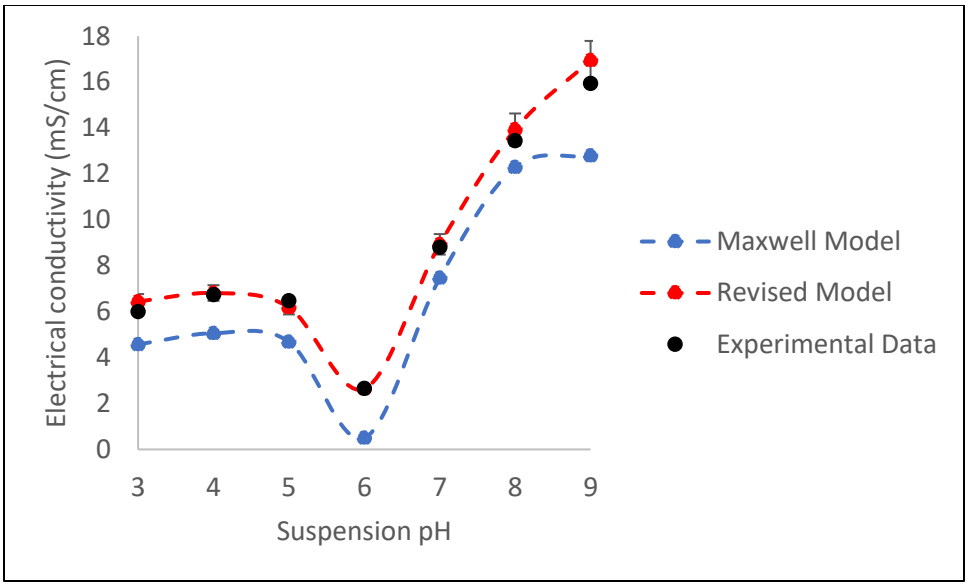

Figure 6.11 Experimental data points (black dots) and revised model results (red dash curves) vs. Maxwell model (blue dash curves) for electrical conductivity of ceramic suspensions for ZnO:Ga

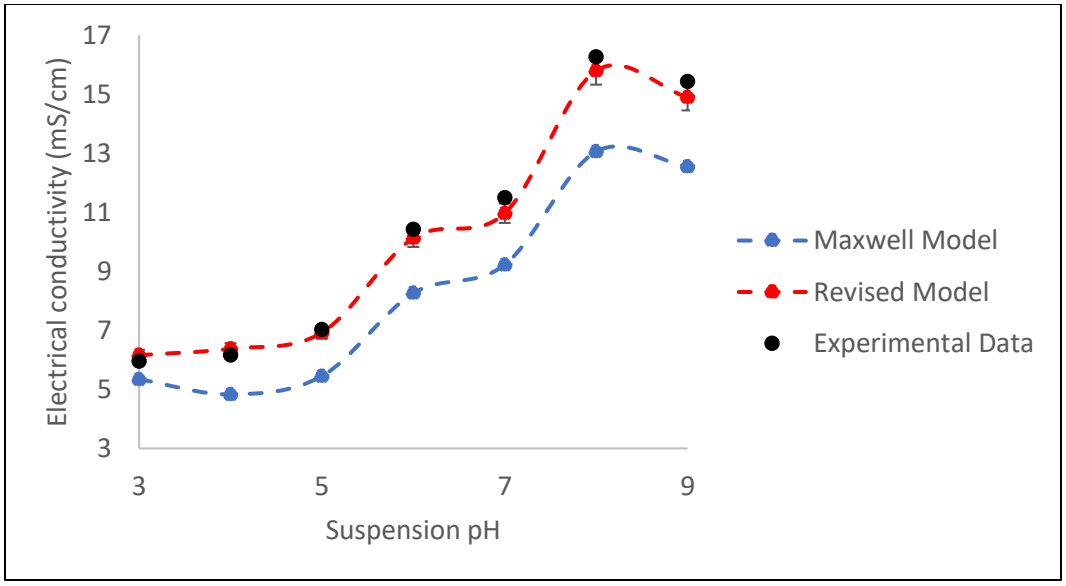

Figure 6.12 Experimental data points (black dots) and revised model results (red dash curves) vs. Maxwell model (blue dash curves) for electrical conductivity of ceramic suspensions for In_2O_3:Sn

Further look at **Figure 6.1** reveals another unique behavior for ZnO:Ga suspensions: there seems to be a dip for the electrical conductivity at pH6. This indicates that zinc oxide has the smallest electrical conductivity at around pH6 (pH5-pH7). pH is an important parameter for controlling the stability of suspension by affecting the particle interactions [331]. It was usually found that pure zinc oxide nanoparticles have zero zeta potential (isoelectric point) between pH8-pH10.3 [332, 333, 334]. Further research indicates that the isoelectric point (least suspension stability) can greatly be decreased to pH6 by adding impurities, coating, or by changing the suspension pH values [333]. These modifications can change the surface charge of zinc oxide and further affect its isoelectric point. In our case, by doping zinc oxide with Ga and uniformly disperse these nanoparticles in suspension with different pH values (pH3-9), the isoelectric point of zinc oxide is also modified. ZnO:Ga suspension at pH6 is least stable and thus has the smallest electrical conductivity compare to other pH values.

In summary, a theoretical model describing electrical conductivity of ceramic suspensions considering effects of powder volume fraction, particles size and suspension stability was proposed in this study. An excellent correlation between modelling predictions and experimental results was verified for four different ceramic-based suspensions: Ag/Nb doped titanium dioxide, Ga doped zinc oxide, and Sn doped indium oxide.

Chapter 6, in full, is currently being prepared for submission for publication of the material. Shuang Qiao, Ekaterina Novitskaya, Flor Sanchez, Manuel Herrera Zaldivar, Rafael Vazquez-Duhalt, and Olivia A. Graeve. The dissertation author was the primary investigator and author of this material.

Chapter 7. Conclusions

In this research project, we first synthesized four different kinds of mesoporous materials: Ag and Nb doped TiO_2, Ga doped ZnO and Sn doped In_2O_3 with wet-chemical method. Powders were all characterized by XRD, TEM, and BET to confirm their crystal structure, morphology and pore sizes, respectively. Synthesized mesoporous powders were later uniformly dispersed into pH3-pH9 buffer solutions with different powder volume fractions through magnetic stirring and ultrasonication. Electrical conductivity of the nanofluids were measured and particle sizes were analyzed by DLS technique. Then we propose a revised model to predict the electrical conductivity of diluted ceramic suspensions with these four materials. Based on the experimental data obtained for the electrical conductivities of these four (Ag/Nb doped TiO_2, Ga doped ZnO, and Sn doped In_2O_3) nanofluids, we generate a mathematical equation that incorporates three main parameters affecting electrical conductivity of ceramic suspensions: powder volume fraction, particle sizes and suspension stability. An equation as a function of powder volume fraction φ, electrical conductivity of base fluid σ_0, dynamic viscosity of suspension η, zeta potential ζ, dielectric constant of solution ε_r and electrostatic surface potential Ψ_0 was discussed and explained in detail regarding the derivative and calculations. Specific derivations of each step are also shown in the paper. The model has been confirmed successful with excellent correlation between the results obtained from the modelling and experimental data. Our current proposed model quantifies all the aspects that will contribute to the electrical conductivity of nanofluids by comprehensive mathematical approach. Besides, the mechanisms of electrical conductivity of nanofluids were also investigated. Particle size and electrical conductivity of the suspension shows reverse relationship at the same pH value with concentration increases for all our examined materials. It is concluded that the particle sizes have more pronounced effect on the electrical conductivities of

corresponding suspensions compared to powders' volume fractions. In addition, all four ceramic suspensions tested in our study show higher electrical conductivity in basic solutions compared to the acidic ones due to better suspensions stability in basic environment.

Chapter 7, in part, is currently being prepared for submission for publication of the material. Shuang Qiao, Ekaterina Novitskaya, Flor Sanchez, Manuel Herrera Zaldivar, Rafael Vazquez-Duhalt, and Olivia A. Graeve. The dissertation author was the primary investigator and author of this material.

Chapter 8 Recommendations for future work

Based on current progress, the following recommendations are suggested for future work to help further address some issues related to electrical conductivity of mesoporous suspensions as well as the electrical conductivity model we have developed:

- Further study the pore size influences on the final electrical conductivity of stable mesoporous ceramic suspensions. The current synthesized mesoporous materials have the pore sizes between 7-10 nm. We can vary the pore sizes by changing the synthesis conditions and investigate the influences on final suspension electrical conductivity caused by the pore size change.
- Expand the investigated materials to metals as well as carbon nanotubes. In our current study, all four involved materials are ceramics (Ag/Nb doped TiO_2, Ga doped ZnO and Sn doped In_2O_3), we can further expand the study to metals and carbons even graphene to get a more systematic study of electrical conductivities of mesoporous suspensions.
- Include the temperature influences on our developed electrical conductivity model. All the experiments are conducted at room temperatures and our current model does not include the impact of temperature changes. In the future work, temperatures influences should also be investigated and considered as one important parameter in the model.

References

1. K. S. W. Sing, D. H. Everett, R. A. W. Haul, L. Moscou, R. A. Pierotti, J. Rouquérol and T. Siemieniewska, Reporting physisorption data for gas/solid systems with special reference to the determination of surface area and porosity, *Pure Appl. Chem.*, 1985, **57**, 603-619.

2. C. T. Kresge, M. E. Leonowicz, W. J. Roth, J. C. Vartuli and J. S. Beck, Ordered mesoporous molecular sieves synthesized by a liquid-crystal template mechanism, *Nature*, 1992, **359**, 710–712.

3. S. S. Kim, W. Zhang and T. J. Pinnavaia, Ultrastable mesostructured silica vesicles, *Science*, 1998, **282**, 1302–1305.

4. P. T. Tanev and T. J. Pinnavaia, Biomimetic templating of porous lamellar silicas by vesicular surfactant assemblies, *Science*, 1996, **271**, 1267–1269.

5. L. Mercier and T. J. Pinnavaia, Direct synthesis of hybrid organic−inorganic nanoporous silica by a neutral amine assembly route: structure−function control by stoichiometric incorporation of organosiloxane molecules, *Chem Mater.*, 2000, **12**, 188–196.

6. S. Oliver, A. Kuperman, N. Coombs, A Lough and GA Ozin, Lamellar aluminophosphates with surface patterns that mimic diatom and radiolarian microskeletons, *Nature*, 1995 **378**, 47–50.

7. Q. Huo, DI Margolese and GD Stucky, Surfactant Control of Phases in the Synthesis of Mesoporous Silica-Based Materials, *Chem Mater*., 1996, **8**, 1147–1160.

8. J. S. Beck, J. C. Vartuli, W. J. Roth, M. E. Leonowicz, C. T. Kresge and K. D. Schmitt, A new family of mesoporous molecular sieves prepared with liquid crystal templates, *J Am Chem Soc.*, 1992, **114**, 10834–10843.

9. A. Monnier, F. Schüth, Q. Huo, D. Kumar, D. Margolese and R. S. Maxwell, Cooperative formation of inorganic-organic interfaces in the synthesis of silicate mesostructures, *Science*, 1993, **261**, 1299–1303.

10. J. C. Vartuli, K. D. Schmitt, C. T. Kresge, W. J. Roth, M. E. Leonowicz and S. B. McCullen, Effect of Surfactant/Silica Molar Ratios on the Formation of Mesoporous Molecular Sieves: Inorganic Mimicry of Surfactant Liquid-Crystal Phases and Mechanistic Implications, *Chem Mater.*, 1994, **6**, 2317–2326.

11. A. A. Romero, M. D. Alba, W. Zhou and J. Klinowski, Synthesis and Characterization of the Mesoporous Silicate Molecular Sieve MCM-48, *J Phys Chem B*., 1997, **101**, 294–5300.

12. V. Alfredsson and M. W. Anderson, Structure of MCM-48 Revealed by Transmission Electron Microscopy, *Chem Mater*., 1996, **8**, 1141–1146.

13. Q. Huo, D. I. Margolese, U. Ciesla, P. Feng, T. E. Gier and P. Sieger, Generalized synthesis of periodic surfactant/inorganic composite materials, *Nature*, 1994, **368**, 317–321.

14. D. Zhao, J. Feng, Q. Huo, N. Melosh, G. H. Fredrickson and B. F. Chmelka, Triblock copolymer syntheses of mesoporous silica with periodic 50 to 300 angstrom pores, *Science*., 1998, **279**, 548–552.

15. D. Zhao, Q. Huo, J. Feng, B. F. Chmelka and G. D. Stucky, Nonionic triblock and star diblock copolymer and oligomeric surfactant syntheses of highly ordered, hydrothermally stable, mesoporous silica structures, *J Am Chem Soc*., 1998, **120**, 6024–6036.

16. T. Kimura, T. Kamata, M. Fuziwara, Y. Takano, M. Kaneda and Y. Sakamoto, Formation of novel ordered mesoporous silicas with square channels and their direct observation by transmission electron microscopy, *Angew Chem*., 2000, **39**, 3855-3859.

17. P. Schmidt-Winkel, W. W. Lukens, D. Zhao, P. Yang, B. F. Chmelka and G. D. Stucky, Mesocellular siliceous foams with uniformly sized cells and windows, *J Am Chem Soc*., 1999, **121**, 254–255.

18. S. Che, Z. Liu, T. Ohsuna, K. Sakamoto, O. Terasaki and T. Tatsumi, Synthesis and characterization of chiral mesoporous silica, *Nature*., 2004, **429**, 281–284.

19. U. Ciesla, D. Demuth, R. Leon, P. Petroff, G. Stucky and K. Unger, Surfactant controlled preparation of mesostructured transition-metal oxide compounds, *J Chem Soc. Chem Commun.*, 1994, **0**, 1387-1388.

20. Q. Huo, D. Margolese, U. Ciesla, P. Feng, T. E. Gier, P. Sieger, R. Leon, P. M. Petroff, F. Schüth and G. D. Stucky, Generalized synthesis of periodic surfactant-inorganic composite materials, *Nature*, 1994, **368**, 317–321.

21. P. Yang, D. Zhao, D. Margolese, B. Chmelka and G. Stucky, Generalized syntheses of large-poremesoporous metal oxideswith semicrystalline frameworks, *Nature*, **396**, 152–155.

22. M. Kruk, M. Jaroniec, R. Ryoo and S. H. Joo, Characterization of Ordered Mesoporous Carbons Synthesized Using MCM-48 Silicas as Templates, *J Phys Chem B.*, 2000, **104**, 7960–7968.

23. R. Ryoo, S. H. Joo and S. Jun. Synthesis of Highly Ordered Carbon Molecular Sieves via Template-Mediated Structural Transformation, *J Phys Chem B.*, 1999, **103**, 7743–7746.

24. H. J. Shin, R. Ryoo, M. Kruk and M. Jaroniec, Modification of SBA-15 pore connectivity by high-temperature calcination investigated by carbon inverse replication, *Chem Commun*., 2001, **4**, 349–350.

25. S. Che, K. Lund, T. Tatsumi, S. Iijima, S. H. Joo and R. Ryoo, Direct observation of 3D mesoporous structure by scanning electron microscopy (SEM): SBA-15 silica and CMK-5 carbon, *Angew Chem*., 2003, **42**, 2182–2185.

26. J. Lee, S. Han and T. Hyeon, Synthesis of new nanoporous carbon materials using nanostructured silica materials as templates, *J Mater Chem*., 2004, **14**, 478-486.

27. D. Gu, H. Bongard, Y. Meng, K. Miyasaka, O. Terasaki and F. Zhang, Growth of Single-Crystal Mesoporous Carbons with*Im* $\bar{3}$*m* Symmetry, *Chem Mater*., 2010, **22**, 4828–4833.

28. C. Liang and S. Dai, Synthesis of mesoporous carbon materials via enhanced hydrogen-bonding interaction, *J Am Chem Soc*., 2006, **128**, 5316–5317.

29. Y. Fang, D. Gu, Y. Zou, Z. Wu, F. Li and R. Che, A low-concentration hydrothermal synthesis of biocompatible ordered mesoporous carbon nanospheres with tunable and uniform size, *Angew Chem*., 2010, **49**, 7987–7991.

30. D. Gu, H. Bongard, Y. Deng, D. Feng, Z. Wu and Y. Fang, An aqueous emulsion route to synthesize mesoporous carbon vesicles and their nanocomposites, *Adv Mater Weinheim*., 2010, **22**, 833–837.

31. D. Feng, Y. Lv, Z. Wu, Y. Dou, L. Han and Z. Sun, Free-standing mesoporous carbon thin films with highly ordered pore architectures for nanodevices, *J Am Chem Soc*., 2011, **133**, 15148–15156.

32. J. Čejka and S. Mintova, Perspectives of micro/mesoporous composites in catalysis, *Catalysis Reviews*., 2007, **49**, 457–509.

33. Y. Deng, Y. Cai, Z. Sun, J. Liu, C. Liu and J. Wei, Multifunctional mesoporous composite microspheres with well-designed nanostructure: a highly integrated catalyst system, *J Am Chem Soc.*, 2010, **132**, 8466–8473.

34. D. M. Antonelli and J. Y. Ying, Mesoporous materials, *Current Opinion in Colloid & Interface Science*., 1996, **1**, 523–529.

35. D. M. Antonelli, A. Nakahira and J. Y. Ying, Ligand-Assisted Liquid Crystal Templating in Mesoporous Niobium Oxide Molecular Sieves, *Inorg Chem*., 1996, **35**, 3126–3136.

36. A. Taguchi and F. Schüth, Ordered mesoporous materials in catalysis, *Micropor Mesopor Mat*., 2005, **77**, 1–45.

37. M. Hartmann, Ordered Mesoporous Materials for Bioadsorption and Biocatalysis, *Chem Mater*., 2005, **17**, 4577–4593.

38. D. E. D. Vos, M. Dams, B. F. Sels and P. A. Jacobs, Ordered Mesoporous and Microporous Molecular Sieves Functionalized with Transition Metal Complexes as Catalysts for Selective Organic Transformations, *Chem Rev*., 2002, **102**, 3615–3640.

39. A. Corma, M. T. Navarro and J. P. Pariente, Synthesis of an ultralarge pore titanium silicate isomorphous to MCM-41 and its application as a catalyst for selective oxidation of hydrocarbons, *J Chem Soc Chem Commun*., 1994, **0**, 147-148.

40. K. M. Reddy, I Moudrakovski and A Sayari, Synthesis of mesoporous vanadium silicate molecular sieves, *J Chem Soc, Chem Commun*., 1994, **0**, 1059-1060.

41. J. M. Kisler, A. Dähler, G. W. Stevens and A. J. O'Connor, Separation of biological molecules using mesoporous molecular sieves, *Micropor Mesopor Mat*., 2001, **44-45**, 769–774.

42. M. Hartmann, A. Vinu and G. Chandrasekar, Adsorption of vitamin E on mesoporous carbon molecular sieves, *Chem Mater*., 2005, **17**, 829–833.

43. J. F. Díaz and K. J. Balkus, Enzyme immobilization in MCM-41 molecular sieve, *Journal of Molecular Catalysis B: Enzymatic*., 1996, **2**, 115–126.

44. M. E. Gimon-Kinsel, V. L. Jimenez, L. Washmon and K. J. Balkus, Mesoporous molecular sieve immobilized enzymes, *Stud Surf Sci Catal*., 1998, **117**, 373-380.

45. L. Washmon-Kriel, V. L. Jimenez and K. J. Balkus, Cytochrome c immobilization into mesoporous molecular sieves, *J Mol Catal B Enzym*., 2000, **10**, 453–469.

46. Y. Wang and F. Caruso, Mesoporous silica spheres as supports for enzyme immobilization and encapsulation, *Chem Mater*., 2005, **17**, 953–961.

47. M. Kruk, M. Jaroniec, C. H. Ko and R. Ryoo, Characterization of the Porous Structure of SBA-15, *Chem Mater*., 2000, **12**, 1961–1968.

48. H. H. P. Yiu and I. J. Bruce, Biological applications of organically functionalized mesoporous molecular sieves and related materials, *Studies in surface science and catalysi*, 2003, **146**, 581–584.

49. V. P. Torchilin, Recent advances with liposomes as pharmaceutical carriers, *Nat Rev Drug Discov*., 2005, **4**, 145–160.

50. J. W. Yoo and C. H. Lee, Drug delivery systems for hormone therapy, *J Control Release*., 2006, **112**, 1–14.

51. M. Malmsten, Soft drug delivery systems, *Soft Matter*. 2006, **2**, 760-769.

52. M. Vallet-Regi, A. Rámila, RP del Real and J Pérez-Pariente, A New Property of MCM-41: Drug Delivery System, *Chem Mater*, 2001, **13**, 308–311.

53. S. Radin, G. El-Bassyouni, E. J. Vresilovic, E. Schepers and P. Ducheyne, In vivo tissue response to resorbable silica xerogels as controlled-release materials. *Biomaterials*., 2005, **26**, 1043–1052.

54. P. Kortesuo, M. Ahola, S. Karlsson, I. Kangasniemi, A. Yli-Urpo and J. Kiesvaara, Silica xerogel as an implantable carrier for controlled drug delivery--evaluation of drug distribution and tissue effects after implantation, *Biomaterials*., 2000, **21**, 193–198.

55. S. Chia, J. Urano, F. Tamanoi, B. Dunn and J. I. Zink, Patterned hexagonal arrays of living cells in sol−gel silica films, *J Am Chem Soc*., 2000, **122**, 6488–6489.

56. B. C. Dave, B. Dunn, J. S. Valentine and J. I. Zink, Sol-gel encapsulation methods for biosensors, *Anal Chem*., 1994, **66**, 1120A–1127A.

57. W. Jin and J. D. Brennan, Properties and applications of proteins encapsulated within sol–gel derived materials, *Anal Chim Acta*., 2002, **461**, 1–36.

58. I. Gill, Bio-doped nanocomposite polymers: sol−gel bioencapsulates, *Chem Mater*. 2001, **13**, 3404–3421.

59. M. E. Davis, Ordered porous materials for emerging applications, *Nature*., 2002, **417**, 813–821.

60. A. G. Slater and A. I. Cooper, Function-led design of new porous materials, *Science*., 2015, **348**, 8075.

61. D. Chen, F. Huang, Y. B. Cheng and R. A. Caruso, Mesoporous anatase TiO_2 beads with high surface areas and controllable pore sizes: A superior candidate for high-performance dye-sensitized solar cells, *Adv Mater*., 2009, **21**, 2206–2210.

62. P. Tiwana, P. Docampo, M. B. Johnston, H. J. Snaith and L. M. Herz, Electron mobility and injection dynamics in mesoporous ZnO, SnO_2, and TiO_2 films used in dye-sensitized solar cells, *ACS Nano*., 2011, **5**, 5158–5166.

63. F. Dai, J. Zai, R. Yi, M. L. Gordin, H. Sohn and S. Chen, Bottom-up synthesis of high surface area mesoporous crystalline silicon and evaluation of its hydrogen evolution performance, *Nat Commun*. 2014, **5**, 3605.

64 . K. Sivula, R. Zboril, F. L. Formal, R. Robert, A. Weidenkaff and J. Tucek, Photoelectrochemical water splitting with mesoporous hematite prepared by a solution-based colloidal approach, *J Am Chem Soc*., 2010, **132**, 7436–7444.

65. T. W. Kim and K. S. Choi, Nanoporous $BiVO_4$ photoanodes with dual-layer oxygen evolution catalysts for solar water splitting, *Science*., 2014, **343**, 990–994.

66. T. Hisatomi, M. Otani, K. Nakajima, K. Teramura, Y. Kako and D. Lu, Preparation of crystallized mesoporous Ta_3N_5 assisted by chemical vapor deposition of tetramethyl orthosilicate, *Chem Mater*., 2010, **22**, 3854–3861.

67. X. Wang, K. Maeda, X. Chen, K. Takanabe, K. Domen and Y. Hou, Polymer semiconductors for artificial photosynthesis: hydrogen evolution by mesoporous graphitic carbon nitride with visible light, *J Am Chem Soc*., 2009, **131**, 1680–1681.

68. J. M. Kisler, G. W. Stevens and A. J. O´Connor, Adsorption of proteins on mesoporous molecular sieves, *Mater Phys Mech*., 2001, **4**, 89-93.

69. J. K. Kim, K. Shin, S. M. Cho, TW Lee and JH Park, Synthesis of transparent mesoporous tungsten trioxide films with enhanced photoelectrochemical response: application to unassisted solar water splitting, *Energy Environ Sci*., 2011, **4**, 1465-1470.

70. F. Jiao, J. Bao, A. H. Hill and P. G. Bruce, Synthesis of ordered mesoporous Li-Mn-O spinel as a positive electrode for rechargeable lithium batteries, *Angew Chem Int Ed Engl*., 2008, **47**, 9711–9716.

71. W. Li, J. Liu and D. Zhao, Mesoporous materials for energy conversion and storage devices, *Nat Rev Mater*., 2016, **1**, 16023.

72. F. Jiao, K. M. Shaju and P. G. Bruce, Synthesis of nanowire and mesoporous low-temperature $LiCoO_2$ by a post-templating reaction, *Angew Chem Int Ed Engl*. 2005, **44**, 6550–6553.

73. N. D. Petkovich and A. Stein, Controlling macro- and mesostructures with hierarchical porosity through combined hard and soft templating, *Chem Soc Rev*., 2013, **42**, 3721–3739.

74. D. Gu and F. Schüth, Synthesis of non-siliceous mesoporous oxides, *Chem Soc Rev*. 2014, **43**, 313–344.

75. Y. Shi, Y. Wan and D. Zhao, Ordered mesoporous non-oxide materials, *Chem Soc Rev*. 2011, **40**, 3854–3878.

76. W. Li, Q. Yue, Y. Deng and D. Zhao, Ordered mesoporous materials based on interfacial assembly and engineering, *Adv Mater*., 2013, **25**, 5129-5152.

77. W. Xuan, C. Zhu, Y. Liu and Y. Cui, Mesoporous metal-organic framework materials, *Chem Soc Rev*., 2012, **41**, 1677–1695.

78. W. Li, Z. Wu, J. Wang, A. A. Elzatahry and D. Zhao, A perspective on mesoporous TiO_2 materials, *Chem Mater*., 2014, **26**, 287–298.

79. Y. Wan and D. Zhao, On the controllable soft-templating approach to mesoporous silicates, *Chem Rev*., 2007, **107**, 2821–2860.

80. D. Wu, F. Xu, B. Sun, R. Fu, H. He and K. Matyjaszewski, Design and preparation of porous polymers, *Chem Rev*., 2012, **112**, 3959–4015.

81. R. Zhang, D. Shen, M. Xu, D. Feng, W. Li and G. Zheng, Ordered macro-/mesoporous anatase films with high thermal stability and crystallinity for photoelectrocatalytic water-splitting, *Adv Energy Mater*., 2014, **4**, 1301725.

82. X. Feng, X. Ding and D. Jiang, Covalent organic frameworks, *Chem Soc Rev*., 2012, **41**, 6010–6022.

83. A. Corma, From microporous to mesoporous molecular sieve materials and their use in catalysis, *Chem Rev*., 1997, **97**, 2373–2420.

84. R. Lv, C. Cao, H. Zhai, D. Wang, S. Liu and H. Zhu, Growth and characterization of single-crystal ZnSe nanorods via surfactant soft-template method, *Solid State Commun*., 2004, **130**, 241–245.

85. J. Jang and J. Bae, Fabrication of mesoporous polymer using soft template method, *Chem Commun*., 2005, **9**, 1200–1202.

86. X. J. Wu and D. Xu, Soft template synthesis of yolk/silica shell particles, *Adv Mater*., 2010, **22**, 1516–1520.

87. J. Liu, T. Yang, D. W. Wang, G. Q. M. Lu, D. Zhao and S. Z. Qiao, A facile soft-template synthesis of mesoporous polymeric and carbonaceous nanospheres, *Nat Commun*., 2013, **4**, 2798.

88. N. Pal and A. Bhaumik, Soft templating strategies for the synthesis of mesoporous materials: inorganic, organic-inorganic hybrid and purely organic solids, *Adv Colloid Interface Sci*., 2013, **189-190**, 21–41.

89. P. Alexandridis, U. Olsson and B. Lindman, A record nine different phases (four cubic, two hexagonal, and one lamellar lyotropic liquid crystalline and two micellar solutions) in a ternary isothermal system of an amphiphilic block copolymer and selective solvents (water and oil), *Langmuir*., 1998, **14**, 2627–2638.

90. W. Li and D. Zhao, An overview of the synthesis of ordered mesoporous materials, *Chem Commun*., 2013, **49**, 943–946.

91. J. Wei, H. Wang, Y. Deng, Z. Sun, L. Shi and B. Tu, Solvent evaporation induced aggregating assembly approach to three-dimensional ordered mesoporous silica with ultralarge accessible mesopores, *J Am Chem Soc*., 2011, **133**, 20369–20377.

92. Y. Deng, J. Wei, Z. Sun and D. Zhao, Large-pore ordered mesoporous materials templated from non-Pluronic amphiphilic block copolymers, *Chem Soc Rev*., 2013, **42**, 4054–4070.

93. Y. Liu, R. Che, G. Chen, J. Fan, Z. Sun and Z. Wu, Radially oriented mesoporous TiO_2 microspheres with single-crystal-like anatase walls for high-efficiency optoelectronic devices, *Sci Adv*., 2015, **1**, 500166.

94. Y. Liu, Y. Luo, A. A. Elzatahry, W. Luo, R. Che and J. Fan, Mesoporous TiO_2 Mesocrystals: remarkable defects-induced crystallite-interface reactivity and their in-situ conversion to single crystals, *ACS Cent Sci*., 2015, **1**, 400–408.

95. S. Guldin, S. Hüttner, P. Tiwana, M. C. Orilall, B. Ülgüt and M. Stefik, Improved conductivity in dye-sensitised solar cells through block-copolymer confined TiO_2 crystallization, *Energy Environ Sci*., 2011, **4**, 225–233.

96. S. K. Pathak, A. Abate, P. Ruckdeschel, B. Roose, K. C. Gödel and Y. Vaynzof, Performance and stability enhancement of dye-sensitized and perovskite solar cells by Al doping of TiO_2, *Adv Funct Mater*., 2014, **24**, 6046–6055.

97. S. Ghosh, N. A. Kouamé, L. Ramos, S. Remita, A. Dazzi and A. Deniset-Besseau, Conducting polymer nanostructures for photocatalysis under visible light, *Nat Mater*., 2015, **14**, 505–511.

98. W. Zhou, W. Li, J. Q. Wang, Y. Qu, Y. Yang and Y. Xie, Ordered mesoporous black TiO_2 as highly efficient hydrogen evolution photocatalyst, *J Am Chem Soc*., 2014, **136**, 9280–9283.

99. R. Zhang, Y. Du, D. Li, D. Shen, J. Yang and Z. Guo, Highly reversible and large lithium storage in mesoporous Si/C nanocomposite anodes with silicon nanoparticles embedded in a carbon framework, *Adv Mater*., 2014, **26**, 6749–6755.

100. C. Jo, Y. Kim, J. Hwang, J. Shim, J. Chun and J. Lee, Block copolymer directed ordered mesostructured $TiNb_2O_7$ multimetallic oxide constructed of nanocrystals as high-power Li-ion battery anodes, *Chem Mater*., 2014, **26**, 3508–3514.

101. S. H. Oh, R. Black, E. Pomerantseva, J. H. Lee and L. F. Nazar, Synthesis of a metallic mesoporous pyrochlore as a catalyst for lithium–O_2 batteries, *Nat Chem*., 2012, **4**, 1004–1010.

102. C. Jo, J. Hwang, H. Song, A. H. Dao, Y. Kim and S. H. Lee, Block-copolymer-assisted one-pot synthesis of ordered mesoporous WO_{3-x}/carbon nanocomposites as high-rate-performance electrodes for pseudocapacitors, *Adv Funct Mater*., 2013, **23**, 3747-3754.

103. T. Brezesinski, J. Wang, J. Polleux, B. Dunn and S. H. Tolbert, Templated nanocrystal-based porous TiO_2 films for next-generation electrochemical capacitors, *J Am Chem Soc*., 2009, **131**, 1802–1809.

104. K. Brezesinski, J. Wang, J. Haetge, C. Reitz, S. O. Steinmueller and S. H. Tolbert, Pseudocapacitive contributions to charge storage in highly ordered mesoporous group V transition metal oxides with iso-oriented layered nanocrystalline domains, *J Am Chem Soc*., 2010, **132**, 6982–6990.

105. V. Augustyn, J. Come, M. A. Lowe, J. W. Kim, P. L. Taberna and S. H. Tolbert, High-rate electrochemical energy storage through Li^+ intercalation pseudocapacitance, *Nat Mater*., 2013, **12**, 518–522.

106. T. Brezesinski, J. Wang, R. Senter, K. Brezesinski, B. Dunn and S. H. Tolbert, On the correlation between mechanical flexibility, nanoscale structure, and charge storage in periodic mesoporous CeO_2 thin films, *ACS Nano*., 2010, **4**, 967–977.

107. T. Brezesinski, J. Wang, S. H. Tolbert and B. Dunn, Ordered mesoporous alpha-MoO_3 with iso-oriented nanocrystalline walls for thin-film pseudocapacitors, *Nat Mater*., 2010, **9**, 146–151.

108. Z. Wu, Y. Lv, Y. Xia, P. A. Webley and D. Zhao, Ordered mesoporous platinum @ graphitic carbon embedded nanophase as a highly active, stable, and methanol-tolerant oxygen reduction electrocatalyst, *J Am Chem Soc*., 2012, **134**, 2236–2245.

109. M. C. Orilall, F. Matsumoto, Q. Zhou, H. Sai, H. D. Abruña and F. J. DiSalvo, One-pot synthesis of platinum-based nanoparticles incorporated into mesoporous niobium oxide-carbon composites for fuel cell electrodes, *J Am Chem Soc*., 2009, **131**, 9389–9395.

110. J. Wei, D. Zhou, Z. Sun, Y. Deng, Y. Xia and D. Zhao, A controllable synthesis of rich nitrogen-doped ordered mesoporous carbon for CO_2 capture and supercapacitors, *Adv Funct Mater*., 2013, **23**, 2322-2328.

111. J. Shim, J. Lee, Y. Ye, J. Hwang, S. K. Kim and T. H. Lim, One-pot synthesis of intermetallic electrocatalysts in ordered, large-pore mesoporous carbon/silica toward formic acid oxidation, *ACS Nano*., 2012, **6**, 6870–6881.

112. B. Kong, J. Tang, Y. Zhang, T. Jiang, X. Gong and C. Peng, Incorporation of well-dispersed sub-5-nm graphitic pencil nanodots into ordered mesoporous frameworks, *Nat Chem*., 2016, **8**, 171–178.

113. F. Kleitz, S. H. Choi and R. Ryoo, Cubic Ia3d large mesoporous silica: synthesis and replication to platinum nanowires, carbon nanorods and carbon nanotubes, *Chem Commun*., 2003, **0**, 2136-2137.

114. E. Ramasamy and J. Lee, Large-pore sized mesoporous carbon electrocatalyst for efficient dye-sensitized solar cells, *Chem Commun*., 2010, **46**, 2136–2138.

115. I. Jeong, C. Jo, A. Anthonysamy, J. M. Kim, E. Kang and J. Hwang, Ordered mesoporous tungsten suboxide counter electrode for highly efficient iodine-free electrolyte-based dye-sensitized solar cells, *Chem Sus Chem*., 2013, **6**, 299–307.

116. T. Grewe, X. Deng, C. Weidenthaler, F. Schüth and H. Tüysüz, Design of ordered mesoporous composite materials and their electrocatalytic activities for water oxidation, *Chem Mater*., 2013, **25**, 4926–4935.

117. Y. Jiao, D. Han, L. Liu, L. Ji, G. Guo and J. Hu, Highly ordered mesoporous few-layer graphene frameworks enabled by Fe_3O_4 nanocrystal superlattices. *Angew Chem Int Ed Engl*., 2015, **54**, 5727–5731.

118. H. Liu, D. Su, R. Zhou, B. Sun, G. Wang and S. Z. Qiao, Highly ordered mesoporous MoS_2 with expanded spacing of the (002) crystal plane for ultrafast lithium ion storage, *Adv Energy Mater*., 2012, **2**, 970–975.

119. D. Gu, W. Li, F. Wang, H. Bongard, B. Spliethoff and W. Schmidt, Controllable synthesis of mesoporous peapod-like Co_3O_4@carbon nanotube arrays for high-performance lithium-ion batteries, *Angew Chem Int Ed Engl*., 2015, **54**, 7060–7064.

120. X. Ji, K. T. Lee and L. F. Nazar, A highly ordered nanostructured carbon-sulphur cathode for lithium-sulphur batteries, *Nat Mater*., 2009, **8**, 500–506.

121. J. Xie, X. Yao, Q. Cheng, I. P. Madden, P. Dornath and C. C. Chang, Three dimensionally ordered mesoporous carbon as a stable, high-performance Li-O_2 battery cathode, *Angew Chem Int Ed Engl*., 2015, **54**, 4299–4303.

122. J. S. Lee, S. I. Kim, J. C. Yoon and J. H. Jang, Chemical vapor deposition of mesoporous graphene nanoballs for supercapacitor, *ACS Nano*., 2013, **7**, 6047–6055.

123. A. Vu, X. Li, J. Phillips, A. Han, W. H. Smyrl and P. Bühlmann, Three-dimensionally ordered Mesoporous (3DOm) carbon materials as electrodes for electrochemical double-layer capacitors with ionic liquid electrolytes, *Chem Mater*., 2013, **25**, 4137–4148.

124. C. Cui, W. Qian, Y. Yu, C. Kong, B. Yu and L. Xiang, Highly electroconductive mesoporous graphene nanofibers and their capacitance performance at 4 V, *J Am Chem Soc*., 2014, **136**, 2256–2259.

125. Z. Wu, W. Li, Y. Xia, P. Webley and D. Zhao, Ordered mesoporous graphitized pyrolytic carbon materials: synthesis, graphitization, and electrochemical properties, *J Mater Chem*., 2012, **22**, 8835-8845.

126. A. Pendashteh, S. E. Moosavifard, M. S. Rahmanifar, Y. Wang, M. F. El-Kady and R. B. Kaner, Highly ordered mesoporous $CuCo_2O_4$ nanowires, a promising solution for high-performance supercapacitors, *Chem Mater*., 2015, **27**, 3919–3926.

127. Z. Cui, M. Yang, H. Chen, M. Zhao and F. J. DiSalvo, Mesoporous TiN as a noncarbon support of Ag-rich PtAg nanoalloy catalysts for oxygen reduction reaction in alkaline media, *Chem Sus Chem*., 2014, **7**, 3356–3361.

128. W. Li, Y. Deng, Z. Wu, X. Qian, J. Yang and Y. Wang, Hydrothermal etching assisted crystallization: a facile route to functional yolk-shell titanate microspheres with ultrathin nanosheets-assembled double shells, *J Am Chem Soc*., 2011, **133**, 15830–15833.

129. X. Fei, W. Li, Z. Shao, S. Seeger, D. Zhao and X. Chen, Protein biomineralized nanoporous inorganic mesocrystals with tunable hierarchical nanostructures, *J Am Chem Soc*., 2014, **136**, 15781–15786.

130. B. Chi, L. Zhao and T. Jin, One-step template-free route for synthesis of mesoporous N-doped titania spheres, *J Phys Chem C*., 2007, **111**, 6189–6193.

131. N. Lakshminarasimhan, E. Bae and W. Choi, Enhanced photocatalytic production of H_2 on mesoporous TiO_2 prepared by template-free method: Role of interparticle charge transfer, *J Phys Chem C*., 2007, **111**, 15244–15250.

132. N. Li, G. Liu, C. Zhen, F. Li, L. Zhang and H. M. Cheng, Battery performance and photocatalytic activity of mesoporous anatase TiO_2 nanospheres/graphene composites by template-free self-assembly, *Adv Funct Mater*., 2011, **21**, 1717–1722.

133. C. Yu, X. Dong, L. Guo, J. Li, F. Qin and L. Zhang, Template-free preparation of mesoporous Fe_2O_3 and its application as absorbents, *J Phys Chem C*., 2008, **112**, 13378–13382.

134. S. Manna, K. Das and S. K. De, Template-free synthesis of mesoporous CuO dandelion structures for optoelectronic applications, *ACS Appl Mater Interfaces*., 2010, **2**, 1536–1542.

135. S. W. Bian, J. Baltrusaitis, P. Galhotra and V. H. Grassian, A template-free, thermal decomposition method to synthesize mesoporous MgO with a nanocrystalline framework and its application in carbon dioxide adsorption, *J Mater Chem*., 2010, **20**, 8705-8710.

136. J. Qian, M. Zhou, Y. Cao, X. Ai and H. Yang, Template-free hydrothermal synthesis of nanoembossed mesoporous $LiFePO_4$ microspheres for high-performance lithium-ion batteries, *J Phys Chem C*., 2010, **114**, 3477–3482.

137. X. Wang, S. Cheng and J. C. C. Chan, Propylsulfonic acid-functionalized mesoporous silica synthesized by in situ oxidation of thiol groups under template-free condition, *J Phys Chem C*., 2007, **111**, 2156–2164.

138. A. Yildirim, H. Budunoglu, H. Deniz, M. O. Guler and M. Bayindir, Template-free synthesis of organically modified silica mesoporous thin films for TNT sensing, *ACS Appl Mater Interfaces*., 2010, **2**, 2892–2897.

139. D. Nguyen, W. Wang, H. Long, W. Shan, X. Li and M. Fang, A facile and controllable multi-templating approach based on a solo nonionic surfactant to preparing nanocrystalline bimodal meso-mesoporous titania, *Micropor Mesopor Mat*., 2016, **230**, 177–187.

140. W. Li, M. Liu, S. Feng, X. Li, J. Wang and D. Shen, Template-free synthesis of uniform magnetic mesoporous TiO_2 nanospindles for highly selective enrichment of phosphopeptides, *Mater Horiz*., 2014, **1**, 439-445.

141. L. Peng, J. Zhang, Z. Xue, B. Han, X. Sang and C. Liu, Highly mesoporous metal-organic framework assembled in a switchable solvent, *Nat Commun*., 2014, **5**, 4465.

142. H. Sai, K. W. Tan, K. Hur, E. A. Smith, R. Hovden and Y. Jiang, Hierarchical porous polymer scaffolds from block copolymers, *Science*., 2013, **341**, 530–534.

143. J. Hwang, C. Jo, K. Hur, J. Lim, S. Kim and J. Lee, Direct access to hierarchically porous inorganic oxide materials with three-dimensionally interconnected networks, *J Am Chem Soc*., 2014, **136**, 16066–16072.

144. K. Nakanishi and N. Tanaka, Sol-gel with phase separation. Hierarchically porous materials optimized for high-performance liquid chromatography separations, *Acc Chem Res*., 2007, **40**, 863–873.

145. N. Abdullah and S. K. Kamarudin, Titanium dioxide in fuel cell technology: An overview, *J Power Sources*., 2015, **278**, 109–118.

146. Y. Liu, L. Tian, X. Tan, X. Li and X. Chen, Synthesis, properties, and applications of black titanium dioxide nanomaterials, *Sci Bull*., 2017, **62**, 431–441.

147. A. Fujishima, K. Honda, Electrochemical photolysis of water at a semiconductor electrode, *Nature*., 1972, **238**, 37-38.

148. Y. Matsumoto, M. Murakami, T. Shono, T. Hasegawa, T. Fukumura and M. Kawasaki, Room-temperature ferromagnetism in transparent transition metal-doped titanium dioxide, *Science*., 2001, **291**, 854–856.

149. M. Knei, M. Jenderka, K. Brachwitz, M. Lorenz and M. Grundmann, Modeling the electrical transport in epitaxial undoped and Ni-, Cr-, and W-doped TiO_2 anatase thin films, *Appl Phys Lett*., 2014, **105**, 062103.

150. Z. Jiao, Y. Zhang, T. Chen, Q. Dong, G. Lu and Y. Bi, TiO_2 nanotube arrays modified with Cr-doped $SrTiO_3$ nanocubes for highly efficient hydrogen evolution under visible light. *Chemistry (Easton)*., 2014, **20**, 2654–2662.

151. Z. Yao, F. Jia, S. Tian, C. Li, Z. Jiang and X. Bai, Microporous Ni-doped TiO_2 film photocatalyst by plasma electrolytic oxidation, *ACS Appl Mater Interfaces*., 2010, **2**, 2617–2622.

152. N. Roy, K. T. Leung and D. Pradhan, Nitrogen doped reduced graphene oxide based Pt–TiO_2 nanocomposites for enhanced hydrogen evolution. *J Phys Chem C*., 2015, **119**, 19117–19125.

153. J. Yu, Q. Xiang and M. Zhou, Preparation, characterization and visible-light-driven photocatalytic activity of Fe-doped titania nanorods and first-principles study for electronic structures, *Appl Catal B*., 2009, **90**, 595–602.

154. Y. H. Peng, G. F. Huang and W. Q. Huang, Visible-light absorption and photocatalytic activity of Cr-doped TiO_2 nanocrystal films, *Adv. Powder Tech.*., 2012, **23**, 8–12.

155. L. Deng, S. Wang, D. Liu, B. Zhu, W. Huang and S. Wu, Synthesis, characterization of Fe-doped TiO_2 nanotubes with high photocatalytic activity, *Catal Lett*., 2009, **129**, 513–518.

156. S. A. Chambers, S. Thevuthasan, R. F. C. Farrow, R. F. Marks, J. U. Thiele and L. Folks, Epitaxial growth and properties of ferromagnetic co-doped TiO_2 anatase, *Appl Phys Lett*., 2001, **79**, 3467–3469.

157. N. T. Q. Hoa, Solvothermal synthesis and photocatalytic activity of Co-doped TiO_2 nanowires, *IJNT*., 2015, **12**, 426-433.

158. B. Liu, H. M. Chen, C. Liu, S. C. Andrews, C. Hahn and P. Yang, Large-scale synthesis of transition-metal-doped TiO_2 nanowires with controllable overpotential, *J Am Chem Soc*., 2013, **135**, 9995–9998.

159. T. Zhang, B. Yu, D. Wang and F. Zhou, Molybdenum-doped and anatase/rutile mixed-phase TiO_2 nanotube photoelectrode for high photoelectrochemical performance, *J Power Sources*., 2015, **281**, 411–416.

160. M. Mollavali, C. Falamaki and S. Rohani, Preparation of multiple-doped TiO_2 nanotube arrays with nitrogen, carbon and nickel with enhanced visible light photoelectrochemical activity via single-step anodization, *Int J Hydrogen Energy*., 2015, **40**, 12239–12252.

161. X. Chen and C. Burda, The electronic origin of the visible-light absorption properties of C-, N- and S-doped TiO_2 nanomaterials, *J Am Chem Soc*., 2008, **130**, 5018–5019.

162. R. Asahi, T. Morikawa, T. Ohwaki, K. Aoki and Y. Taga, Visible-light photocatalysis in nitrogen-doped titanium oxides, *Science*., 2001, **293**, 269–271.

163. J. H. Park, S. Kim and A. J. Bard, Novel carbon-doped TiO_2 nanotube arrays with high aspect ratios for efficient solar water splitting, *Nano Lett*., 2006, **6**, 24–28.

164. R. Asahi, T. Morikawa, H. Irie and T. Ohwaki, Nitrogen-doped titanium dioxide as visible-light-sensitive photocatalyst: designs, developments, and prospects, *Chem Rev*., 2014, **114**, 9824–9852.

165. K. Yang, Y. Dai and B. Huang, Study of the nitrogen concentration influence on N-doped TiO_2 anatase from first-principles calculations. *J Phys Chem C*., 2007, **111**, 12086–12090.

166. Q. Deng, Y. Liu, K. Mu, Y. Zeng, G. Yang and F. Shen, Preparation and characterization of F-modified C-TiO_2 and its photocatalytic properties, *Phys Stat Sol (a)*., 2015, **212**, 691–697.

167. H. Li, X. Zhang, Y. Huo and J. Zhu, Supercritical preparation of a highly active S-doped TiO_2 photocatalyst for methylene blue mineralization, *Environ Sci Technol*., 2007, **41**, 4410–4414.

168. K. Yang, Y. Dai and B. Huang, Understanding photocatalytic activity of S- and P-doped TiO_2 under visible light from first-principles, *J Phys Chem C*., 2007, **111**, 18985–18994.

169. W. Zhou, Y. Liu, Y. Zhang, G. Yang, S. Deng and F. Shen, Novel multi-layer cross-linked TiO_2/C nanosheets and their photocatalytic properties, *New J Chem*., 2014, **38**, 1647-1654.

170. Y. Zhang, Y. Liu, L. Wang, Q. Deng, G. Yang and S. Deng, Preparation and characterization of carbon-modified TiO_2 composite, *Micro & Nano Letters*., 2014, **9**, 471–474.

171. T. Xia, W. Zhang, Z. Wang, Y. Zhang, X. Song and J. Murowchick, Amorphous carbon-coated TiO_2 nanocrystals for improved lithium-ion battery and photocatalytic performance, *Nano Energy*., 2014, **6**, 109–118.

172. M. K. Seery, R. George, P. Floris and S. Phillai, Silver doped titanium dioxide nanomaterials for enhanced visible light photocatalysis, *J. Photochem. Photobiol*., 2007, **189**, 258-263.

173. K. C. Ok, J. Park, J. H. Lee, A. B. Du, J. L. Hun and K. B. Chung, Semiconducting behavior of niobium-doped titanium oxide in the amorphous state, *Appl Phys Lett*., 2012, **100**, 142103.

174. S. Y. Jung, T. J. Ha, C. S. Park, W. S. Seo, Y. S. Lim and S. Shin, Improvement in the conductivity ratio of ordered mesoporous Ag-TiO_2 thin films for thermoelectric materials, *Thin Solid Films*., 2013, **529**, 94–97.

175. W. Maret, Metals on the move: zinc ions in cellular regulation and in the coordination dynamics of zinc proteins, *Biometals*., 2011, **24**, 411–418.

176. H. Tapiero and K. D. Tew, Trace elements in human physiology and pathology: zinc and metallothioneins, *Biomedicine & Pharmacotherapy*., 2003, **57**, 399–411.

177. C. J. Frederickson, J. Y. Koh and A. I. Bush, The neurobiology of zinc in health and disease, *Nat Rev Neurosci*., 2005, **6**, 449–462.

178. L. Vayssieres, K. Keis, A. Hagfeldt and S. E. Lindquist, Three-dimensional array of highly oriented crystalline ZnO microtubes, *Chem Mater*., 2001, **13**, 4395–4398.

179. M. H. Huang, S. Mao, H. Feick, H. Yan, Y. Wu and H. Kind, Room-temperature ultraviolet nanowire nanolasers, *Science*., 2001, **292**, 1897–1899.

180. J. S. Wellings, N. B. Chaure, S. N. Heavens and I. M. Dharmadasa, Growth and characterization of electrodeposited ZnO thin films, *Thin Solid Films*., 2008, **516**, 3893–3898.

181. Z. Deng, M. Chen, G. Gu and L. Wu, A facile method to fabricate ZnO hollow spheres and their photocatalytic property, *J Phys Chem B*., 2008, **112**, 16–22.

182. S. J. Yang and C. R. Park, Facile preparation of monodisperse ZnO quantum dots with high quality photoluminescence characteristics, *Nanotechnology*., 2008, **19**, 035609.

183. J. Xie, Y. Cao, D. Jia, Y. Li and Y. Wang, Solid-state synthesis of Y-doped ZnO nanoparticles with selective-detection gas-sensing performance, *Ceramics International*., 2016, **42**, 90–96.

184. J. Guo and C. Peng, Synthesis of ZnO nanoparticles with a novel combustion method and their C_2H_5OH gas sensing properties, *Ceramics International*., 2015, **41**, 2180–2186.

185. P. J. Lu, S. C. Huang, Y. P. Chen, L. C. Chiueh and D. Y. C. Shih, Analysis of titanium dioxide and zinc oxide nanoparticles in cosmetics, *J Food Drug Anal*., 2015, **23**, 587–594.

186. M. Rajalakshmi, S. Sohila, S. Ramya, R. Divakar, C. Ghosh and S. Kalavathi, Blue green and UV emitting ZnO nanoparticles synthesized through a non-aqueous route, *Opt Mater*., 2012, **34**, 1241–1245.

187. N. Izu, K. Shimada, T. Akamatsu, T. Itoh, W. Shin and K. Shiraishi, Polyol synthesis of Al-doped ZnO spherical nanoparticles and their UV–vis–NIR absorption properties, *Ceram. Int*., 2014, **40**, 8775–8781.

188. Y. C. Kong, D. P. Yu, B. Zhang, W. Fang, S. Q. Feng, Ultraviolet-emitting ZnO nanowires synthesized by a physical vapor deposition approach. *Appl Phys Lett*., 2001, **78**, 407–409.

189. C. Zou, F. Liang and S. Xue, Synthesis and oxygen vacancy-related photocatalytic properties of ZnO nanotubes grown by thermal evaporation, *Res Chem Intermed*., 2015, **41**, 5167–5176.

190. K. K. Kim, D. Kim, S. K. Kim, S. M. Park an J. K. Song, Formation of ZnO nanoparticles by laser ablation in neat water, *Chem Phys Lett*., 2011, **511**, 116–120.

191. L. F. Dong, Z. L. Cui and Z. K. Zhang, Gas sensing properties of nano-ZnO prepared by arc plasma method, *Nanostructured Materials*., 1997, **8**, 815-823.

192. G. Applerot, A. Lipovsky, R. Dror, N. Perkas, Y. Nitzan and R. Lubart, Enhanced antibacterial activity of nanocrystalline ZnO due to increased ROS-mediated cell injury, *Adv Funct Mater*., 2009, **19**, 842–852.

193. L. Xu, Y. L. Hu, C. Pelligra, C. H. Chen, L. Jin and H. Huang, ZnO with different morphologies synthesized by solvothermal methods for enhanced photocatalytic activity, *Chem Mater*., 2009, **21**, 2875–2885.

194. S. Sepulveda-Guzman, B. Reeja-Jayan, E. Rosa, A. Torres-Castro, V. Gonzalez-Gonzalez and M. Jose-Yacaman, Synthesis of assembled ZnO structures by precipitation method in aqueous media, *Materials Chemistry and Physics*., 2009, **115**, 172–178.

195. B. Ristic and P. Smets, Fusion of uncertain combat identity declarations and implication rules using the belief function theory, *Signal and Data Processing of Small Targets.*, 2005, 591318.

196. Y. Zhou, W. Wu, G. Hu, H. Wu and S. Cui, Hydrothermal synthesis of ZnO nanorod arrays with Synthesis of assembled ZnO structures by precipitation method in aqueous media the addition of polyethyleneimine, *Mater Res Bull*., 2008, **43**, 2113–2118.

197. E. L. Ratcliff, A. K. Sigdel, M. R. Macech, K. Nebesny, P. A. Lee and D. S. Ginley, Surface composition, work function, and electrochemical characteristics of gallium-doped zinc oxide, *Thin Solid Films*., 2012, **520**, 5652–5663.

198. V. Bhosle, A. Tiwari and J. Narayan, Electrical properties of transparent and conducting Ga doped ZnO, *J Appl Phys*., 2006, **100**, 033713.

199. M. Hiramatsu, K. Imaeda, N. Horio and M. Nawata, Transparent conducting ZnO thin films prepared by XeCl excimer laser ablation, *J Vac Sci Technol A*., 1998, **16**, 669–673.

200. B. K. Meyer, J. Sann, D. M. Hofmann, C. Neumann and A. Zeuner, Shallow donors and acceptors in ZnO, *Semicond Sci Technol*., 2005, **20**, 62–66.

201. H. Chen, A. Du Pasquier, G. Saraf, J. Zhong and Y. Lu, Dye-sensitized solar cells using ZnO nanotips and Ga-doped ZnO films, *Semicond Sci Technol*., 2008, **23**, 045004.

202. E. Fortunato, D. Ginley, H. Hosono and D. C. Paine, Transparent conducting oxides for photovoltaics, *MRS Bull*., 2007, **32**, 242–247.

203. V. Bhosle, J. T. Prater, F. Yang, D. Burk, S. R. Forrest and J. Narayan, Gallium-doped zinc oxide films as transparent electrodes for organic solar cell applications, *J Appl Phys*., 2007, **102**, 023501.

204. S. Tanaka, A. A. Zakhidov, R. Ovalle-Robles, Y. Yoshida, I. Hiromitsu and Y. Fujita, Semitransparent organic photovoltaic cell with carbon nanotube-sheet anodes and Ga-doped ZnO cathodes, *Synth Met*., 2009, **159**, 2326–2328.

205. H. K. Park, J. A. Jeong, Y. S. Park, S. I. Na, D. Y. Kim and H. K. Kim, Room-temperature Indium-free Ga: ZnO/Ag/Ga: ZnO multilayer electrode for organic solar cell applications, *Electrochem Solid-State Lett*., 2009, **12**, 309-311.

206. H. K. Park, J. W. Kang, S. I. Na, D. Y. Kim and H. K. Kim, Characteristics of indium-free GZO/Ag/GZO and AZO/Ag/AZO multilayer electrode grown by dual target DC sputtering at room temperature for low-cost organic photovoltaics, *Solar Energy Materials and Solar Cells*., 2009, **93**, 1994–2002.

207. I. B. Shim and C. S. Kim, Doping effect of indium oxide-based diluted magnetic semiconductor thin films, *J Magn Magn Mater*., 2004, **272-276**, 1571–1572.

208. S. H. Babu, S. Kaleemulla, N. M. Rao and C. Krishnamoorthi, Indium oxide: A transparent, conducting ferromagnetic semiconductor for spintronic applications, *J Magn Magn Mater*., 2016, **416**, 66–74.

209. R. E. Triambulo, H. G. Cheong, G. H. Lee, I. S. Yi, J. W. Park, A transparent conductive oxide electrode with highly enhanced flexibility achieved by controlled crystallinity by incorporating Ag nanoparticles on substrates, *J Alloys Compd*., 2015, **620**, 340–349.

210. D. Li, D. K. Li, H. Z. Wu, F. Liang, W. Xie and C. W. Zou, Defects related room temperature ferromagnetism in Cu-implanted ZnO nanorod arrays, *J Alloys Compd*., 2014, **591**, 80–84.

211. K. P. Sibin, N. Swain, P. Chowdhury, A. Dey, N. Sridhara and H. D. Shashikala, Optical and electrical properties of ITO thin films sputtered on flexible FEP substrate as passive thermal control system for space applications, *Solar Energy Materials and Solar Cells*., 2016, **145**, 314–322.

212. J. Xu, Y. Chen and J. Shen, Ethanol sensor based on hexagonal indium oxide nanorods prepared by solvothermal methods, *Mater Lett*., 2008, **62**, 1363–1365.

213. K. Soulantica, L. Erades, M. Sauvan, F. Senocq, A. Maisonnat and B. Chaudret, Synthesis of indium and indium oxide nanoparticles from indium cyclopentadienyl precursor and their application for gas sensing, *Adv Funct Mater*., 2003, **13**, 553–557.

214. F. O. Adurodija, H. Izumi, T. Ishihara, H. Yoshioka, M. Motoyama and K. Murai, Influence of substrate temperature on the properties of indium oxide thin films, *J Vac Sci Technol A*., 2000, **18**, 814–818.

215. Y. Shigesato, S. Takaki and T. Haranoh, Electrical and structural properties of low resistivity tin-doped indium oxide films, *J Appl Phys*., 1992, **71**, 3356–3364.

216. W. S. Seo, H. H. Jo, K. Lee and J. T. Park, Preparation and optical properties of highly crystalline, colloidal, and size-controlled indium oxide nanoparticles, *Adv Mater*., 2003, **15**, 795–797.

217. C. Li, D. Zhang, X Liu, S Han, T Tang and J Han, In_2O_3 nanowires as chemical sensors, *Appl Phys Lett*., 2003, **82**, 1613–1615.

218. H. Ohno, A window on the future of spintronics, *Nat Mater*., 2010, **9**, 952–954.

219. M. Z. H. Khan, Effect of ITO surface properties on SAM modification: A review toward biosensor application, *Cogent Engineering*., 2016, **3**, 1170097.

220. S. Lee, S. U. S/ Choi, S. Li and J. A. Eastman, Measuring thermal conductivity of fluids containing oxide nanoparticles, *J Heat Transfer*., 1999, **121**, 280-289.

221. Y. Xuan and Q. Li, Heat transfer enhancement of nanofluids, *Int. J. Heat Fluid Flow*., 2000, **21**, 58–64.

222. X. Wang, X. Xu and S. U. S. Choi, Thermal conductivity of nanoparticle - fluid mixture. *Journal of Thermophysics and Heat Transfer*., 1999, **13**, 474–480.

223. J. A. Eastman, S. U. S. Choi, S. Li, W. Yu and L. J. Thompson, Anomalously increased effective thermal conductivities of ethylene glycol-based nanofluids containing copper nanoparticles, *Appl Phys Lett*., 2001, **78**, 718–720.

224. J. A. Eastman, S. U. S. Choi, S. Li, L. J Thompson and S Lee, Enhanced thermal conductivity through the development of nanofluids, *MRS Proc*., 1996, **457**, 3-11.

225. S. U. S. Choi and J. A. Eastman, Enhancing thermal conductivity of fluids with nanoparticles, *ASME FED*, 1995, **231**, 99-103.

226. S. P. Jang and S. U. S. Choi, Cooling performance of a microchannel heat sink with nanofluids, *Appl Therm Eng*., 2006, **26**, 2457–2463.

227. D. Wen, G. Lin, S. Vafaei and K. Zhang, Review of nanofluids for heat transfer applications, *Particuology*., 2009, **7**, 141–150.

228. S. M. S. Murshed, K. C. Leong and C. Yang, Thermophysical and electrokinetic properties of nanofluids – A critical review, *Appl Therm Eng*., 2008, **28**, 2109–2125.

229. W. Yu and H. Xie, A Review on nanofluids: preparation, stability mechanisms, and applications, *J Nanomater*., 2012, **2012**, 1–17.

230. Y. Li, J. Zhou, S. Tung, E. Schneider and S. Xi, A review on development of nanofluid preparation and characterization, *Powder Technol*., 2009, **196**, 89–101.

231. F. H. Lin, C. Liu and P. Zhang, On a micro-macro model for polymeric fluids near equilibrium, *Commun Pure Appl Math*., 2007, **60**, 838–866.

232. R. Sturman, J. M. Ottino and S. Wiggins, The mathematical foundations of mixing: the linked twist map as a paradigm in applications micro to macro, fluids to solids, Cambridge University Press, 2006.

233. A. C. Eringen, Simple microfluids, *Int J Eng Sci*., 1964, **2**, 205–217.

234. B. J. Kirby and E. F. Hasselbrink, Zeta potential of microfluidic substrates: 1. Theory, experimental techniques, and effects on separations, *Electrophoresis*., 2004, **25**, 187–202.

235. I. W. Hamley, Introduction to soft matter– revised edition, Chichester, UK: John Wiley & Sons, 2007.

236. D. F. Evans and H. Wennerström, The Colloidal Domain: Where Physics, Chemistry, Biology, and Technology Meet, Wiley-VCH, 1994.

237. P. Simon and Y. Gogotsi, Materials for electrochemical capacitors, *Nat Mater*., 2008, **7**, 845–854.

238. R. Burt, G. Birkett and X. S. Zhao, A review of molecular modelling of electric double layer capacitors, *Phys Chem Chem Phys*., 2014, **16**, 6519–6538.

239. P. A. Kralchevsky and K. Nagayama, Capillary interactions between particles bound to interfaces, liquid films and biomembranes, *Adv Colloid Interface Sci*., 2000, **85**, 145–192.

240. M. B. McBride, A critique of diffuse double layer models applied to colloid and surface chemistry, *Clays Clay Miner*., 1997, **45**, 598–608.

241. S. S. Dukhin, Non-equilibrium electric surface phenomena, *Adv Colloid Interface Sci*., 1993, **44**, 1–134.

242. B. Derjaguin and L. Landau, Theory of the stability of strongly charged lyophobic sols and of the adhesion of strongly charged particles in solutions of electrolytes, *Prog Surf Sci*., 1993, **43**, 30–59.

243. H. Ohshima, Theory of Colloid and Interfacial Electric Phenomena, Volume 12, 1st Edition, Academic Press, 2006.

244. J. Lyklema, Fundamentals of Interface and Colloid Science, Elsevier, 1995, **2**, 1-59.

245. H. Ohshima, Biophysical chemistry of biointerfaces, Wiley, 2010.

246. E. J. W. Verwey, Theory of the stability of lyophobic colloids, *J Phys Colloid Chem*., 1947, **51**, 631–636.

247. B. V. Derjaguin, Theory of stability of colloids and thin films, Springer, 1989.

248. J. N. Israelachvili, Intermolecular and surface forces, 3rd Edition, Elsevier, 2011.

249. D. L. Chapman, A contribution to the theory of electrocapillarity. The London, Edinburgh, and Dublin Philosophical Magazine and Journal of Science, 1913.

250. M. Gouy, Sur la constitution de la charge électrique à la surface d'un electrolyte, *J Phys Theor Appl*., 1910, **9**, 457–468.

251. O. Stern, Zur Theorie Der Elektroltischen Doppelschicht, Zeitschrift für Elektrochemie und angewandte physikalische Chemie, 2014.

252. D. W. Fuerstenau, Zeta potentials in the flotation of oxide and silicate minerals, *Adv Colloid Interface Sci*., 2005, **114-115**, 9–26.

253. R. J. Hunter, Zeta potential in colloid science: principles and applications, Academic Press, 2013.

254. T. F. Tadros, Industrial applications of dispersions, *Adv Colloid Interface Sci*., 1993, **46**, 1–47.

255. T. F. Tadros, Correlation of viscoelastic properties of stable and flocculated suspensions with their interparticle interactions, *Adv Colloid Interface Sci*., 1996, **68**, 97–200.

256. G. E. Brown, V. E. Henrich, W. H. Casey, D. L. Clark, C. Eggleston and A. Felmy, Metal oxide surfaces and their interactions with aqueous solutions and microbial organisms, *Chem Rev*., 1999, **99**, 77–174.

257. A. Kuiper, Infrared and Raman spectra of benzaldehyde adsorbed on alumina, *J Catal*., 1973, **29**, 40–48.

258. G. Gatta, B. Fubini, G. Ghiotti and C. Morterra, The chemisorption of carbon monoxide on various transition aluminas, *J Catal*., 1976, **43**, 90–98.

259. A. Kuiper, J. Vanbokhoven and J. Medema, The role of heterogeneity in the kinetics of a surface reaction, Infrared characterization of the adsorption structures of organophosphonates and their decomposition, *J Catal*., 1976, **43**, 154–167.

260. R. Finsy, Particle sizing by quasi-elastic light scattering, *Adv Colloid Interface Sci*., 1994, **52**, 79–143.

261. N. G. Khlebtsov, A. G. Melnikov and V. A. Bogatyrev, Relaxation optic phenomena in polydisperse suspensions and determination of particle sizes using transmitted light parameters, *Colloids and Surfaces A: Physicochemical and Engineering Aspects*., 1999, **148**, 17–28.

262. P. Salgi and R. Rajagopalan, Polydispersity in colloids: implications to static structure and scattering, *Adv Colloid Interface Sci*., 1993, **43**, 169–288.

263. G. V. Franks and F. F. Lange, Mechanical behavior of saturated, consolidated, alumina powder compacts: effect of particle size and morphology on the plastic-to-brittle transition, *Colloids and Surfaces A: Physicochemical and Engineering Aspects*., 1999, **146**, 5–17.

264. V. I. Ovod, D. W. Mackowski and R. Finsy, Modeling of the effect of multiple scattering in photon correlation spectroscopy: plane-wave approach, *Langmuir*., 1998, **14**, 2610–2618.

265. M. A. Digman and E. Gratton, Lessons in fluctuation correlation spectroscopy, *Annu Rev Phys Chem*., 2011, **62**, 645–668.

266. R. Dzakpasu and D. Axelrod, Dynamic light scattering microscopy. A novel optical technique to image submicroscopic motions. I: theory, *Biophys J*., 2004, **87**, 1279–1287.

267. D. J. Ross and R. Sigel, Mie scattering by soft core-shell particles and its applications to ellipsometric light scattering, *Phys Rev E Stat Nonlin Soft Matter Phys*., 2012, **85**, 056710.

268. X. Fan, W. Zheng and D. J. Singh, Light scattering and surface plasmons on small spherical particles, *Light Sci Appl*., 2014, **3**, e179.

269. S. H. Hong and J. Winter, Size dependence of optical properties and internal structure of plasma grown carbonaceous nanoparticles studied by in situ Rayleigh-Mie scattering ellipsometry, *J Appl Phys*., 2006, **100**, 064303.

270. S. Bhattacharjee, DLS and zeta potential - What they are and what they are not?, *J Control Release*., 2016, **235**, 337–351.

271. R. Baghi, K. Zhang, S. Wang and L. J. Hope-Weeks, Conductivity tuning of the ITO sol-gel materials by adjusting the tin oxide concentration, morphology and the crystalline size, *Micropor Mesopor Mat*., 2017, **244**, 258–263.

272. X. Sun, Y. Shi, H. Ji, X. Li, S. Cai and C. Zheng, Nanocasting synthesis of ordered mesoporous indium tin oxide (ITO) materials with controllable particle size and high thermal stability, *J Alloys Compd*., 2012, **545**, 5–11.

273. X. Zhang, W. Wu, T. Tian, Y. Man and J. Wang, Deposition of transparent conductive mesoporous indium tin oxide thin films by a dip coating process, *Mater Res Bull*., 2008, **43**, 1016–1022.

274. S. Yoon, E. Kang, J. K. Kim, C. W. Lee and J. Lee, Development of high-performance supercapacitor electrodes using novel ordered mesoporous tungsten oxide materials with high electrical conductivity, *Chem Comm*., 2011, **47**, 1021–1023.

275. J. C. Maxwell, A treatise on electricity and magnetism, Dover Publications, 1831-1879.

276. L. P. Shen, H. Wang, M. Dong, Z. C. Ma and H. B. Wang, Solvothermal synthesis and electrical conductivity model for the zinc oxide-insulated oil nanofluid, *Physics Letters A*., 2012, **376**, 1053–1057.

277. K. G. K. Sarojini, S. V. Manoj, P. K. Singh, T. Pradeep and S. K. Das, Electrical conductivity of ceramic and metallic nanofluids, *Colloids and Surfaces A: Physicochemical and Engineering Aspects*., 2013, **417**, 39–46.

278. S. Ganguly, S. Sikdar and S. Basu, Experimental investigation of the effective electrical conductivity of aluminum oxide nanofluids, *Powder Technol*., 2009, **196**, 326–330.

279. S. B. White, A. J. M. Shih and K. P. Pipe, Investigation of the electrical conductivity of propylene glycol-based ZnO nanofluids, *Nanoscale Res Lett*., 2011, **6**, 346.

280. M. Dong, L. P. Shen, H. Wang, H. B. Wang and J. Miao, Investigation on the electrical conductivity of transformer oil-Based AlN nanofluid, *J Nanomater*., 2013, **2013**, 1–7.

281. A. A. Minea and R. S. Luciu, Investigations on electrical conductivity of stabilized water based Al_2O_3 nanofluids, *Microfluid Nanofluidics*., 2012, **13**, 977–985.

282. S. Bagheli, H. K. Fadafan, R. L. Orimi and M. Ghaemi, Synthesis and experimental investigation of the electrical conductivity of water based magnetite nanofluids, *Powder Technol*., 2015, **274**, 426–430.

283. R. W. O'brien, The electrical conductivity of a dilute suspension of charged particles, *J Colloid Interface Sci*., 1981, **81**, 234–248.

284. J. C. R. Turner, Two-phase conductivity, *Chem. Eng. Sci*. 1976, **31**, 487-492.

285. R. E. Meredith and C. W. Tobias, Conductivities in emulsions, *J. Electrochem. Soc*. 1961, **108**, 286-290.

286. I. Zakaria, W. H. Azmi, W. A. N. W. Mohamed, R. Mamat and G. Najafi, Experimental investigation of thermal conductivity and electrical conductivity of Al_2O_3 nanofluid in water - ethylene glycol mixture for proton exchange membrane fuel cell application, I*nt. Commun. Heat Mass* 2015, **61**, 61-68.

287. A. A. Minea, An Experimental Method to Decrease Heating Time in a Commercial Furnace, *Experimental Heat Transfer*., 2010, **23**, 175-184.

288. B. Glover, K. W. Whites, H. Hong, A Mukherjee and WE Billups, Effective electrical conductivity of functional single-wall carbon nanotubes in aqueous fluids, *Synth Met*., 2008, **158**, 506–508.

289. J. Rao, A. Yu, C. Shao and X. Zhou, Construction of hollow and mesoporous ZnO microsphere: a facile synthesis and sensing property, *ACS Appl Mater Interfaces*., 2012, **4**, 5346–5352.

290. D. S. Kim, S. J. H and S. Y. Kwak, Synthesis and photocatalytic activity of mesoporous TiO2 with the surface area, crystallite size, and pore size, *J. Colloid Interface Sci*., 2007, **316**, 85-91.

291. X. Liu, R. Wang, T. Zhang, Y. He, J. Tu and X. Li, Synthesis and characterization of mesoporous indium oxide for humidity-sensing applications, *Sensors and Actuators B: Chemical*., 2010, **150**, 442–448.

292. E. P. Barrett, L. G. Joyner and P. P. Halenda, The determination of pore volume and area distributions in porous substances. I. computations from nitrogen isotherms, *J Am Chem Soc*., 1951, **73**, 373–380.

293. J. Kayalvizhi and A. Pandurangan, Hydrodeoxygenation of vanillin using palladium on mesoporous KIT-6 in vapor phase reactor, *Molecular Catalysis*., 2017, **436**, 67–77.

294. H. Yang, Q. Shi, B. Tian, Q. Lu, F. Gao and S. Xie, One-step nanocasting synthesis of highly ordered single crystalline indium oxide nanowire arrays from mesostructured frameworks, *J Am Chem Soc*., 2003, **125**, 4724–4725.

295. K. Moller and T. Bein, Inclusion chemistry in periodic mesoporous hosts, *Chem Mater*., 1998, **10**, 2950–2963.

296. T. W. Kim, F. Kleitz, B. Paul and R. Ryoo, MCM-48-like large mesoporous silicas with tailored pore structure: facile synthesis domain in a ternary triblock copolymer-butanol-water system, *J Am Chem Soc*., 2005, **127**, 7601–7610.

297. S. Storck, H. Bretinger and W. F. Maier, Characterization of micro- and mesoporous solids by physisorption methods and pore-size analysis, *Applied Catalysis A: General*., 1998, **174**, 137–146.

298. S. Brunauer and P. H. Emmett, Chemisorptions of gases on iron synthetic ammonia catalysts, *J Am Chem Soc*., 1940, **62**, 1732–1746.

299. R. L. Weiher, Electrical Properties of Single Crystals of Indium Oxide, *J. Appl. Phys*., 1962, **33**, 2834.

300. X. Sun, Y. Shi, H. Ji, X. Li, S. Cai and C. Zheng, Nanocasting synthesis of ordered mesoporous indium tin oxide (ITO) materials with controllable particle size and high thermal stability, *J. Alloy Compd*., 2012, **545**, 5-11.

301. S. Y. Jung, T. J. Ha, C. S. Park, W. S. Seo, Y. S. Lim, S. Shin, H. H. Cho and H. H. Park, Improvement in the conductivity ratio of ordered mesoporous Ag-TiO_2 thin films for thermoelectric materials, *Thin Solid Films*, 2013, **529**, 94-97.

302. S. Y. Jung, T. J. Ha, W. S. Seo, Y. S. Lim, S. Shin, H. H. Cho and H. H. Park, Thermoelectric properties of Nb-doped ordered mesoporous TiO_2, *J. Electron. Mater.*, 2011, **40**, 652-656.

303. R. Wang and A. W. Sleight, High conductivity in gallium-doped zinc oxide powders, *Chem. Mater*., 1996, **8**, 433-439.

304. A. Moisala, Q. Li, I. A. Kinloch, A. H. Windle, Thermal and electrical conductivity of single- and multi-walled carbon nanotube-epoxy composites, *Compos. Sci. Technol.*, 2006, **66**, 1285.

305. L. Gao, X. Zhou and Y. Ding, Effective thermal and electrical conductivity of carbon nanotube composites, *Chem. Phys. Lett*., 2007, **434**, 297-300.

306. M. Kole and T. K. Dey, Investigation of thermal conductivity, viscosity, and electrical conductivity of graphene based nanofluids, *J. Appl. Phys.*, 2013, **113**, 084307.

307. H. R. Astorga and D. Mendoza, Electrical conductivity of multiwall carbon nanotubes thin films, *Opt. Mater*., 2005, **27**, 1228-1230.

308. T. T. Baby and S. Ramaprabhu, Investigation of thermal and electrical conductivity of graphene based nanofluids, *J. Appl. Phys*., 2010, **108**, 124308.

309. K. Suttiponparnit, J. Jiang, M. Sahu, S. Suvachittanont, T. Charinpanitkul and P. Biswas, Role of surface area, primary particle size, and crystal phase on titanium dioxide nanoparticle dispersion properties, *Nanoscale Res. Lett*., 2011, **6**, 27.

310. W. M. Sigmund, N. S. Bell and L. Bergström, Novel powder-processing methods for advanced ceramics, *J. Am. Ceram. Soc*., 2000, **83**, 1557-1574.

311. R. J. Pugh and L. Bergström, Surface and Colloid Chemistry in Advanced Ceramics Processing, CRC Press, New York, 1993.

312. Drew Myers, Surfaces, interfaces, and colloids: principles and applications, Wiley-VCH, Weinheim, 1999.

313. K. Bourikas, T. Hiemstra and W. H. Van Riemsdijk, Ion pair formation and primary charging behavior of titanium oxide (anatase and rutile), *Langmuir*, 2001, **17**, 749-756.

314. N. H. Tkachenko, Z. M. Yaremko, C. Bellmann and M. M. Soltys, The influence of ionic and nonionic surfactants on aggregative stability and electrical surface properties of aqueous suspensions of titanium dioxide, *J Colloid Interface Sci*., 2006, **299**, 686-695.

315. W. M. Sigmund, N. S. Bell and L. Bergström, Novel powder-processing methods for advanced ceramics, *J. Am. Ceram. Soc*., 2000, **83**, 1557-1574.

316. F. Bordi, C. Cametti, P. Codastefano and P. Tartaglia, Electrical conductivity of colloidal systems during irreversible aggregation, *Physica A*, 1990, **164**, 663-672.

317. R. A. Reichle, K. G. McCurdy and L. G. Hepler, Zinc Hydroxide: Solubility Product and Hydroxy-complex Stability Constants from 12.5–75 °C, *Can J Chem.*, 1975, **53**, 3841-3845.

318. W. J. Tseng and F. Tzeng, Effect of ammonium polyacrylate on dispersion and rheology of aqueous ITO nanoparticle colloids, *Colloids Surf. A* 2006, **276**, 34-39.

319. S. Chakraborty and S. Padhy, Anomalous electrical conductivity of nano-scale colloidal suspensions, *ACS Nano*, 2008, **2**, 2029-2036.

320. D. Zhu, X. Li, N. Wang, X Wang, J. Gao and H. Li, Dispersion behavior and thermal conductivity characteristics of Al_2O_3–H_2O nanofluids, *Curr. Appl. Phys.*, 2009, **9**, 131-139.

321. H. Kim and C. M. Gilmore, Electrical, optical, and structural properties of indium–tin–oxide thin films for organic light-emitting devices, *J Appl Phys.*, 1999, **86**, 6451.

322. L. B. Modesto-Lopez and P. Biswas, Role of the effective electrical conductivity of nanosuspensions in the generation of TiO_2 agglomerates with electrospray, *J Aerosol Sci.*, 2010, **41**, 790-804.

323. S. N. Shoghl, J. Jamali and M. K. Moraveji, Electrical conductivity, viscosity, and density of different nanofluids: An experimental study, *Exp. Therm. Fluid. Sci.*, 2016, **4**, 339-346.

324. H. Kim, C. M. Gilmore, A. Piqué, J. S. Horwitz, H. Mattoussi and H. Murata, Electrical, optical, and structural properties of indium–tin–oxide thin films for organic light-emitting devices, *J Appl Phys.*, 1999, **86**, 6451.

325. D. Henderson, L. Blum and M. Lozada-Cassou, The statistical mechanics of the electric double layer, *J Electroanal Chem Interfacial Electrochem.*, 1983, **150**, 291–303.

326. C. Schreiner, S. Zugmann, R. Hartl and H. J. Gores, Fractional Walden rule for ionic liquids: examples from recent measurements and a critique of the so-called ideal KCl line for the Walden plot, *J. Chem. Eng. Data.*, 2010, **55**, 1784–1788.

327. F. F. Chen, Introduction to Plasma Physics, Springer, 1974.

328. R. A. Griffin and J. J. Jurinak, Estimation of activity coefficients from the electrical conductivity of natural aquatic systems and soil extracts, *Soil Science.*, 1973, **116**, 26-30.

329. R. J. Hunter, Foundations of Colloid Science, 2nd Edition, Oxford University Press, 1987.

330. C. I. Bouzigues, P. Tabeling and L. Bocquet, Nanofluidics in the Debye layer at hydrophilic and hydrophobic surfaces, *Phys Rev Lett.*, 2008, **101**, 114503.

331. C. P. Tso, C. M. Zhung, Y. H. Shih, Y. M. Tseng, S. C. Wu and R. A. Doong, Stability of metal oxide nanoparticles in aqueous solutions, *Water Sci. Technol.*, 2010, **61**, 127-133.

332. J. Zhai, X. Tao, Y. Pu, X. F. Zeng and J. F. Chen, Core/shell structured ZnO/SiO_2 nanoparticles: Preparation, characterization and photocatalytic property, *Appl. Surf. Sci.*, 2010, **257**, 393-397.

333. F. Yuan, H. Peng, Y. Yin, Y. Chunlei and H. Ryu, Preparation of zinc oxide nanoparticles coated with homogeneous Al_2O_3 layer, *Mater. Sci. Eng. B*, 2005, **122**, 55-60.

334. M. H. Liao, C. H. Hsu and D. H. Chen, Preparation and properties of amorphous titania-coated zinc oxide nanoparticles, *J. Solid State Chem.*, 2006, **179**, 2020-2026.